

Scuola di Scienze  
Dipartimento di Fisica e Astronomia  
Corso di Laurea Magistrale in Fisica del Sistema Terra

**Shelf break frontal dynamics and its  
ecosystem implications at the  
Mid-Atlantic Bight**

**Relatrice:**

**Prof.ssa Nadia Pinardi**

**Presentata da:**

**Serena Negroni**

**Correlatori:**

**Dr. Dennis McGillicuddy**

**Dr. Glen Gawarkiewicz**

**Prof. Paolo Oddo**

Sessione IV  
Anno Accademico 2022/2023



You remember the old prayer for those in peril on the sea? Perhaps there should be a special prayer for those trying to explain the sea.

- Henry Stommel

*A mio nonno Archimede, che mi è sempre stato accanto durante questo percorso.*



---

## Abstract

Shelf break fronts represent areas of high productivity found at the edges of continental shelves. The Mid-Atlantic Bight frontal system along the U.S. northeast shelf is one of those. In this region, the enhanced primary production is maintained by upwelling mechanisms, also involving Gulf Stream submesoscale instabilities that interact with the shelf. Nevertheless, it is noteworthy that the concentrations of chlorophyll- $\alpha$  (Chl- $\alpha$ ) in the shelf break region do not consistently exhibit enhancement throughout the year even if local increases of phytoplankton biomass have been observed in some circumstances, hence the whole process is not completely clear. In this thesis, we aim to investigate the frontal dynamics in order to clarify some of the mechanisms controlling primary production.

A comprehensive inter-annual analysis (2003-2020), conducted using satellite images of surface Chl- $\alpha$  concentration, revealed periodic variability aligned with Spring and Autumn blooms, exhibiting coherence with surface wind variability. However, short-lived Chl- $\alpha$  enhancements do not strongly correlate with surface winds, suggesting that the observed variability is driven by a combination of upwelling mechanisms not directly connected to winds.

Furthermore, the connection between upwelling mechanisms, involving the detachment of the bottom boundary layer (BBL), and the observed increase in Chl- $\alpha$  concentration at the shelf break front is investigated. The detachment of the BBL is examined using *in situ* data and an extensive characterization of this process is given by applying two methodologies: accumulated properties change algorithm and along isopycnal change in properties, which revealed a significant BBL variability influenced by Gulf Stream features and seasonal stratification conditions. Moreover, we investigated the correlation between the detaching BBL, nutrient distribution, and Chl- $\alpha$  abundance along isopycnals. Results indicate that the relationships between nitrate decline and phytoplankton biomass increase are not as straightforward as expected, which might be related to the limited statistical support, attributed to sample size, intrinsic data variability, and the assumption of bidimensionality.

---

---

## Sommario

I fronti oceanici che si trovano ai confini delle piattaforme continentali (shelf-break), sono aree ad elevata produttività. Il sistema del fronte della Baia Medio-Atlantica (MAB), situato lungo il confine nord-orientale della piattaforma continentale degli Stati Uniti, è uno di questi. In tale regione, elevate concentrazioni di fitoplankton sono mantenute da meccanismi di risalita, tra cui anche le instabilità di submesoscala della Corrente del Golfo che interagiscono con la piattaforma. Tuttavia, è noto che le concentrazioni di clorofilla- $\alpha$  (Chl- $\alpha$ ) nella regione del shelf-break non presentano degli aumenti coerenti durante tutto l'anno, anche se delle intensificazioni locali sono state osservate in determinate circostanze; comunque l'intero processo non è del tutto ben spiegato. Perciò, lo scopo di tale tesi è quello di investigare in modo più approfondito la dinamica frontale, per chiarire alcuni dei meccanismi che controllano la produttività primaria.

Utilizzando immagini satellitari delle concentrazioni superficiali di Chl- $\alpha$ , si è condotta un'analisi della variabilità inter-annuale (periodo: 2003 - 2020), la quale ha rivelato delle oscillazioni periodiche corrispondenti con le fioriture primaverili e autunnali. Esse sono risultate coerenti con la variabilità del vento in superficie. Ciononostante, gli aumenti di breve durata della Chl- $\alpha$  non sono correlati in modo robusto con la variabilità di larga scala dei venti di superficie, suggerendo che la variabilità osservata è guidata da una combinazione di meccanismi di risalita non direttamente connessi ai venti.

Inoltre, si è investigata la connessione tra i meccanismi di risalita che coinvolgono il distacco dello strato limite in prossimità del fondale (BBL), e gli aumenti osservati nelle concentrazioni di Chl- $\alpha$  nei pressi del fronte al shelf-break. Il distacco del BBL è stato analizzato utilizzando dati *in situ*. Si è fornita un'ampia caratterizzazione di tale processo applicando due metodi: un algoritmo di variazione accumulata delle proprietà e differenze delle proprietà calcolate lungo le isopiche. Essi hanno rivelato una significativa variabilità del BBL, influenzata dalle strutture di submesoscala della Corrente del Golfo e dalle condizioni di stratificazione stagionale. Inoltre, si è indagata la correlazione tra il sollevamento del BBL, la distribuzione dei nutrienti e l'abbondanza di fitoplancton lungo le isopiche. I risultati indicano che le relazioni tra la diminuzione dei nitrati e l'aumento della biomassa del fitoplancton non sono così dirette come ci si potrebbe aspettare. Ciò potrebbe essere dovuto al limitato supporto statistico, attribuibile alla dimensione del campione, alla variabilità intrinseca dei dati e all'assunzione di bidimensionalità.

---

# Contents

<b>1</b>	<b>Introduction</b>	<b>1</b>
1.1	Shelf break fronts dynamics . . . . .	3
1.1.1	Bottom boundary layer detachment . . . . .	6
1.2	Biological productivity at shelf break fronts . . . . .	7
1.2.1	Phytoplankton abundance . . . . .	7
1.3	Thesis objectives . . . . .	14
<b>2</b>	<b>Data and methods</b>	<b>17</b>
2.1	Field <i>in situ</i> data . . . . .	17
2.1.1	Accumulated properties change algorithm . . . . .	19
2.1.2	Along isopycnals change in properties . . . . .	21
2.2	Satellite Chlorophyll- $\alpha$ . . . . .	23
2.2.1	Space-time analysis method . . . . .	25
2.3	Reanalysis datasets . . . . .	25
2.4	Bathymetry . . . . .	27
<b>3</b>	<b>Characterization of inter-annual chlorophyll-<math>\alpha</math> variability</b>	<b>29</b>
3.1	MODIS surface Chlorophyll- $\alpha$ concentration . . . . .	29
3.1.1	Time series of spatially averaged Chl- $\alpha$ . . . . .	31
3.1.2	Variability of surface chlorophyll- $\alpha$ concentration . . . . .	33
3.1.3	Space-time analysis method for Chl- $\alpha$ concentration . . . . .	36
3.2	Environmental conditions . . . . .	39
3.2.1	Surface Winds . . . . .	39
3.2.2	Sea surface temperature, salinity and currents . . . . .	40
<b>4</b>	<b>Physical drivers for chlorophyll-<math>\alpha</math> variability</b>	<b>43</b>
4.1	Relation between wind transport and enhanced surface Chl- $\alpha$ . . . . .	43
4.2	Nutrient transport induced by bottom boundary layer detachment . . . . .	46
4.2.1	CTD and Niskin bottles sections . . . . .	47

## CONTENTS

---

4.2.2	Accumulated properties change . . . . .	60
4.2.3	Along isopycnal change in properties . . . . .	65
<b>5</b>	<b>Conclusions and outlooks</b>	<b>73</b>
<b>A</b>	<b>Accumulated properties change figures</b>	<b>77</b>
	<b>Bibliography</b>	<b>87</b>

# Chapter 1

## Introduction

The Middle Atlantic Bight (MAB) continental shelf is a part of the U.S. northeast shelf which is one of the most productive marine ecosystems. The ecosystem is nourished by high concentrations of phytoplankton, that undergo substantial variations over broad spatial and temporal scales [Zhang et al., 2013]. Current paradigms suggest that this productivity is driven by several upwelling mechanisms located within the shelf break front [He et al. [2011], Oliver et al. [2022], Zhang et al. [2023]]. This upwelling supplies nutrients that stimulate primary production by phytoplankton, which in turn leads to enhanced production at higher trophic levels. Although local enhancement of phytoplankton biomass has been observed in some synoptic measurements within the region, such a feature is absent from time-averaged measurements, both remotely sensed and *in situ*. The shelf break front region is typically located between 100 m and 200 m isobaths and it is characterized by large horizontal and vertical gradients in water properties and persistent upwelling associated with the front. However, this is a feature susceptible to nonlinear instabilities and strong interactions with the Gulf Stream warm-core rings that impinge on the continental slope. In addition, in the region, there is a persistent shelf break jet (Figure 1.1, [Forsyth et al., 2020]) that contributes to the large fluxes of heat, freshwater, and nutrients that control the water mass characteristics and the ecosystem within the area of the shelf break. The shelf break frontal processes are inherently non-linear and exhibit variation over a broad range of spatial and temporal scales. In particular, there are strong vertical motions associated with the shelf break front, which may significantly influence the circulation and the ecosystem dynamics of the region. Specifically, the upward motion could deliver nutrients into the euphotic zone and stimulate local primary productivity. Although the processes regulating the shelf break upwelling are complex, some simple models have been used to understand different dynamic aspects. For example, Zhang et al. [2011] developed a 2D model to investigate the

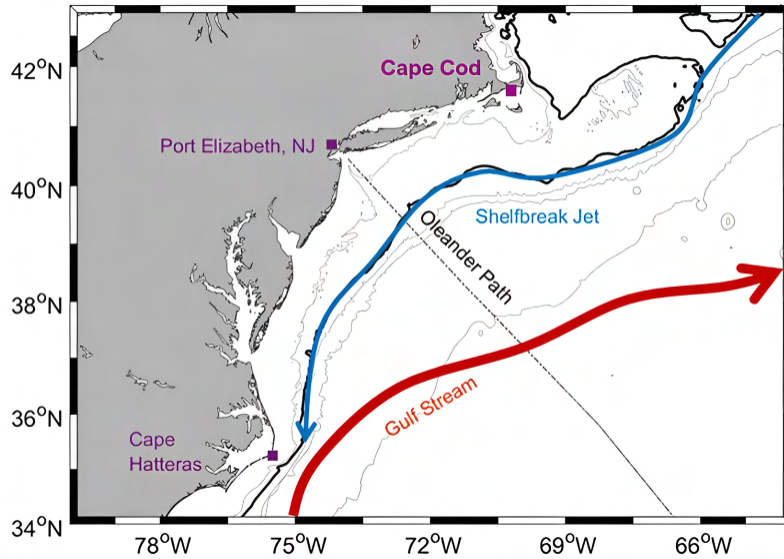


**Figure 1.1:** Map of the MAB including the location of the shelf break Jet (blue) and Gulf Stream (red). Gray contours of bathymetry are shown indicating the 40-, 1000-, 2000- and 4000-m isobath, with the 100-m isobath shown in black. Modified from Forsyth et al. [2020].

mean cross-shelf and vertical circulation at the shelf break and its seasonal variation. The results showed a secondary circulation at the front (Fig. 1.2, upper left), associated with the geostrophic adjustment of the interior. Specifically, the mean flow within the surface and bottom boundary layer is predominantly off-shore, due to the influence of mean wind stress and bottom Ekman layer dynamics respectively. These off-shore flows are balanced by interior on-shore flow along the shelf, causing a mean upward motion with speeds of tens of cm/day to a few m/day depending on the season. Another upwelling mechanism acting within the front is the convergence in the bottom boundary layer (Fig. 1.2, upper right; [Pickart, 2000], [Gawarkiewicz et al., 2004]). Observations at the shelf break [Barth et al. [1998], Houghton and Visbeck [1998]] have shown convergence of the cross-shelf bottom flows near the foot of the shelf break front, leading to a detachment of the bottom boundary layer and then upwelling into the interior. Eventually, instability-driven meandering of the shelf break front can drive upwelling dynamics (Fig. 1.2, bottom; [Zhang and Gawarkiewicz, 2015]). As demonstrated by studies in the open ocean ([Levy Marina, 2001]), also frontal instability can induce strong vertical motion (several to tens of m/day) through mesoscale and submesoscale vorticity dynamics. All these upwelling mechanisms could deliver nutrients to the euphotic zone, thereby increasing productivity. However, as the associated spatial and temporal scales are dramatically different, the overall strength of these different types of upwelling and the relative

importance of the vertical nutrient fluxes associated with each are not well constrained. Nevertheless, despite the upwelling processes there does not appear to be a significant enhancement in the seasonal mean cross-shelf distribution of chlorophyll in either satellite-based or *in situ* data sets [Zhang et al., 2013]. In this contest, the *Shelf Break Productivity Interdisciplinary Research Operation at the Pioneer Array* (SPIROPA) aims to answer why there would not be an enhancement of mean chlorophyll associated with the mean upwelling.

This work follows previous investigations done to test the hypothesis of upwelling mechanisms at the shelf break front and if they can lead to a biological response, enhancing surface and/or subsurface chlorophyll concentration. In the following sections, some theoretical bases related to the physics of the shelf-break front are given (Section 1.1), as well as some details associated with the biogeochemistry of oceanic nutrients cycles and primary production (Section 1.2).

## 1.1 Shelf break fronts dynamics

Various types of fronts are commonly found throughout the world ocean. Among these, the shelf break fronts are those occurring at the edge of the continental shelves. In general, they separate relatively cold and fresh shelf waters from relatively warm and saline slope water. Because of this characteristic and their topographic constrain, they are remarkably robust. The Middle Atlantic shelf break front is one of those. The mechanism of frontogenesis was modeled and understood in the early '90 by Gawarkiewicz and Chapman [1992]. In this type of front, the horizontal stratification is created from a freshwater inflow (for the MAB coming from the Labrador Sea) which tends to form a plume that spans the water column from surface to bottom

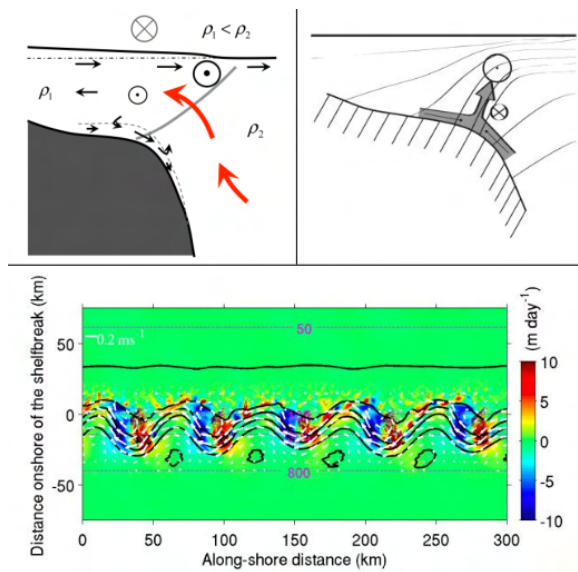


**Figure 1.2:** Three upwelling mechanisms at the shelf break. Upper left: mean upward motion (red arrows) driven by divergence in the on-shore interior flow [Zhang et al., 2011]. Upper right: along-isopycnal upwelling associated with convergence in the bottom boundary layer [Linder et al., 2004]. Bottom: vertical motion associated with frontal meandering in an idealized simulation [Zhang and Gawarkiewicz, 2015]. Colors, white arrows, and black lines indicate vertical velocity, horizontal velocity, and isopycnal contours (interval of  $0.1 \text{ kg m/kg}^3$ ) at 40 m; magenta lines are isobaths. By courtesy of McGillicuddy Jr. et al. [2016].

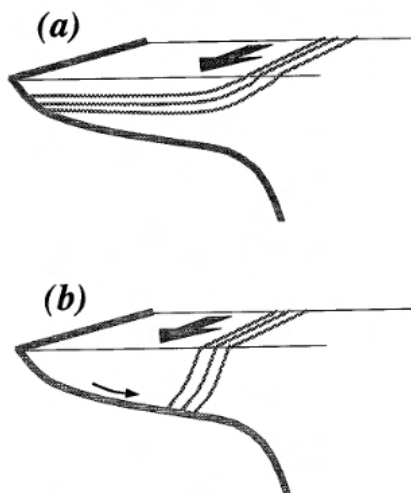


**Figure 1.3:** Sketches depicting (a) a shallow surface-trapped freshwater plume and (b) a surface-to-bottom freshwater plume. The large arrows indicate the directions of the surface currents. The small arrow represents off-shore transport in the bottom boundary layer. Case (b) is the subject of study here. Taken from [Chapman and Lentz \[1994\]](#).

[[Chapman and Lentz, 1994](#)]. This surface-to-bottom plume is positively influenced by the bottom topography because much of the plume is in direct contact with the bottom. In particular, as shown in [Figure 1.3](#), the along-shelf flow generates an off-shore flow of fresh water in the bottom boundary layer, which should push the entire front further off-shore and thereby alter both the density and velocity field. A cross-shelf density gradient along the bottom is created and it is proportional to the bottom slope [[Gawarkiewicz and Chapman, 1992](#)]. The more the slope becomes greater approaching the shelf break, the more the cross-shelf density gradient along the bottom increases. This in turn inhibits the off-shore transport along the bottom and results in a convergence in the bottom boundary layer (BBL) at the shelf break. Since the BBL transports lighter shelf water seaward, the convergence near the shelf break leads to an accumulation of buoyancy there, which then further enhances the cross-shelf density gradient. This positive feedback between the BBL convergence and the cross-shelf gradient can create an adverse cross-shelf pressure gradient strong enough to detach the BBL near the shelf break, as shown in [Figure 1.4 \(a\)](#). In this manner, the shelf break front is created and maintained. Moreover, the cross-shelf circulation that moves the freshwater off-shore, under the saltier water, creates an unstable situation, thereby the front needs to adjust geostrophically [[Chapman and Lentz, 1994](#)]. In other words, the pressure gradients created by the two different water masses must be balanced with the Coriolis effect and, instead of moving water from a region of high pressure (or high sea level) to a region of low pressure (or low sea level), it moves along the lines of equal pressure (isobars). The *geostrophic balance* is a first-order approximation of the *Navier–Stokes equations* in a rotating reference

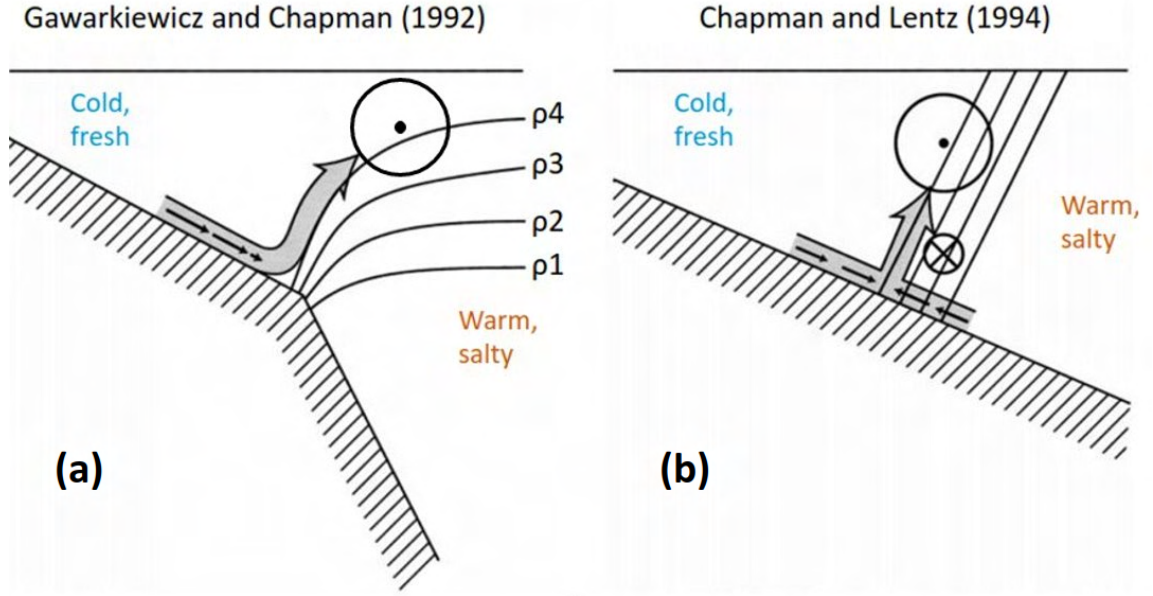


**Figure 1.4:** Schematic of the shelf break front and detached BBL in two model studies. (a) Gawarkiewicz and Chapman (1992) model: convergent flow in the BBL (short arrows) detaches at the shelf break due to the on-shore pressure gradient resulting from the concentration of frontal isopycnals. The large shaded arrow denotes the trajectories of fluid parcels as they advect into the interior. (b) Chapman and Lentz (1994) model: Geostrophic adjustment of the front leads to a flow reversal in the jet at depth (( $\odot$ : equatorward flow,  $\otimes$ : poleward flow), which leads to opposing upslope and downslope flow in the BBL; the associated collision leads to detachment. Modified from Pickart [2000].

frame. In particular, it is assumed that there is no acceleration (steady-state), no viscosity, and that the pressure is hydrostatic. The resulting balance is:

$$\begin{aligned} f v_g &= \frac{1}{\rho} \frac{\partial p}{\partial x} \\ f u_g &= -\frac{1}{\rho} \frac{\partial p}{\partial y} \end{aligned} \quad (1.1)$$

where  $f = 1.45 \times 10^{-4} \text{ s}^{-1}$  is the *Coriolis parameter*,  $\rho$  is the water density,  $p$  is the pressure field and  $u_g$ ,  $v_g$  are the geostrophic velocities in  $x$ ,  $y$  directions respectively. In the present reference system, the  $x$  coordinate represents the along-shelf direction, while  $y$  is the cross-shelf direction. As a consequence, a surface-intensified along-shelf jet with a strong vertical shear is generated, thus reducing the along-shelf velocity to small values at the base of the front. The same happens on the other side of the front with the poleward flow that induces an upslope flow in the BBL that counteracts the downslope flow. The interior density front reaches an equilibrium position at the shelf break (see Figure 1.4 (b)), consequently the convergence of the two flows in the BBL leads to a detachment, and the water parcels are forced to move upwards, following density contours. Eventually, the front reaches a steady state equilibrium

in which it is “trapped” along an isobath by the advection of density in the BBL. For this reason, the shelf break fronts are a persistent feature characterizing the continental shelf breaks, even though they can be significantly altered by off-shore forcing.

### 1.1.1 Bottom boundary layer detachment

As illustrated in the previous section, the BBL plays a fundamental role in the establishment of the shelf break front. In particular, two mechanisms have been depicted (see Figure 1.4) to explain the frontogenesis of the MAB shelf break front, and, as a consequence in both of them, the detachment of the BBL is expected. In the present work we follow the definition of BBL given by [Pickart \[2000\]](#): it is the weakly stratified near-bottom layer, which is separated by a distinct interface of constant temperature, salinity, and density from the above water column. It has been proved that the BBL may be the result of mechanical mixing rather than convective overturning because it has been observed a constant density interface between the interior and the BBL and not a jump in this property. However, its structure can be significantly influenced by the changes of the interior flow above, related to the bottom local topography or the ambient slope water, thereby major variations can be observed close to the location of the shelf break front. In addition, the down-slope flow in the BBL, beneath the equatorward-slowing shelf break jet, separates from the bottom upon encountering the shelf break front. Thus, it is the cross-stream convergence of the jet in the BBL that suggests that an interior convergent flow may upwell and enhance the flow of the detached BBL. This has been verified by [Houghton and Visbeck \[1998\]](#), who performed a dye-release experiment at the bottom of the MAB shelf break front near 70°W, demonstrating that the water parcels detached from the BBL, move toward the surface following the isopycnals. An order of magnitude estimation for the *upwelling velocity* can be obtained by integrating the continuity equation:

$$w = \int_{z_{bottom}}^{z_{surf}} \frac{dv}{dy} dz \quad (1.2)$$

where  $\frac{dv}{dy}$  is the cross-shelf gradient of the cross-shelf velocity and  $dz$  is the vertical spacing. Combining  $w$  estimation with measured  $v$ , [Pickart \[2000\]](#) was able to calculate the pattern of the secondary circulation associated with the detachment of the BBL (see Figure 1.5) and showed that the strongest vertical flow is aligned along the detached BBL.

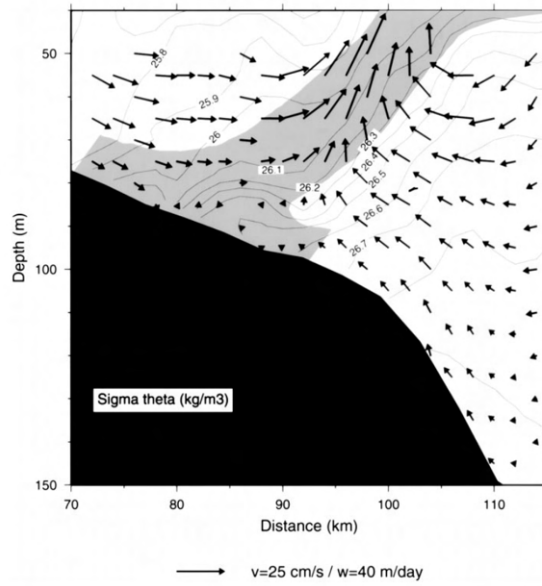


**Figure 1.5:** Inferred secondary circulation (vectors) in relation to the density field and the detached BBL (gray shading). Taken from [Pickart \[2000\]](#).

## 1.2 Biological productivity at shelf break fronts

Shelf break fronts are the most active and important ones from a biological point of view [[K.H. Mann, 2006](#)]. Along the eastern seaboard of North America, at the edge of the continental shelf, maxima in biological variables such as chlorophyll, primary productivity, zooplankton, etc, were observed in association with the shelf break front, leading to enhancements visible from satellite images. A typical enhanced condition is reported in [Figure 1.6](#). These increases are due to the upward mixing of the nutrient-rich deeper water into the euphotic zone over the shelf. In addition, intense wind events and Gulf Stream meanders force similar flows. In the following paragraphs, a focus on ecosystem dynamics is given.

### 1.2.1 Phytoplankton abundance

Oceanic primary production is the creation of new organic compounds in the ocean from atmospheric or dissolved carbon dioxide. The organisms responsible for primary production are called primary producers or autotrophs; they are able to manufacture organic matter by photosynthesis or chemosynthesis. Photosynthetic primary producers use light-derive energy to convert carbon dioxide into organic carbon compounds. On the other hand, chemosynthetic primary producers use oxidation or reduction of inorganic chemical compounds as their source of energy. For the purpose of this study, we will focus on the factors regulating the ecosystem behavior of phytoplanktonic producers. The existence of phytoplankton in ocean water is important because it is responsible for more than 90% of the fixation of inorganic carbon to

## 1 Introduction

---

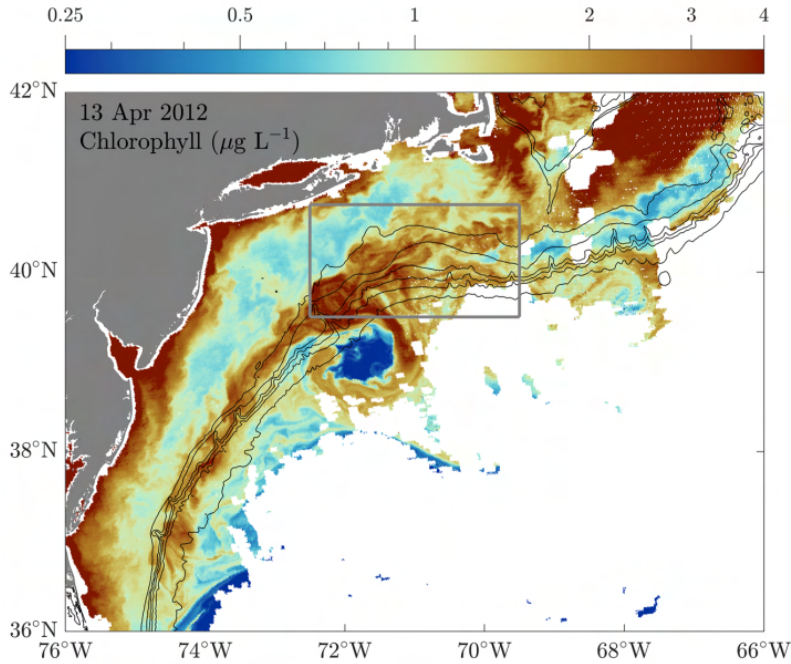
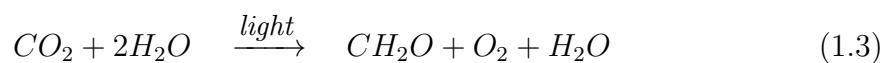


**Figure 1.6:** Example snapshot of enhanced chlorophyll at the shelf break, depth contours at 75, 100, 200, 500, 1000, and 2000 m. The gray box indicates the geographic boundaries of the SPIROPA sampling area. Note the log color axis scale. Taken from [Oliver et al. \[2022\]](#).

organic matter across the oceans' surface; furnishing the organic matter that largely supports marine consumer food web [[Valiela, 2015](#)]. Phytoplankton plays an important role in the sequestration of atmospheric carbon into the oceans, fixing it in the illuminated upper layers of the seas and burring toward deeper layers when it sinks as cell or pelleted into fecal material excreted by planktonic consumers [[Valiela, 2015](#)]. The species of phytoplankton are widely distributed and grow reasonably quickly but local conditions can significantly alter their population. Light, nutrients, and temperature are immediate factors that control the abundance and the activity of primary producers. Also grazing by zooplankton or larger marine organisms and sinking affects the rates of growth and governs densities. To understand how all these aspects combine, it is necessary to understand how phytoplankton forms organic matter.

The main reaction that allows phytoplankton to acquire and metabolize carbon to get energy is *photosynthesis*. Its basic equation can be expressed as:

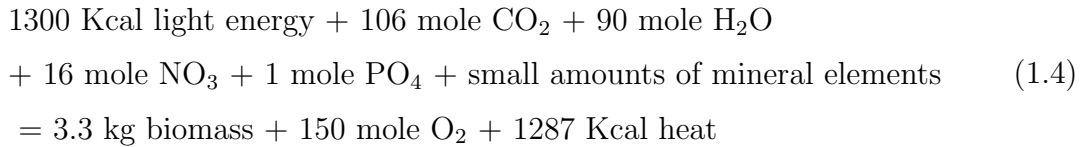


Thus, the reaction can only happen if enough light is available and depends on the capture of the photons by photosynthetic pigments. For the case considered, water is

## 1.2 Biological productivity at shelf break fronts

---

an electron donor, and two molecules of water are split to form one molecule of oxygen, one molecule of water, and one molecule of carbohydrates ( $\text{CH}_2\text{O}$ ). The energy of excited electrons released during the reaction is used to make the hydrogen carrier NADPH and the energy-storage molecule ATP (adenosine triphosphate). However, equation 1.3 is incomplete, because producers require a variety of inorganic nutrients to provide the building blocks for the synthesis of the compounds that form their cells. Thereby the equation becomes [Valiela, 2015]:



These values are based on the average contents of phytoplanktonic cells, but there could be considerable variations in these elemental ratios. For example, phytoplankton may use ammonium rather than nitrate to satisfy its nitrogen requirement [Valiela, 2015]. Consequently, limitations in the light and nutrient availability can vary the ratios between available matter and biomass produced.

### Light availability

Light is one of the controlling factors of primary production. The solar radiation incoming at the Earth's surface reduces its intensity passing through the atmosphere, whose compounds absorb part of the spectrum for solar energy. The amount of light reaching the sea surface is further reduced by clouds, scattering, and reflection. When the sun is low in the sky or during rough seas, over 30 % of the radiation may be lost. Instead, during clear days with mild wind conditions, only a small percentage of this radiation is lost. In addition, daily, seasonal, and weather variations are a constant source of variability for solar irradiance (photons arriving on a surface [ $\text{m}^2/\text{s}$ ]). Moreover, the light is absorbed by water particles itself, suspended particles in the water column, and dissolved organic matter, so only a small fraction of the solar radiation penetrates the water column. Thus, the amount of light penetrating to any depth  $z$ , can be described by *Beer's Law*:

$$I_z = I_0 e^{-k_d z} \quad (1.5)$$

where  $I_z$  is the irradiance at  $z$ , the depth of interest,  $I_0$  is the irradiance at the sea surface, and  $k_d$  is the extinction coefficient, which strongly depends on location and wavelengths. The light in the water column decreases exponentially with depth, thereby it can be distinguished between the *euphotic zone* and the *aphotic zone*. The former is the upper layer that receives sunlight, allowing phytoplankton to per-

## 1 Introduction

---

form photosynthesis and creating the perfect conditions for aquatic life to prosper; in fact, it is the zone where 90 % of the marine creatures live. The *aphotic zone* is characterized by little or no sunlight. Usually, the boundary between the two is represented by the depth at which the amount of light corresponds to the 1% of the surface irradiance. The depth of the *euphotic zone* varies greatly, depending on the amount of suspended particles and dissolved organic matter. For example, mixing of the nutrient-rich waters in spring reduces light penetration because of the resuspended bottom particles, the large amount of dissolved organic matter, and blooms of phytoplankton [Valiela, 2015]. In contrast, during summer, the *euphotic zone* is usually found to have greater depth associated with subsurface chlorophyll maxima. Moreover, the depth of the *euphotic zone* varies according to the daily variation of sunlight. All these variability make photosynthesis not constant over time. In a not well-lit environment, producers may adapt physiologically to ambient light intensity, primarily by varying the number of pigments involved in harvesting photons. Accordingly, photosynthesis in cells is carried out by photosynthetic units composed of a light-collecting antenna and a reaction center made up of chlorophyll- $\alpha$ . Under low light conditions, the size of the antenna increases to improve the photosynthetic efficiency or the ability to collect light, resulting in higher photosynthesis rates per unit chlorophyll [Valiela, 2015]. This mechanism is called *photoadaptation*. As a consequence of that, high measurements of chlorophyll- $\alpha$  may not correspond to high biomass volume.

### Nutrients availability

Nutrient supply may affect the photosynthetic performance. For example, in nutrient-rich conditions, the rates of photosynthesis can increase at any value of irradiance. The main organic elements building up organic matter are hydrogen (H), carbon (C), nitrogen (N), oxygen (O), and phosphorus (P), which are found in an approximately constant stoichiometric ratio in oceanic organisms [Sarmiento, 2006]. In particular, for C, N, and P it has empirically found that  $C:N:P = 106:16:1$ . This is known as *Redfield's ratio*, named after the first scientist who described how the chemistry of the deep ocean and the chemistry of living things, such as phytoplankton in the surface ocean, were related. The *Redfield's ratio* is used to estimate the carbon and nutrient fluxes in the biogeochemical cycles of the oceans [Redfield, 1934].

Phytoplankton needs to take up elements from seawater in order to form organic matter (see equation 1.3), among all, the main nutrient-limiting factor for photosynthesis is nitrogen; probably because nitrogen containing photosynthetic pigments (which are useful as protein reserve and as collectors of photons) increases when N supply increases and vice-versa [Valiela, 2015].

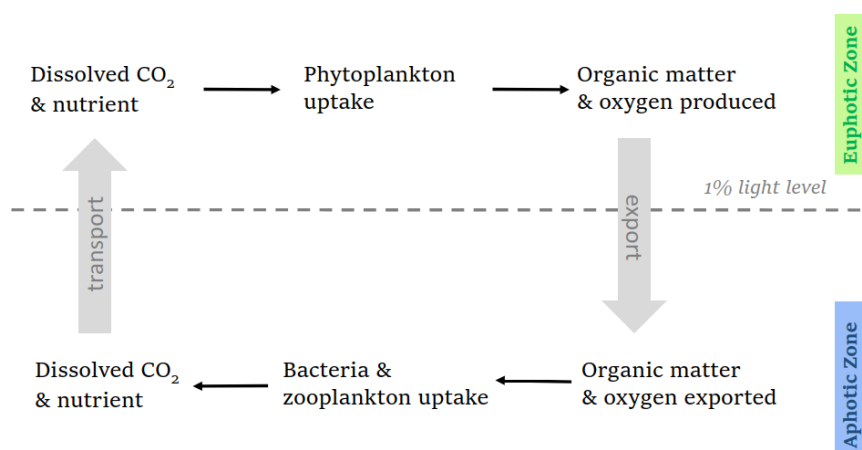


**Figure 1.7:** Schematic illustration of the relevant aspect related to the cycling of the organic matter within the ocean water column.

On a global scale, the highest nutrient-rich environment in the ocean is the deep water. Nutrients are transported to the surface within the water masses through different mechanisms, such as upwelling, convective overturning, and vertical mixing. Once at the surface, they are utilized by biological organisms. Due to this uptake, the euphotic zone has usually relatively low levels of nutrient concentrations. However, a high portion of organic matter is produced on the surface by biological activity and this is both exported to depth and, for a higher percentage, recycled within the surface. A schematic view of how organic matter cycles is depicted in Figure 1.7. The production of surface organic matter is divided into two components: a *regenerated production* and a *new production*. The former is produced with recycled organic matter within the surface ocean, while the latter is due to external sources, mostly upwelling or upward mixing of nutrients. A steady state corresponds to an equilibrium between the export of organic matter from the surface and new production.

To conclude, surface nutrient concentrations, phytoplankton biomass, and biological productivity based on phytoplankton are controlled primarily by the transport of nutrients within the ocean. For the purpose of this study and for the reasons underlined above, we will focus on how nitrogen is cycled through marine ecosystems.

**Oceanic nitrogen cycle** Nitrogen is an essential element for marine primary production because it is a fundamental building block for proteins. In seawater, nitrogen mostly occurs as inert dissolved  $N_2$  gas, reactive nitrogen, such as nitrate ( $NO_3^-$ ) and ammonium ( $NH_4^+$ ), dissolved organic compounds (DON) and particle organic compounds (PON). Most of the phytoplanktonic organisms are able to use both nitrate

## 1 Introduction

---

and ammonia as a source of inorganic N for photosynthesis. However, the use of ammonium instead of nitrate to produce organic matter is more common, because the reaction is energetically favored; thereby ammonium in the water column has a short lifetime [Sarmiento, 2006]. In contrast, nitrate is the most abundant form of nitrogen in seawater, in particular during winter when primary production is less active. As already noted, nitrate may disappear from the euphotic zone during blooms and, since the active uptake of phytoplankton is usually restricted to the euphotic zone, nitrate concentrations are greater at depth.

Nitrogen is transformed and transported within marine ecosystems in a complex pattern. Major sources of new nitrogen are *nitrogen fixation*, *vertical mixing* and *horizontal transport*. In contrast, mechanisms responsible for losses of nitrogen are *water transport*, *denitrification* and *phytoplankton uptake*. Eventually, some *regeneration processes* can make organically bounded nitrogen newly available. A brief explanation of each of the previous processes is given:

### Sources:

*Nitrogen fixation* : absorption of atmospheric  $N_2$  gas into organic nitrogen, typically converted in ammonia ( $NH_3^+$ ). Nitrogen fixation tends to be modest in relation to other nitrogen inputs in marine ecosystems;

*Vertical Mixing* : upward and downward motion that occurs as a result of the temperature gradients or the wind forcing at the surface of the ocean. This is the major source of nitrogen for the euphotic zone due to the advection of nutrient-rich deeper waters;

*Horizontal transport* : for the coastal area considered, it is associated with the intrusion of enriched nutrient waters from the Gulf Stream. Other horizontal transports can be associated with river runoff or with a tidal flux of groundwater carrying nutrients from land to coastal environment [Valiela, 2015].

### Losses:

*Water transport* : in general it is associated with physical processes such as tidal exchange, freshwater runoff in estuaries, and vertical and lateral transport in the open ocean;

*Denitrification* : it is process by which inorganic nitrogen compounds are converted to  $N_2$ . It represents the dominant loss term and it depends on the amount of available  $NO_3^-$  and DON, both supplied by external sources or *nitrification*. The latter is the process by which reduced nitrogen compounds (primarily  $NH_4^+$ ) are sequentially oxidized to nitrite ( $NO_2^-$ ) and nitrate. Denitrification and nitrification produce the pollutant gas nitrous oxide ( $N_2O$ ).

## 1.2 Biological productivity at shelf break fronts

*Phytoplankton uptake* : phytoplankton uses different nitrogen compounds present in the water column in order to produce the energy required for living and proteins that built up their cells.

### Recycling:

*Nitrogen regeneration* : nitrogen incorporated in particles is recycled by the release from bacteria, zooplankton, and fish. Also, it is recycled from the regeneration of DON. Regeneration can occur also in sediments: the organic nitrogen stored in the sentiments in a mineralized form is released into the overlying water. Ammonium is the most common inorganic form of nitrogen that emerges from regeneration [Valiela, 2015].

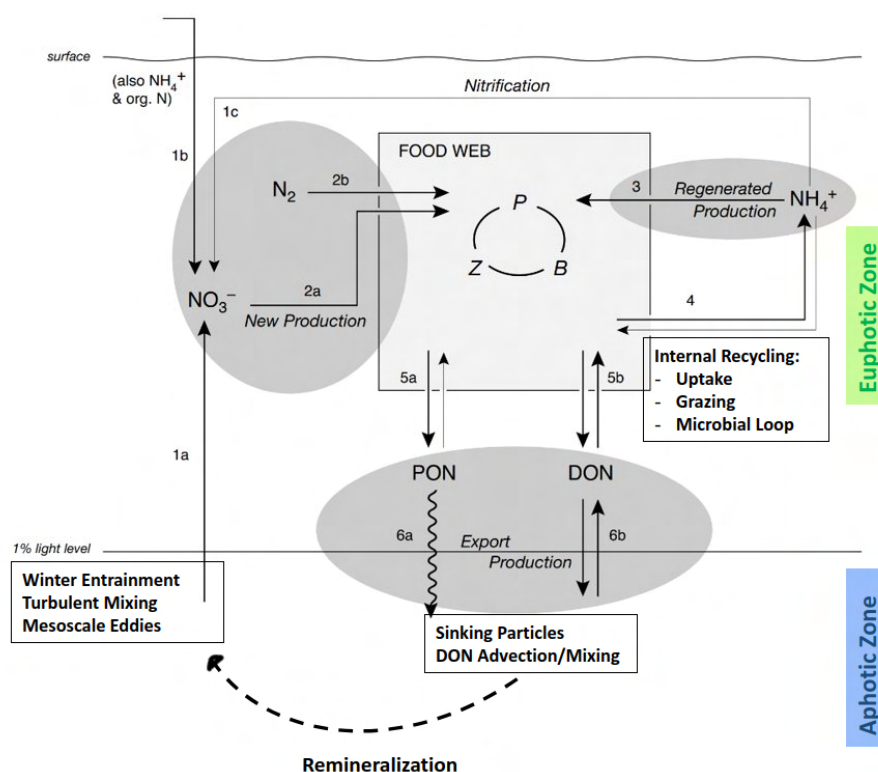


**Figure 1.8:** Schematic illustration of the paradigm for the cycling of nitrogen in the surface ocean. P is phytoplankton; Z and B are zooplankton and bacteria, respectively; PON and DON are particulate and dissolved organic nitrogen. Modified from Sarmiento [2006].

In Figure 1.8 a schematic illustration of how nitrogen is cycled in the surface ocean is represented. New nitrogen is supplied to the system either from below (pathway 1a) or from the atmosphere (pathway 1b) as well as through nitrogen fixation (pathway 2b). Regenerated production is driven by ammonium (pathway 3). The export of organic matter from the surface ocean is in the form of PON (pathway 6a) as well as DON (pathway 6b), some of which is recycled back into the part of the ecosystem before it can be exported (pathway 5). DON is both produced and recycled by the

## 1 Introduction

---

ecosystem (pathway 5b) as well as being exported from and possibly imported to the surface ocean (pathway 6b). Organic matter *rem mineralization*<sup>1</sup> by the ecosystem can go all the way to nitrate rather than just to ammonium (nitrification; pathway 1c). Bacteria are also able to consume nitrate.

**Chlorophyll- $\alpha$**  Surface chlorophyll distribution is the most commonly used index of phytoplankton biomass. Thus for all the considerations above, the growth and loss of phytoplankton can be modeled using the solution of the conservative equation:

$$\frac{\partial Chl}{\partial t} + \vec{V} \cdot \vec{\nabla} Chl = \frac{\partial}{\partial z} \left( K_v \frac{\partial Chl}{\partial z} \right) + \vec{\nabla}_H \cdot (K_H \vec{\nabla}_H Chl) + \frac{\partial Chl}{\partial t} \Bigg|_{Bio} \quad (1.6)$$

where:

- \*  $\frac{\partial Chl}{\partial t}$  is the chlorophyll variability observed;
- \*  $\vec{V} \cdot \vec{\nabla} Chl$  is the advective term. For this particular case can be written as:  
 $v \frac{\partial Chl}{\partial y} + w \frac{\partial Chl}{\partial z}$ ;
- \*  $\frac{\partial}{\partial z} \left( K_v \frac{\partial Chl}{\partial z} \right) + \vec{\nabla}_H \cdot (K_H \vec{\nabla}_H Chl)$  are the diffusive terms (that are small compared to the advective one and they can be neglected);
- \*  $\frac{\partial Chl}{\partial t} \Bigg|_{Bio}$  represents all the factors that affect the phytoplankton population: nutrients, light and temperature limitation, off-shore forcing, and zooplankton grazing. Hence, it can be written as:

$$\frac{\partial Chl}{\partial t} \Bigg|_{Bio} = \frac{\partial Chl}{\partial t} \Bigg|_{Growth} - \frac{\partial Chl}{\partial t} \Bigg|_{Removal} \quad (1.7)$$

The *growth* term is regulated by light availability, nutrient supply, and temperature; the *removal* term depends on grazing. However, the off-shore forcing can modify both of these terms, in particular creating a more favorable nutrient-rich environment or increasing upwelling.

For a complete understanding of the system, a set of equations should be provided for each component of the system.

### 1.3 Thesis objectives

The primary objectives of this study are first, to investigate the inter-annual variability of Chl- $\alpha$  at the MAB shelf break front and explore potential links to wind-driven dynamics; second, to test the hypothesis of frontal upwelling by examining the cor-

---

<sup>1</sup>Breakdown or transformation of organic matter into its simplest inorganic forms.

relation between enhanced primary production at the shelf break front and nutrient transport induced by BBL detachment; third, to explore the interaction between the Gulf Stream submesoscale instabilities impinging on the shelf and BBL detachment. The work is organized as follows:

1. **Inter-annual characterization of surface Chl- $\alpha$  variability:** we analyze the inter-annual variation of surface Chl- $\alpha$  in the MAB region from 2003 to 2020. This analysis is based on satellite data products, providing insights into long-term Chl- $\alpha$  trends.;
2. **Inter-annual analysis of environmental conditions:** we conduct an inter-annual examination of environmental factors, including sea surface temperature, salinity, horizontal velocities, and surface winds, using reanalysis datasets. Particular interest is given on assessing the correlation between Ekman wind-driven dynamics and the occurrence of surface Chl- $\alpha$  blooms;
3. **Variability of the MAB shelf break front:** We provide a comprehensive description of the variability of the MAB shelf break front, given by data collected during three distinct oceanographic cruises. These data are instrumental in investigating the hypothesis of nutrient transport within the BBL using two distinct methodologies: 1) accumulated properties change (Section 2.1.1); 2) along isopycnals change in properties (Section 2.1.2).

The datasets and the methods used are described in detail in Chapter 2. The inter-annual characterization of the region is shown in Chapter 3; the results related to the physical driver of Chl- $\alpha$  variability are reported in Chapter 4. Conclusions are summarized in Chapter 5.



# Chapter 2

## Data and methods

As exposed in Chapter 1, one of the main objectives of this work is to test the hypothesis of nutrient transport within the BBL detachment at the shelf break front. If this hypothesis is verified, a biological response in terms of enhanced Chl- $\alpha$  concentration is expected. This chapter gives a general overview of the datasets and methods employed for the analysis.

The local variability in the region of interest has been studied using *in situ* data collected during three oceanographic cruises (Section 2.1). With these data has been tested the above-mentioned hypothesis using two different methods: accumulated properties changes and along isopycnals change in properties, respectively described in Sections 2.1.1 and 2.1.2. In addition, to better understand the processes characterizing the MAB shelf break region, the inter-annual variability for the period 2003 - 2020, has been investigated using remote sensing measurements of surface Chl- $\alpha$  (Section 2.2) and reanalysis datasets for the environmental conditions: sea surface temperature, salinity, currents, and surface winds at 10 m height (Section 2.3).

### 2.1 Field *in situ* data

*In situ* measurements were collected during three different oceanographic cruises carried out in the SPIROPA project:

1. AR29 of the *R/V Neil Armstrong* from the 16th to the 28th April 2018;
2. RB1904 of the *R/V Ronald H. Brown* from the 12th to the 25th May 2019;
3. TN368 of the *R/V Thomas G. Thompson* from the 5th to the 19th July 2019;

From all the sections available, only the synoptic transects along 70.8°W, north-south-oriented, and cross-shelf were chosen. Each transect was repeatedly sampled across the shelf break with 14 stations  $\sim 7$  km apart, to capture the mean state and

## 2 Data and methods

the variability of the front. The sampling area with the stations' location is reported in Figure 2.1. This area is remarkable for that particular region of the MAB: it covers the typical location of the front between 100 m and 200 m isobaths and can capture the passing front meanders of  $\sim 15$  km amplitude and 4-day period [Gawarkiewicz *et al.*, 2004].

At each station, vertical CTD profiles were taken to measure the hydrographic properties such as temperature, pressure, salinity, and density. Discrete seawater samples were collected at 10-m intervals, using 24 10-L Niskin bottles mounted on the CTD rosette. The rosette was equipped with a SeaBird 911 CTD system, a WetLabs FLNTURTD fluorometer, a BioSpherical Instruments sensor for photosynthetically active radiation (PAR), and a WetLabs C-Star beam transmissometer. Temperature, salinity, potential density, and fluorescence were measured on all CTD casts.

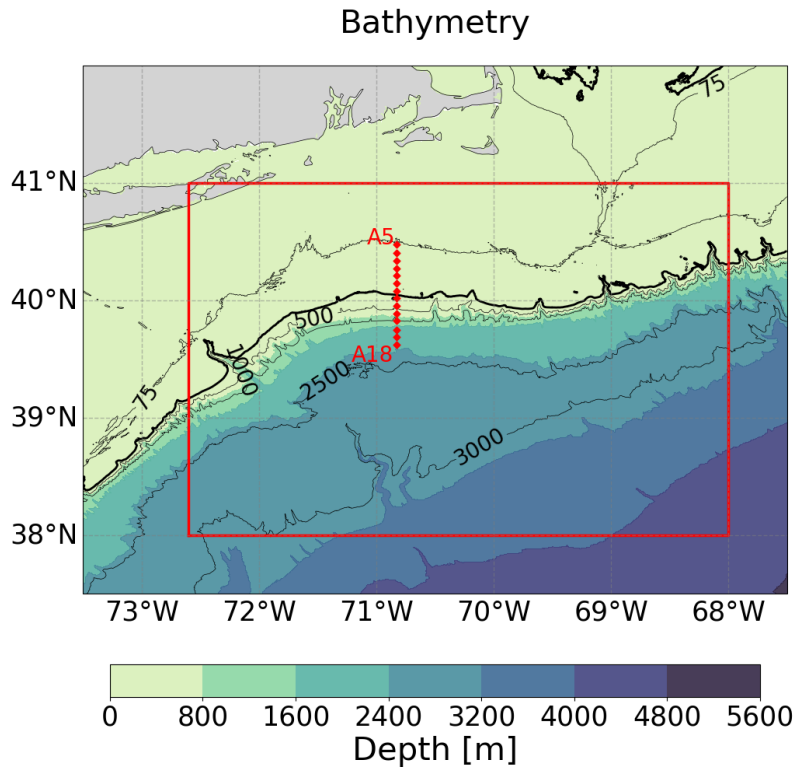


**Figure 2.1:** Bathymetry distribution of the MAB region. The red box corresponds to the area considered for the analysis in Chapter 3. Red diamonds represent the sampling stations' location. The thick black line represents the shelf break at 200 m isobath.

The concentration of nutrients (nitrate, phosphate, silicate), chlorophyll, and particulate organic nitrate (PON) were measured throughout discrete seawater sampling. Nutrient concentrations were determined by filtering seawater samples through  $0.4 \mu\text{m}$  polycarbonate filters, which were frozen in acid-washed polyethylene bottles, and analyzed post-cruise at the Woods Hole Oceanographic Institution Nutrient Analyt-

ical Facility. Chlorophyll concentrations were obtained by filtering duplicate water sampling through GF/F Whatman filters under low vacuum (0.45 atm), and immediately frozen in liquid nitrogen. Post-cruise they were thawed in 90% acetone and analyzed by standard fluorometric methods. PON concentrations were determined by filtering 0.25-2.0 L of seawater under low vacuum through precombusted (450 °C for 2 h) Whatman GF/F filters, stored in precombusted glass vials, dried at 60 °C, and analyzed on a Costech ECS 4010 elemental analyzer.

CTD fluorescence ( $F_{CTD}$ ) is an indirect measure of chlorophyll pigmentation and, thereby can be a proxy for phytoplankton abundance. To obtain a more precise estimation,  $F_{CTD}$  was converted into chlorophyll- $\alpha$  ( $Chl_{CTD}$ ) concentration using a regression between CTD fluorescence measurements and chlorophyll- $\alpha$  + Phaeo- $\alpha$ <sup>1</sup> concentration extracted from Niskin bottles:

$$Chl_{CTD} = mF_{CTD} + q \quad (2.1)$$

The regression coefficients for each cruise are reported in Table 2.1.

Cruise	Slope [ $m$ ]	Intercept [ $q$ ]	$R^2$	RMSE
AR29 - April 2018	0.99	0.03	0.94	0.83
RB1905 - May 2019	1.14	-0.11	0.90	0.64
TN368 - July 2019	1.09	-0.04	0.89	0.70

**Table 2.1:** CTD fluorometer vs chlorophyll- $\alpha$  calibration coefficients and regression statistic.

### 2.1.1 Accumulated properties change algorithm

To reveal the presence of BBL detachment it has been followed the criteria explained in Chapter 1.1.1. The leading idea is that the isopycnals along with the water is transported both off-shore and upward, should be characterized by small lateral accumulated changes in properties (APC). Thereby, the gradient of a given property, calculated in the cross-shelf direction should have some minima close to the bottom. For the present study, accumulated salinity (ASC), temperature (ATC), and nitrate (ANC) changes have been considered. It has already been proved by [Gawarkiewicz et al. \[2004\]](#) that the ATC technique accurately works for the MAB frontal system and it can detect the detachment of the BBL. Therefore, this method has been applied also to a biocheogemical variable (nitrate concentration) to link the physical process with the biological activity.

The algorithm used was the one developed by [Linder \[2005\]](#) and it computes the

<sup>1</sup>Non-photosynthetic pigment which is a degradation product of chlorophyll pigments. It is commonly formed during and after phytoplankton blooms.

## 2 Data and methods

---

APC sections via a multistep process [Gawarkiewicz et al., 2004]:

- (i) Extraction from each CTD cast of the significant variables: temperature, potential density ( $\sigma_\theta$ ), salinity, and nitrate concentrations;
- (ii) Gridding of the potential density field at higher resolution using a 2D regular grid spacing 1.5 km in  $y$  direction (cross-shelf distance, positive offshore) and 5 m in  $z$  (vertical distance, positive upward). The gridding is performed using a Laplacian-spline interpolation;
- (iii) Each section is contoured at given small density contours ( $\Delta\sigma_\theta = 0.01 \text{ kg/m}^3$ ), and the  $(y, z)$  coordinates are computed for each contour;
- (iv) Extraction of the bottom depth considering the deepest local depth for each CTD cast building the transect;
- (v) Only those isopycnals intersecting the bottom are considered. Thus, a set of  $(y, z)$  coordinates representing the isopycnals originating from the bottom and terminating at either the surface or the off-shore boundary of the section, is obtained;
- (vi) Interpolation of each variable (temperature, salinity, and nitrate concentration) along the selected isopycnals using the calculated  $(y, z)$  coordinated;
- (vii) Calculation of the gradient of each interesting variable along the isopycnals ( $\sigma$ ) in the off-shore direction. For example, for the temperature ( $\theta$ ):

$$\frac{d\theta}{dy} = \theta(\sigma(y_0)) - \theta(\sigma(y_0 + \Delta y)) \quad (2.2)$$

where  $y$  is the cross-shelf direction,  $y_0$  is the starting coordinate and  $\Delta y$  is the grid spacing in the off-shore direction;

- (viii) Estimation of ASC, ATC, and ANC integrating the absolute value of the gradients, along each isopycnal, starting with a value of zero at the bottom:

$$\text{ATC} = \int_{z_{b_\sigma}}^{z_{s_\sigma}} \left| \frac{d\theta}{dy} \right| dz_\sigma \quad (2.3)$$

in which  $z_{b_\sigma}$  and  $z_{s_\sigma}$  are the vertical coordinates, from the bottom to the surface, along the selected isopycnal and  $dz_\sigma$  in the vertical displacements along the isopycnals.

- (ix) Eventually, these irregularly spaced values of APC in the cross-shelf plane, are regridded and contoured like any other properties.

### 2.1.2 Along isopycnals change in properties

Related to the process of BBL detachment, it has been hypothesized that a transport of nutrients toward the surface is associated with the detaching mechanism, thus carrying nutrients from the deep nutrient-rich environment to the surface, where they can be used by phytoplankton to produce organic matter. For this purpose the difference ( $\Delta_{\text{surface}} - \Delta_{\text{bottom}}$ ) between the concentrations of  $\text{NO}_3^-$ , PON, and chlorophyll- $\alpha$  (Chl- $\alpha$ ) has been calculated along the isopycnals associated with: the detaching of the BBL and with the isopycnals at the center of the frontal surface, identified by the 34.5 isohaline [Linder and Gawarkiewicz, 1998]. The analysis has been performed by looking at the process on a 2D plane (cross-shelf and off-shore direction vs depth), thus any contribution of lateral transport has been neglected. With this approximation, the relations among the biogeochemical tracers are straightforward: if  $\text{NO}_3^-$  decreases (it is consumed by phytoplankton to perform photosynthesis), PON (nitrogen contained in living material and nitrogen in detritus) shall theoretically increase of the same order of magnitude:

$$-\Delta\text{NO}_3^- \approx \Delta\text{PON} \quad (2.4)$$

If nitrogen is utilized, more Chl- $\alpha$  is produced, even if the relationship between the two is not one-to-one as in the former case. Hence:

$$-\Delta\text{NO}_3^- \sim \Delta\text{Chl-}\alpha \quad (2.5)$$

For coastal areas, it is usually estimated that the ratio between carbon (C) and chlorophyll is C:Chl = 50:1. From the *Redfield's ratio*: C:N:P = 106:16:1, the proportion between carbon and nitrate can be evaluated. However, it is valuable to mention that the given C:Chl ratio is an averaged estimation that can be strongly affected by the differences among phytoplankton species as well as photoadaptation and nutrients distribution [Cullen, 2015].

The key points of this methodology are two:

1. The choice of the target isopycnals along with calculating the differences ( $\Delta$ s);
2. Defining the isopycnals' coordinates representing the bottom end and top end of the  $\Delta$ s estimation.

The target isopycnals were chosen as follows: the isopycnal intersecting the foot of the mean location of the front (corresponding to the bottom end of the 34.5 isohaline) in the BBL, and the isopycnal found in the center of the ANC minima. Depending on the stratification condition it was found that the range of these isopycnals was

## 2 Data and methods

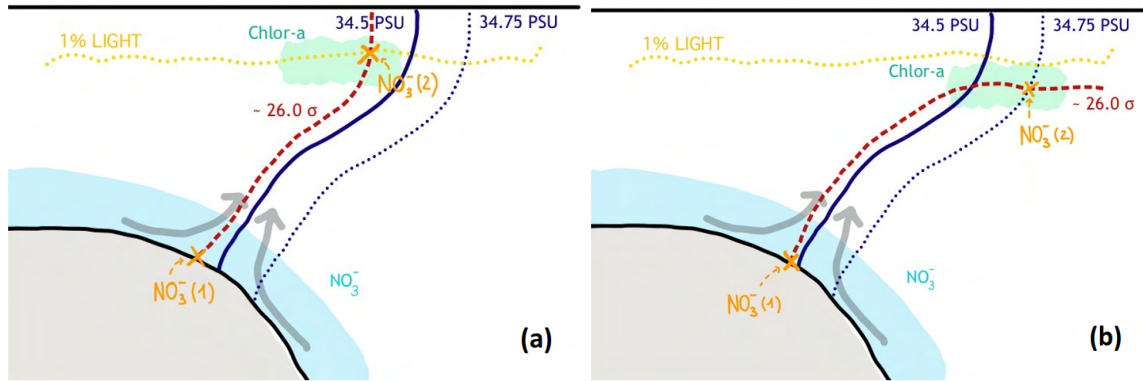


**Figure 2.2:** Methodology used for  $\Delta s$  estimation. Panel (a): low stratified conditions, target isopycnal (dashed red line) outcropping in the euphotic zone (dotted yellow line). Panel (b): high stratified conditions, target isopycnal crossing the off-shore side of the front (dotted blue line, corresponding to 34.75 PSU). In both of the panels, the blue line represents the mean location of the front (34.5 PSU). The orange crosses represent the two locations used for the calculation. The bottom convergence is shown by the two gray arrows.

[26.0 - 26.6]  $\sigma$ . For the bottom end of the target isopycnals it has been chosen the location where they were hitting the bottom; instead for the top end two different criteria have been applied depending on the strength of the stratification. During typical low stratified conditions (winter and early spring), the isopycnals are steep, outcropping at the surface and parallel to the frontal surface due to the mixed layer depth deeper in the water column. Thereby, it has been chosen to select the location where the isopycnal was outcropping in the euphotic zone, as shown in Figure 2.2 (a). The euphotic zone was estimated as the level corresponding with the 1% of surface irradiance. In the next paragraph it is enlighten the method used for the calculation. It has been decided to exclude the region above the euphotic zone to filter out the high productivity associated with it and focus only on the area where the influence of BBL detachment was greater, as emerged by the analysis of the APC sections. Moreover, below the euphotic depth the light availability is limited, thus any primary production should be mainly driven by repleted nutrient concentration. In contrast, when the stratification is greater (late spring and summer), the isopycnals are shallower, bending below both the strong thermocline and the euphotic zone, thereby the former criterion was not suitable anymore. For these sections it has been chosen the location where the isopycnal was crossing the 34.75 PSU, therefore extending the  $\Delta s$  calculation toward the off-shore side of the front (see Figure 2.2 (b)).

### Euphotic depth estimation

In the previous section it has been exposed the importance of the correct identification of the coordinates for the  $\Delta s$  calculation. The method is very sensitive to this; the estimation of the depth of the 1% light level of the surface irradiance is a

crucial factor. To perform that the technique proposed by [Oliver et al. \[2021\]](#) has been followed. The surface irradiance ( $I$ ) at each depth  $z$  was determined for each CTD cast by solving the ordinary differential equation:

$$\frac{\partial I}{\partial z} = -k_d I \quad (2.6)$$

where  $k_d$  is the light extinction coefficient. In this particular case  $k_d = k_z + k_p(\text{Chl-}\alpha)$ , in which  $k_z$  is the light attenuation of clear seawater ( $k_z = 0.04 \text{ m}^{-1}$ ), and  $k_p$  is the light attenuation from phytoplankton biomass, which was significantly different among the three cruises. Thus, for each of these, the  $k_p$  value was derived using CTD profiles of PAR from daytime casts, determining for each of these the value of  $k_p$  that was closest to the 1% light depth to that determined by the ratio of PAR sensor on the rosette and surface PAR sensor values. In the end, a mean  $k_p$  among all obtained from each cast was used for the whole transect. In this way, each transect had its representative  $k_p$  value, ranging from 0.1 to 0.4  $\text{m}^{-1}$ , depending on the different local conditions of phytoplankton attenuation.

To numerically solve the equation 2.6, it has been applied the *forward Euler* method:

$$I_{i+1} = I_{i-1} + \frac{\partial I}{\partial z} \cdot \Delta z$$

which was initialized given the value of the measured CTD PAR at the surface ( $I_0$ ).

## 2.2 Satellite Chlorophyll- $\alpha$

The solar radiation entering the Earth's System is partially absorbed by the atmosphere, backscattered to space, and a fraction arrives at the Earth's surface that can be absorbed or reflected. In particular, it is possible to measure with satellite the emitted or reflected radiation from the ocean surface in order to quantify its properties. This radiation leaving the ocean surface determines the color of the ocean. Ocean's color depends on how light interacts with the materials in the water. Most of the world's oceans appear blue because the water particles absorb the red light component of the visible light spectrum, thereby the blue light component is the one remaining and reflected back out of the water. In addition, water molecules and other particles suspended in the ocean, scatter blue light more than light of other colors. However, in some places, the ocean can be green, or even yellow to brown. The main factors affecting the oceans' color are: dissolved organic matter, phytoplankton with chlorophyll pigments, and marine sediments. In particular, chlorophyll- $\alpha$  are pigments contained in phytoplankton that are able to absorb blue and red light to carry out photosynthesis (see Section 1.2), thus shifting the color of the ocean's

## 2 Data and methods

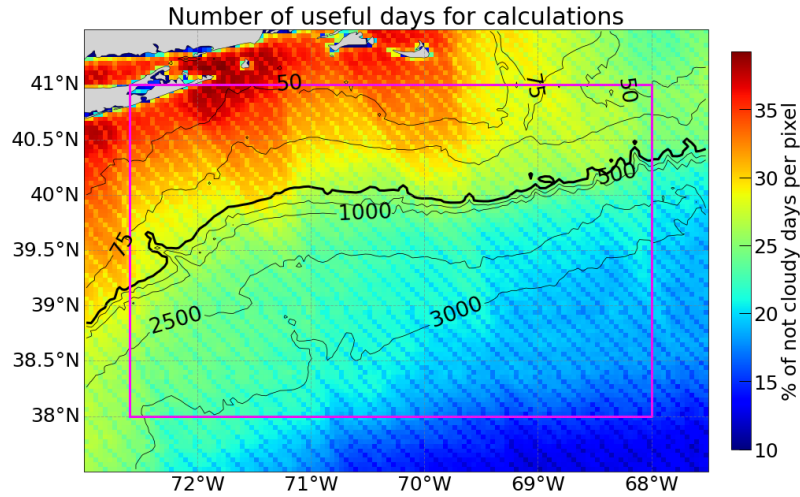


**Figure 2.3:** Percentage of not cloudy days per pixel over the area of interest (magenta box) within the period 2003 - 2020. The black solid contour represents the shelf break at 200 m isobath.

water toward the green part of the spectrum. This green emission can be measured with specific sensors mounted on satellites, providing an estimation of primary production.

For this work, it has been employed surface Chl- $\alpha$  concentrations (*Ocean Color Index* (OCI) algorithm) provided by the Level 3 data product derived from the *Moderate-Resolution Imaging Spectroradiometer* (MODIS) mounted on NASA’s Aqua satellite (EOS PM), launched in 2002. MODIS is a passive sensor<sup>2</sup> collecting data across 36 spectral bands spanning the visible and infrared light range [0.4 - 14.4  $\mu\text{m}$ ] and providing information about the atmospheric column and the surface of the ocean. This product is available on the NASA *Ocean Color Website* [NASA Goddard Space Flight Center, 2022], on a daily basis, mapped on a uniform grid with a 4 Km resolution. The main issue related to this product is the presence of clouds, which is not treated with some post-processing algorithm. Hence, the data coverage is not uniform over the selected area, for the whole period of interest spanning from 2003 to 2020. Specifically, for the shelf break region highlighted by the solid black contour in Figure 2.3, the dataset contains an available proportion of not cloudy days per pixels amounting to approximately 30%. In order to solve this problem, a gap-filling interpolation has been employed in order to obtain a continuous time series of spatially averaged Chl- $\alpha$  concentrations, when needed for the analysis.

<sup>2</sup>Sensor able to gather radiation that is emitted or reflected by an area of interest.

### 2.2.1 Space-time analysis method

Any physical signal can be decomposed into a number of finite frequencies  $f$  or periods  $\tau = \frac{1}{f}$ . How the power of the signal (or the time series) is distributed into frequency components can be described with a *Power Spectral Density* (PSD). In this work, this method has been applied to the interpolated, continuous time series of the spatially averaged concentration of surface Chl- $\alpha$  in order to identify dominant frequencies within the signal. The PSD amplitude has been identified with the squared value of the signal. To calculate the PSD, the *Welch's methods* [Welch, 1967] was used, which involves dividing the signal into overlapping segments, applying a window function to each segment, computing the spectral density (or periodogram) in the frequencies domain of each segment, and finally averaging the periodograms to obtain the estimate of the PSD. This method has been implemented using the function `welch` from Python's statistical module `scipy.signal` [Virtanen et al., 2020].

## 2.3 Reanalysis datasets

Atmospheric and ocean reanalyses are homogeneous 3D gridded representations of the physical state of the global oceans and Earth's atmosphere covering several decades, produced with a numerical model constrained with observational data from satellite and *in situ* measurements. This method is called *data assimilation* and it allows for improvement in the prediction of the state of the atmosphere/ocean by combining a previous forecast with a newly available observational estimate, in a way that produces a new best prediction, from which an updated, improved forecast is issued. For this work, two different reanalyses have been used: the Global Ocean Ensemble Reanalysis for the physical variables in the ocean (temperature, salinity, horizontal velocities) and ERA5 for the surface winds.

**Global Ocean Ensemble Reanalysis** The *Copernicus Marine Environment Monitoring Service* (CMEMS) Global Ocean Ensemble Reanalysis is a multi-model ensemble approach, that uses four different reanalyses to create the ensemble:

1. GLORYS2V4 from Mercator Ocean;
2. ORAS5 from *European Center for Medium-Range Weather Forecast* (ECMWF);
3. GloSea5 from Met Office;
4. C-GLORSv7 from *Euro-Mediterranean Center on Climate Change* (CMCC).

Each of these provides a different daily prediction of the state of the ocean, thus uncertainties or error bars can be estimated [CMEMS, 2023]. Data is available from

## 2 Data and methods

---

1st January 1993 to 31st December 2020. It has a horizontal resolution of  $0.25^\circ \times 0.25^\circ$  and the ocean is resolved in 75 vertical levels. In this work, only the first level has been analyzed (surface level). For each of the reanalyses the forcing at the surface is given by the reanalysis ERA-interim<sup>3</sup> [Dee, 2022], jointly assimilated with altimeter data (sea level anomaly), satellite sea surface temperature, sea ice concentration, and *in situ* temperature and salinity vertical profiles. All model components of the reanalysis are based on different releases of NEMO3 (*Nucleus for European Modelling of the Ocean*) [Gurvan et al., 2019].

This dataset has been used to characterize the inter-annual variability of the physical variables in the ocean. 3D gridded daily field for each of the variables of interest were provided as NetCDF files, although monthly means were computed for the analysis.

**ERA5** ERA5 is the fifth generation ECMWF reanalysis for the global climate and weather for the past 8 decades [ECMWF, 2023]. It has a horizontal resolution of  $0.25^\circ \times 0.25^\circ$  and the atmosphere is vertically resolved using 137 levels from the surface up to a height of 80 Km. Hourly or monthly mean data are available from 1940 to the present. For the present work, monthly estimates on a single level (10 m height from the surface) of the zonal and meridional components of the wind were used. These have been employed to test if the inter-annual variability of the winds could be associated with the variability of Chl- $\alpha$  blooms. In particular, winds can transport water off-shore, leading to upwelling mechanisms for continuity. For the area of interest, it has been verified that the meridional component of this off-shore transport, known as *Ekman transport*, has greater impact on the system compared to the zonal component. The meridional Ekman transport was calculated as follows:

$$M_y = -\frac{\tau_w^x}{f} = -\frac{\rho_a C_d |\vec{u}(10)| u_{10}}{f} \quad (2.7)$$

where  $f = 1.45 \times 10^{-4} \text{ s}^{-1}$  is the *Coriolis factor*,  $\rho_a$  is the density of the air,  $C_d = 1.5 \times 10^{-3}$  is the drag coefficient,  $u_{10}$  is the zonal wind component at 10 m from the surface and  $\vec{u}(10) = \sqrt{u_{10}^2 + v_{10}^2}$  is the magnitude of the wind at 10 m. An estimation of upwelling associated with the Ekman transport can be derived from the *Upwelling Index* (UI), which is a measure of westerlies vs. easterlies winds (as calculated in Oliver et al. [2022]):

$$\text{UI} = \frac{\tau_x}{\rho f} \quad (2.8)$$

with  $\tau_x$  being the  $u$  component of the wind stress,  $\rho$  the water density, and  $f$  the *Coriolis factor*. As most of the shelf break in our region is approximately zonally

---

<sup>3</sup>ERA-Interim was a global atmospheric reanalysis from 1979 to 31st August 2019, developed by ECMWF. It was the predecessor of ERA5.

oriented, we use positive (negative)  $\tau_x$  as the westerlies (easterlies) wind stress.

## 2.4 Bathymetry

For the present work, it is fundamental to be able to distinguish, in both satellite images and reanalysis fields, the different oceanic domains: the *continental shelf*, for depths inferior to 75 m; *shelf break region* between 75 m and 1000 m, and *slope region* when bathymetry is greater than 1000 m. For this purpose, it has been employed the *General Bathymetric Chart of the Ocean 2022* (GEBCO) [GEBCO, 2022]. This is a global, high-resolution (15 arcsecs, around 450 meters squared at the Equator) product, combining several data, such as ship-based surveys, airborne, and satellite altimetry. To adapt the GEBCO bathymetry to the lower resolution of the previous datasets, a two-dimensional interpolation has been performed.



## Chapter 3

# Characterization of inter-annual chlorophyll- $\alpha$ variability

The inter-annual variability of the surface concentration of chlorophyll (Chl- $\alpha$ ), has been investigated using satellite images (Section 3.1). In particular, monthly and annual mean have been performed within the period 2003-2020 to analyze the spatially averaged time series (Subsection 3.1.1) and the power spectral density (See section 3.1.3) of the mean surface Chl- $\alpha$  concentration. In addition, the variability of the environmental conditions that give rise to the observed seasonal fluctuations in Chl- $\alpha$  concentration has been examined in Section 3.2, employing reanalysis datasets.

### 3.1 MODIS surface Chlorophyll- $\alpha$ concentration

The annual average of surface Chl- $\alpha$  concentrations for each year is depicted in Figure 3.1, while Figure 3.2 illustrates the monthly mean values within the specified time frame. It is observed that annually, the highest mean concentration of Chl- $\alpha$  ( $> 1.5 \text{ mg/m}^3$ ) is close to the coast, associated with river runoff which carries nutrients and organic matter into the water allowing algae to grow. On the contrary, the lowest concentration is in the open ocean ( $\sim 0.5 \text{ mg/m}^3$ ). Every year there is a strong local maximum in the northern part of the region, around  $70^\circ \text{ W}$ , which was particularly intense for the years 2009 and 2014. The distribution of the Chl- $\alpha$  is quite constant and uniform through the years, even though 2011, 2014, 2015, and 2018 presented significant local minima ( $\sim 0.2 \text{ mg/m}^3$ ) over the open ocean area. From the monthly mean concentration, it is evident the seasonal and semi-seasonal cycle of the Chl- $\alpha$  concentration, corresponds to April and November blooms. The two mechanisms leading the two maxima in concentrations are different. The one of April is related to the increasing light availability that allows phytoplankton to grow

### 3 Characterization of inter-annual chlorophyll- $\alpha$ variability

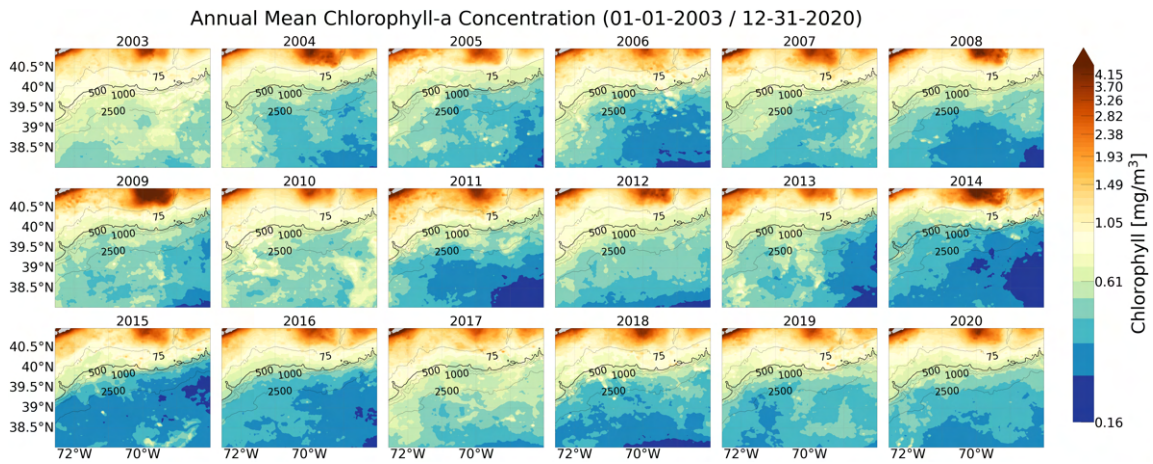


**Figure 3.1:** Annual mean chlorophyll- $\alpha$  concentration in the region of interest, from 2003 to 2020. Gray contour levels represent bathymetry; the bold black line is the shelf break at 200 m isobath. Note the logarithmic color scale.

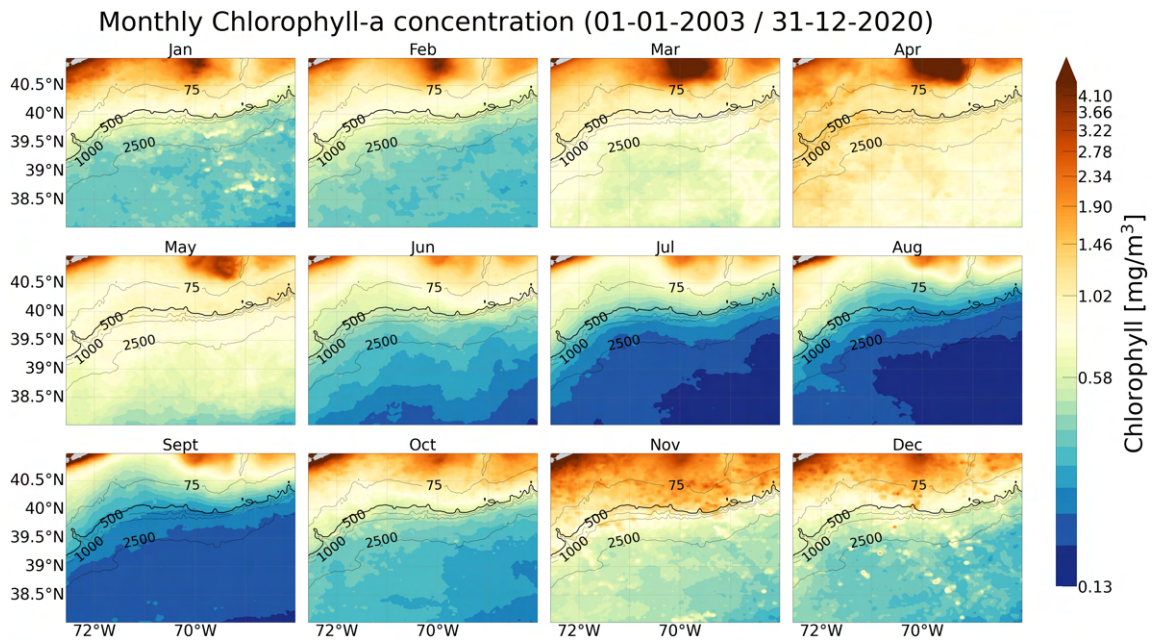


**Figure 3.2:** Monthly mean Chl- $\alpha$  concentration in the region of interest, from 2003 to 2020. Gray contour levels represent bathymetry; the bold black line is the shelf break at 200 m isobath. Note the logarithmic color scale.

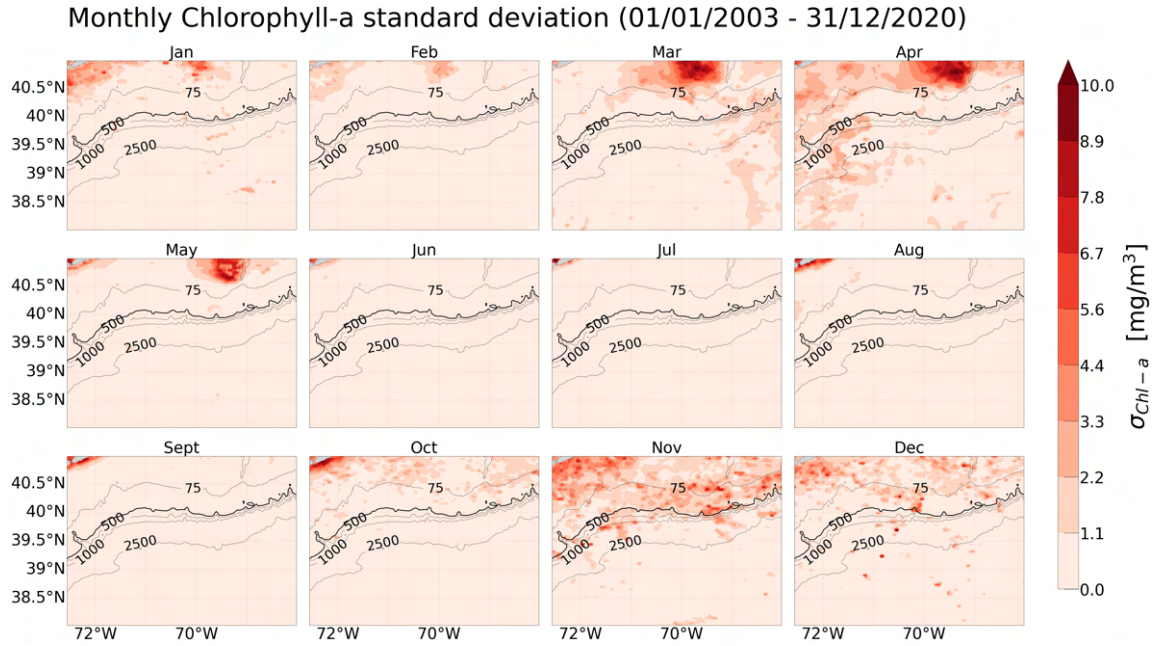


**Figure 3.3:** Monthly standard deviation of chlorophyll- $\alpha$  concentration. Gray contour levels represent bathymetry; the bold black line is the shelf break at 200 m isobath.

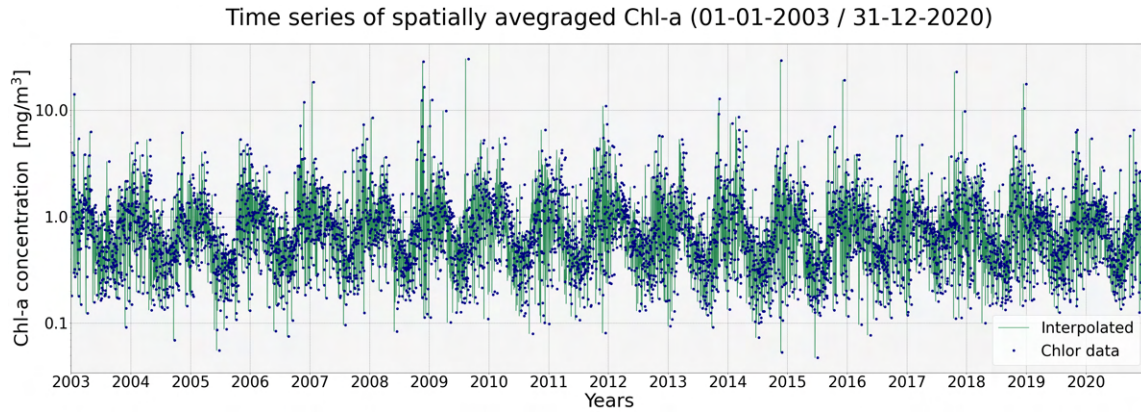
on a nutrient replete surface, due to the remaining mixing from the winter season. As soon as the spring bloom grows, the nutrients are utilized leaving a surface water layer depleted. With the beginning of autumn and the strengthening of the winds, the mixed layer depth increased mixing water to a greater depth and replenishing the nutrients at the surface. With this new enriched environment, the second seasonal bloom can occur even if less intense than the first one. During the summer season, the Chl- $\alpha$  is at its minimum, then it grows during the autumn and diminishes again in winter.

The seasonal and semi-seasonal cycle variability is evident also in the monthly distribution of Chl- $\alpha$  standard deviation reported in Figure 3.3. The local maximum present in May and April is associated with the seasonal cycle, instead, the higher values for November and December represent the semi-seasonal bloom, which appeared to have a lower magnitude but a greater spread all over the shelf area, compared to the spring one. The former has the maximum in  $\sigma_{chlor-\alpha} > 5 \text{ mg/m}^3$  constrained to a restricted area close to 75 m bathymetry. These differences in how the maxima concentrations are distributed reflect the two different mechanisms governing the process.

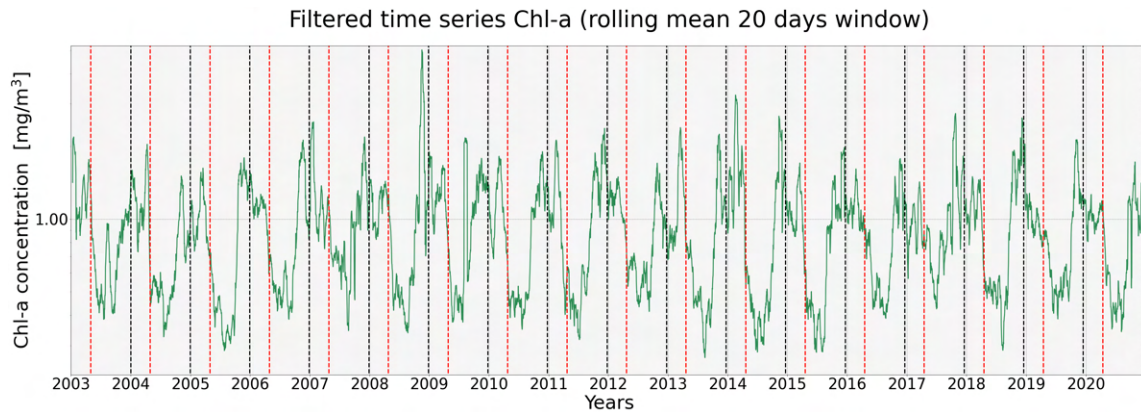
#### 3.1.1 Time series of spatially averaged Chl- $\alpha$

The time series of spatially averaged Chl- $\alpha$  surface concentration has been investigated for the whole period 2003-2020. For each day, a mean value has been calculated

### 3 Characterization of inter-annual chlorophyll- $\alpha$ variability



(a) The green line is the interpolated mean trend of the spatially averaged Chl- $\alpha$  concentration; the blue dots represent the raw data. Note the logarithmic scale on the y-axis.



(b) Filtered time series of mean spatially averaged Chl- $\alpha$ , with a 20-day rolling mean window. The red dashed vertical lines repeat every 120 days (corresponding to the end of April); the black ones every 365 days (end of December). Note the logarithmic scale on the y-axis.

**Figure 3.4:** Time series of mean spatially averaged Chl- $\alpha$  surface concentration in 2003- 2020.

by averaging the concentration over the whole area considered. To compute the continuous time series, the raw data have been interpolated to fill the missing values corresponding to missing days. Once a non-discontinuous time series has been obtained, it has been applied a rolling mean with a 20-day window to smooth the intrinsic fluctuations. In Figure 3.4 the results are shown. The double-peaked mean trend clearly revealed the presence of a seasonal and semi-seasonal cycle, which repeats every year. The maxima do not always correspond to the end of April or the end of December: sometimes are shifted earlier, sometimes after, as shown in Figure 3.4b. Additionally, a spatial averaging procedure was employed to determine the Chl- $\alpha$  concentration for each month over the period from 2003 to 2020. The resultant monthly mean spatially-averaged data is depicted in Figure 3.5. The values confirm that the Spring maximum occurs in April, and it is an absolute maximum

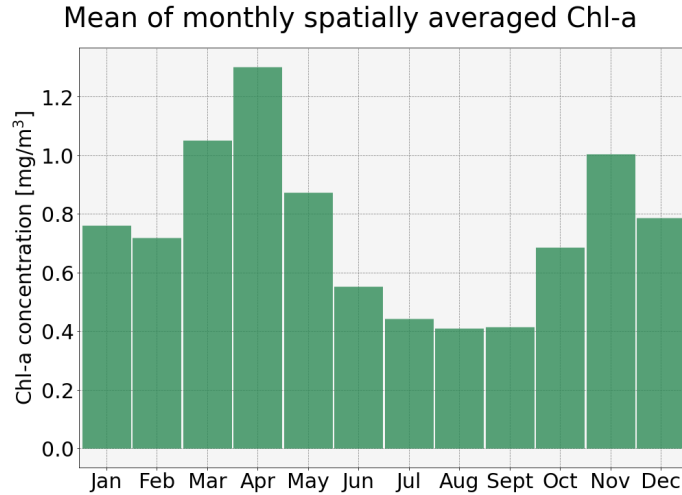


**Figure 3.5:** Mean of the monthly spatially averaged chlorophyll- $\alpha$  within the period 2003 - 2020. It represents the mean values for each month for the whole area.

( $\sim 1.3 \text{ mg/m}^3$ ) preceded by a second local maximum in March ( $\sim 1.1 \text{ mg/m}^3$ ). The Autumn maximum takes place in November but it is lower than the April's one ( $1.0 \text{ mg/m}^3$ ). During the summer months, from July to September there is the minimum surface concentration ( $0.4 \text{ mg/m}^3$ ).

#### 3.1.2 Variability of surface chlorophyll- $\alpha$ concentration

It has been demonstrated that the seasonal surface Chl- $\alpha$  blooms occur mainly on the shelf (Section 3.1). Moreover, local and transient enhancements at the shelf break can take place (Oliver et al. [2022], Zhang et al. [2013]). They have been defined as days when the surface Chl- $\alpha$  concentration at the shelf break exceeds that of both the concentration over the shelf and the slope. However, it is known that they do not appear in long-term averages of the Chl- $\alpha$  concentration at the MAB shelf break and the mean Chl- $\alpha$  is not in general enhanced compared to the seasonal variability. To further investigate this aspect the temporal evolution of the distribution of the mean surface Chl- $\alpha$  concentration, has been investigated using *Hovmöller diagrams*. The time variable has been recorded along the ordinate, while the abscissa represents some significant depth values. In particular, 100 m isobath has been used as the indication of the beginning of the shelf break, and 1000 m isobath represents the beginning of the slope region. To avoid the area closer to shore, which usually has the highest concentration due to land runoff of nutrients, only the area with depths between 50 m to 3000 m has been considered. Hence, the region considered for these calculations is delimited by the red box outlined in Figure 3.6. The variability within the region is large, thereby to capture the signal using mean surface concentrations, the area has been sampled dividing the bathymetry distribution into 51 bins in

### 3 Characterization of inter-annual chlorophyll- $\alpha$ variability

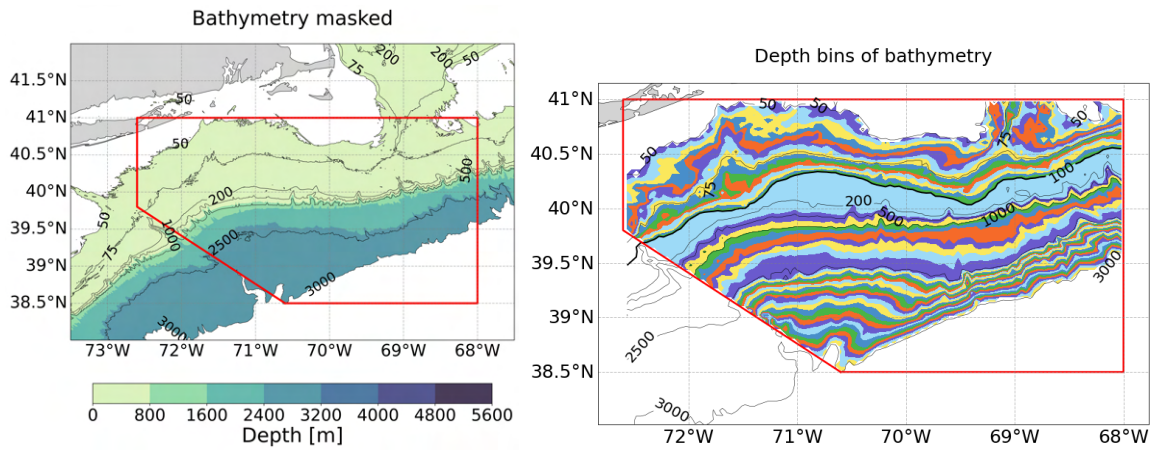


**Figure 3.6:** On the left: bathymetry distribution masked selecting only depths from 50 m to 3000 m. The red box indicates the area in which the calculation has been performed. On the right: distribution of the depth bins of bathymetry.

order to reproduce the mean bathymetry profile, following the procedure pursued by [Oliver et al. \[2022\]](#). The arrangement of depth bins of bathymetry obtained is shown in [Figure 3.6](#). The depth bins do not have a homogeneous width in terms of depth values: they are wider over the slope (depth  $> 200$  m) where the slant is greater; on the contrary, they are narrower over the continental shelf (depth  $< 200$  m). Eventually, for each day and for each depth bin of bathymetry, a surface averaged Chl- $\alpha$  value has been calculated. This procedure was repeated for each year; the results are summarized in [Figure 3.7](#).

The *Hovmöller diagrams* provide a clearer representation of the intra-annual cycles of surface Chl- $\alpha$  concentrations, highlighting both seasonal and semi-seasonal blooms. Every year there were two blooms: the first was during spring with extension all over the shelf and part of the slope and concentration  $\sim 3$  mg/m<sup>3</sup>; the second one occurred between October and December but both intensity and extension were restrained. In between these two blooms, during the summer, the concentration both over the shelf and the slope was minimum ( $\sim 0.5$  mg/m<sup>3</sup>). However, some years were anomalous: in 2003, 2010, 2011, and 2017, there was an intense spring bloom ( $\sim 5$  mg/m<sup>3</sup>) over the whole shelf break and slope area. In contrast, in 2013 and 2014 it was constrained to the shelf region. Similarly, 2018 and 2019 had an unusual scattered fall bloom with the maxima surface concentrations up to  $\sim 5$  mg/m<sup>3</sup> until the 1000 m isobath. Eventually, from this kind of analysis no signal of short-lived enhancements has been found. Consequently, we have examined enhanced days, using individual MODIS Aqua satellite images with more than 50% of data coverage. The results are discussed in the next paragraph.

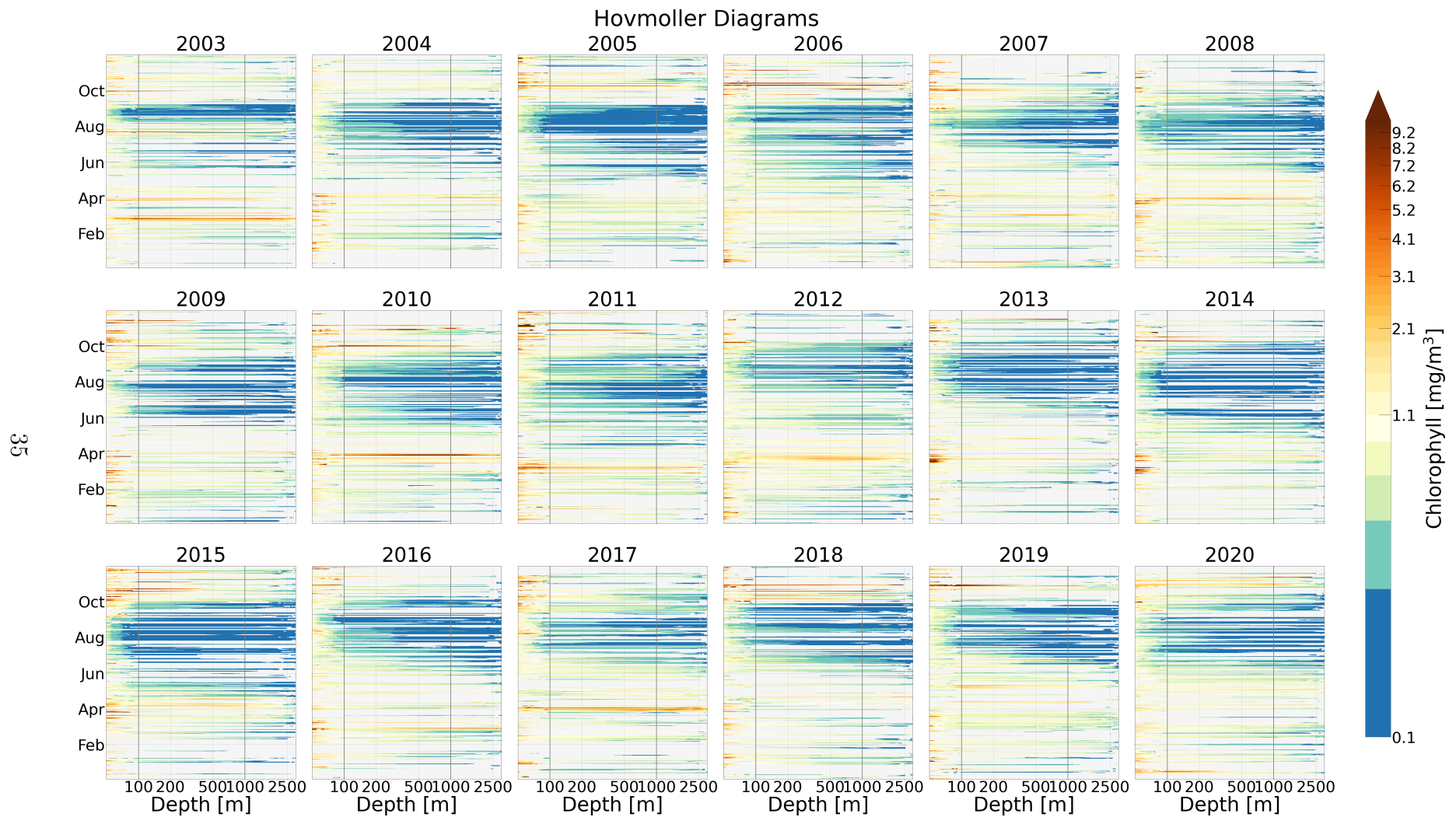


**Figure 3.7:** Depth-binned mean chlorophyll concentrations in the MAB region, from 2003–2020. Note the logarithmic color scale. Light grey regions indicate cloud cover. The 100 m and 1000 m isobaths are identified by the two vertical grey lines.

#### Identification of surface Chl- $\alpha$ enhancements

The satellite median Chl- $\alpha$  concentration for the period of interest demonstrated that shelf break chlorophyll enhancements are typically springtime features (Figure 3.8), confirming the tendency found by [Oliver et al. \[2022\]](#). While median Chl- $\alpha$  concentrations were higher across the shelf break for most of April and May; the period when they were enhanced relative to both the shelf and slope is constrained to only 20 days (24 April–14 May; highlighted region in Figure 3.8). The highest Chl- $\alpha$  concentrations ( $> 1.5 \text{ mg/m}^3$ ) were during the inshore spring bloom beginning in mid-March, which is followed by enhanced chlorophyll at the shelf break and in the slope sea ( $1.1 < \text{Chl-}\alpha < 1.5 \text{ mg/m}^3$ ). On the contrary, the fall bloom was limited to the continental shelf, and the highest concentrations ( $> 1.5 \text{ mg/m}^3$ ) were found within the 75 m isobath. Accordingly, days of enhanced chlorophyll at the shelf break were identified in every year except 2004 (Figure 3.9 (a)). The majority of these ( $> 15$  days per month) happened on April and May (see Figure 3.9 (b)). During fall (October and November) the number of enhancements decreased between 3 to 10 days per month. On the other hand, no significant enhancements were found in winter and late summer (August and September). However, within the period 2003-2020, 66 enhancements were found. The majority of enhanced days had magnitudes between 1 and  $2 \text{ mg/m}^3$  (see Figure 3.10). The 27% (18 enhanced days) had a magnitude less than  $1 \text{ mg/m}^3$  and, of the remaining, only the 16% had a concentration greater than  $2 \text{ mg/m}^3$ . These intense enhancements were mainly between mid-April and May, with some occasional ones in late March. It is worth noting that these results were obtained considering only those days with a cloud coverage of less than 50%, in order to have a sufficient number of pixels to perform the analysis. As depicted in Figure 2.3, only the 20% of the dataset matched this requirement. However, despite the high cloudiness affecting the data (see Section 2.2), results show good agreement with the analysis proposed by [Oliver et al. \[2022\]](#).

#### 3.1.3 Space-time analysis method for Chl- $\alpha$ concentration

The power spectral density (PSD) of the depth-binned (see procedure explained in Section 3.1.2) daily mean surface Chl- $\alpha$  concentration has been estimated, for the whole period 2003-2020, to investigate the variability of the signal and potentially detect any periodicity. To accomplish this, we conducted a space-time analysis applying the *Welch's method* as explained in Section 2.2.1. The resulting two-dimensional spectrum shows the relationship between the temporal and spatial variability and it is presented in Figure 3.11. As expected the highest local maximum corresponds to the seasonal cycle (yearly frequency), and has the greatest magnitude over the shelf, 50 m and 75 m bathymetry. Then it decreases toward a second local maximum over

Climatological Median Chl-a [ $\text{mg}/\text{m}^3$ ]

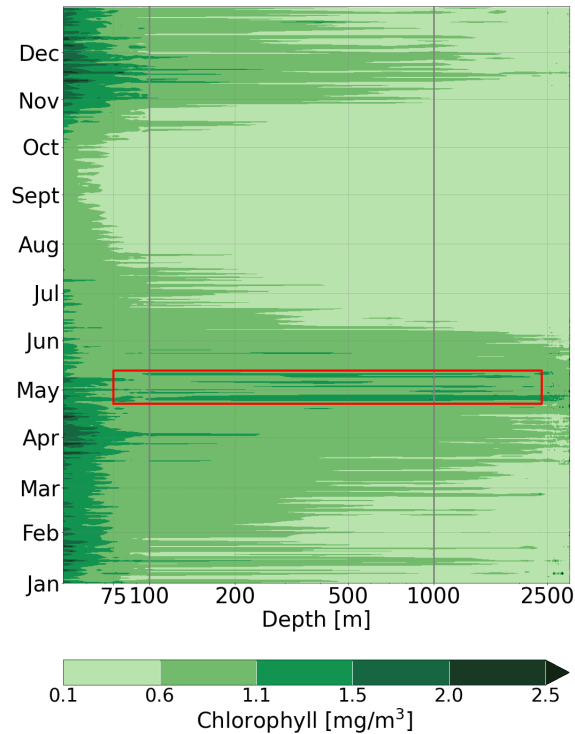


**Figure 3.8:** Depth-binned median chlorophyll concentration in the MAB region. The red box indicates the period of chlorophyll enhancement at the shelf break (24 April–14 May). The 100 and 1000 m isobaths are identified by the two vertical grey lines.

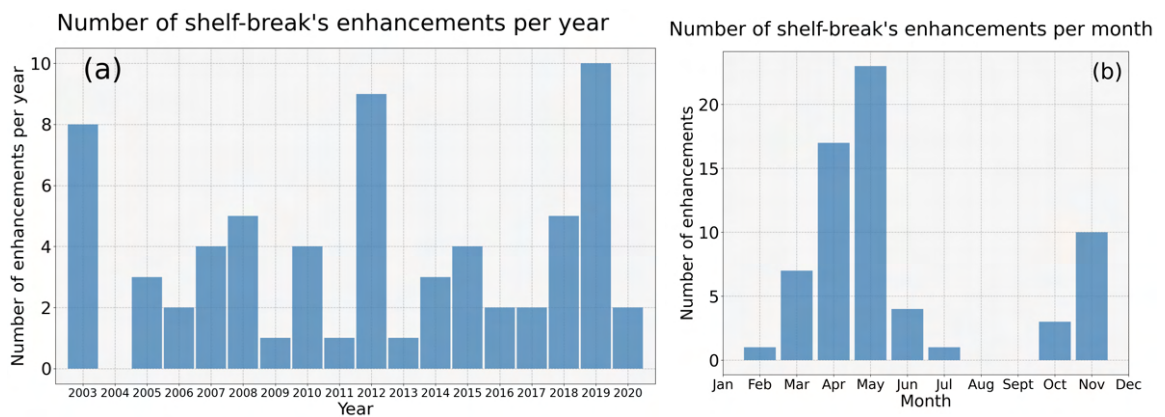


**Figure 3.9:** Panel (a): number of enhanced surface Chl- $\alpha$  days at the shelf break (concentration at the shelf break exceeds that of both the concentration over the shelf and the slope), per year within the period 2003 - 2020. Panel (b) number of enhanced surface Chl- $\alpha$  days at the shelf break, per month within the period 2003 - 2020.

### 3 Characterization of inter-annual chlorophyll- $\alpha$ variability

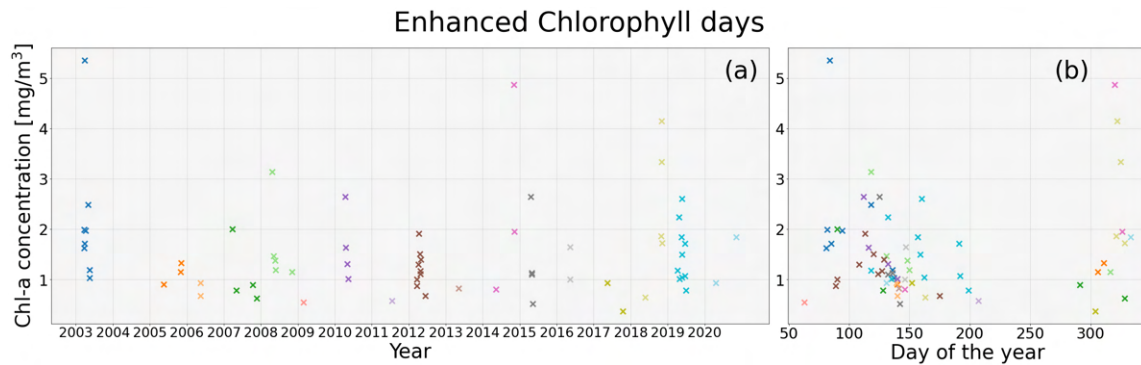


**Figure 3.10:** Distribution of enhanced Chl- $\alpha$  days grouped per year (panel a) and per month (panel b). Different colors are used to distinguish different years.

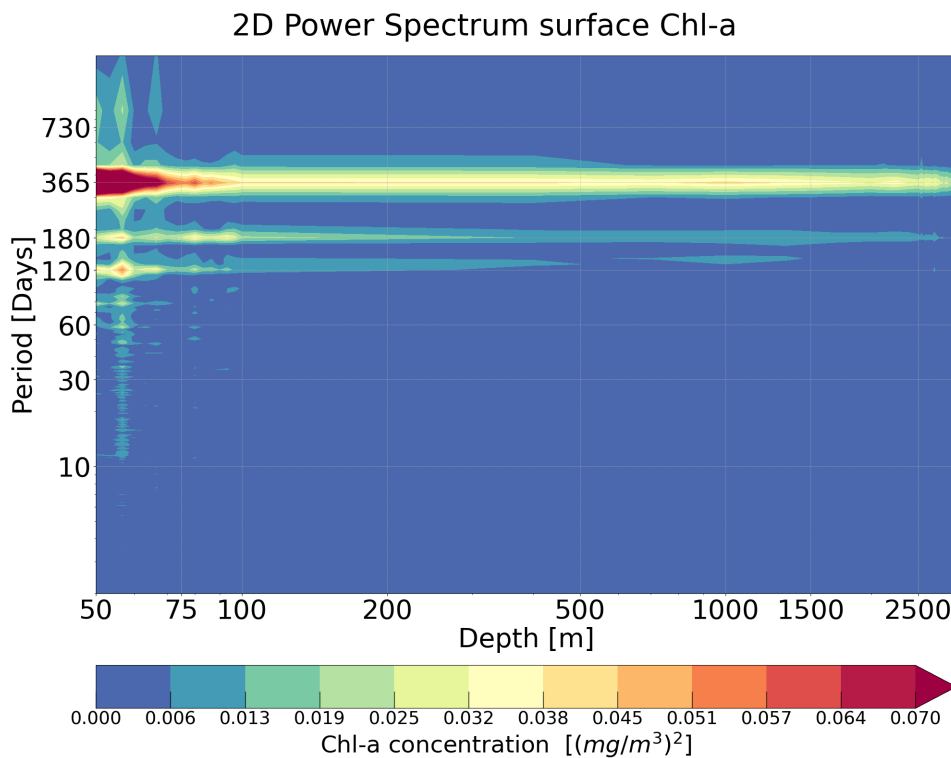


**Figure 3.11:** 2D Welch's power spectrum of depth-binned mean Chl- $\alpha$  concentration in the MAB region. Note the log scale for the x-axis.

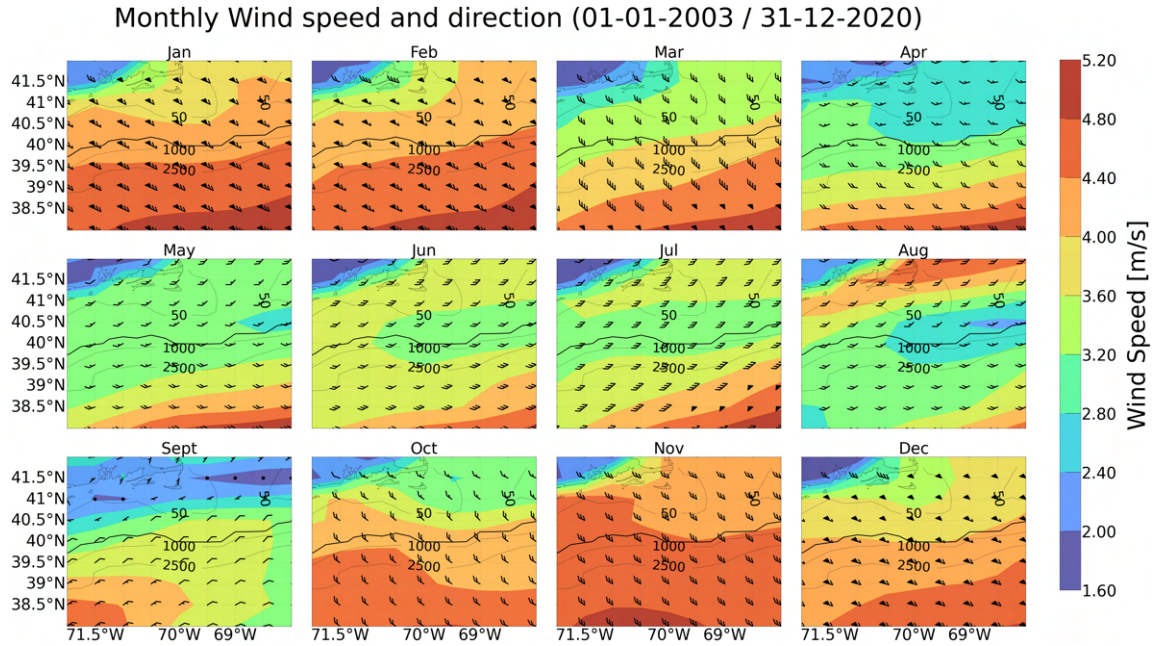


**Figure 3.12:** Monthly mean wind speed and direction (wind barbs). The colors represent the wind intensity. Grey contour levels represent bathymetry; the bold black line represents the shelf break at 200 m isobath.

the outer shelf, close to the 100 m isobath; however, the signal remains significantly high up to the outer slope ( $\sim 1000$  m isobath).

There were two other local on-shore maxima, corresponding to 120 days (intra-seasonal cycle) and 180 days (semi-seasonal cycle). It is interesting to note that the former has a higher magnitude in the shelf area than the one corresponding to the semi-seasonal cycle, but it is limited to the continental shelf, not extending up to the shelf break ( $\sim 100$  m isobath). On the other hand, the one corresponding to a period of 180 days reaches the shelf break region. For periods less than 120 days, no significant periodical frequencies have been found, thus the results of [Oliver et al. \[2022\]](#) have been confirmed also in this analysis: short-lived enhancements are not visible in inter-annual means, thereby confirming their transient behavior.

## 3.2 Environmental conditions

### 3.2.1 Surface Winds

The inter-annual (from 2003 to 2020) monthly mean of wind speed and direction at 10 m height from the surface has been investigated and the results obtained are reported in [Figure 3.12](#)

As expected, the wind intensities are higher during the winter season and lower during the summer. In general, the winds are weaker closer to the coast (mean

### 3 Characterization of inter-annual chlorophyll- $\alpha$ variability

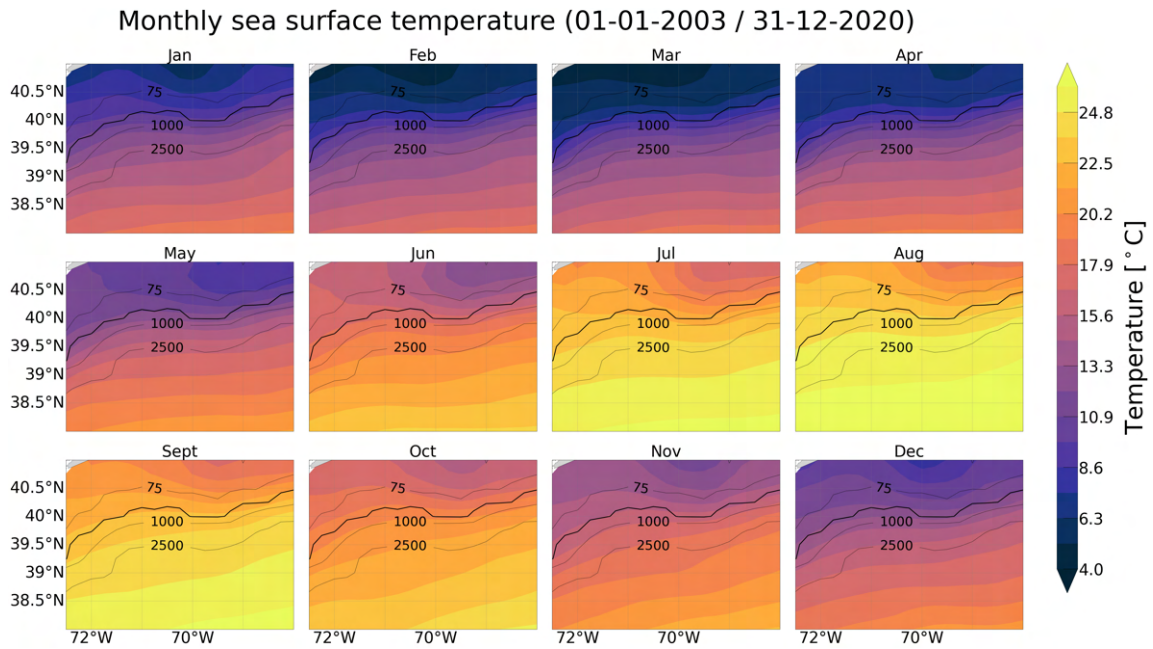


**Figure 3.13:** Monthly mean of sea surface temperature distribution. Grey contour levels represent the bathymetry; the bold black line represents the shelf break at 200 m isobath.

speed  $\sim 2$  m/s) and stronger over the open ocean (up to 5 m/s during winter). It is interesting to note that in June a minimum, with intensity around 3 m/s, arose in the west part of the area and it extended almost all over the shelf break. This minimum seems to enlarge towards the East in July and decreases to 2.5 m/s in August. On the contrary, in August there is a maximum (intensity  $\geq 4$  m/s) in the northwest part, over Cape Cod Bay. Eventually, the direction of the winds is mainly eastward in Spring, northeast in Summer, and southwest during Autumn and Winter. Overall the mean wind direction is perpendicular to the coast, thus supporting the upwelling mechanism due to the displacement of water far away from the coast.

#### 3.2.2 Sea surface temperature, salinity and currents

To characterize the fields of the physical variables in the ocean, it has been analyzed the mean monthly distribution of the surface temperature, salinity, and horizontal velocities, shown in Figures 3.13, 3.14, and 3.15.

The frontal structure at the shelf break was evident in the surface horizontal gradient that separates cold and fresh water over the continental shelf (up to 200 m isobath) from warm and salty water over the slope. The temperature gradient is more evident in February and during the spring season. In summer the surface water homogenizes toward warmer temperature  $\sim 23$  °C, which decreases up to  $\sim 13$  °C during the autumn and winter, restoring the horizontal gradient.

The salinity field shows a stronger horizontal gradient during Summer, with the

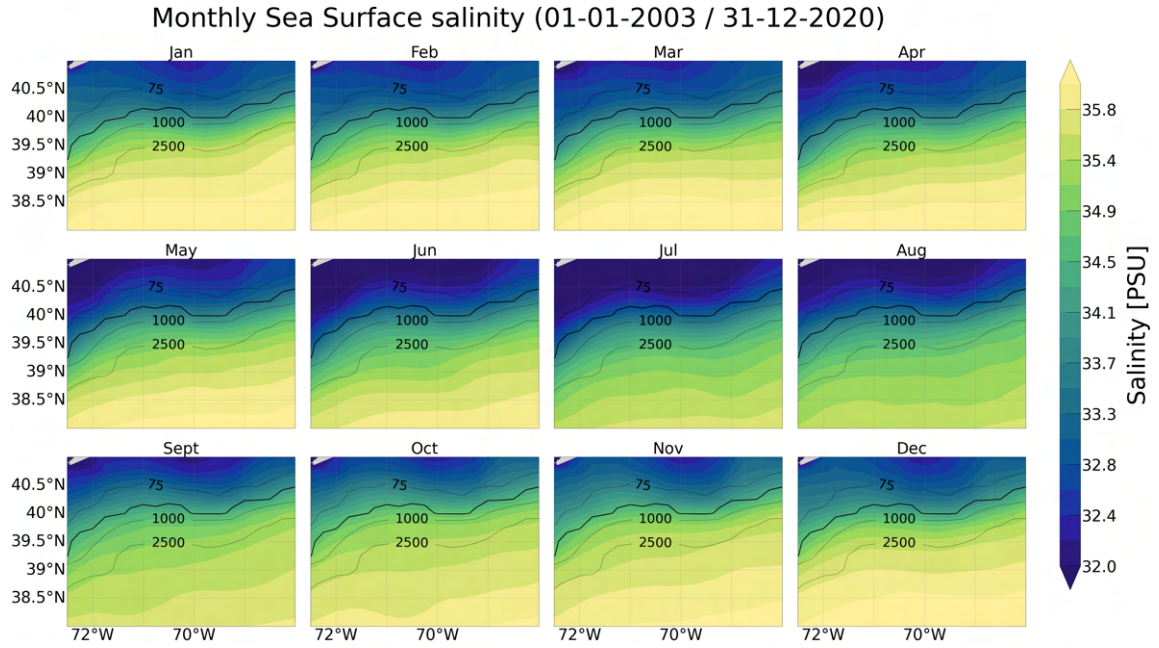


**Figure 3.14:** Monthly mean of sea surface salinity distribution. Grey contour levels represent bathymetry; the bold black line represents the shelf break at 200 m isobath.

lowest values close to the coast (32 PSU). This gradient is always present throughout the year, even if it is less intense during the colder seasons, due to less evaporation ( $\sim 33.5$  PSU on-shore). The surface water salinity over the continental slope area is about 35 PSU.

The sea surface currents in the area are mainly influenced by the presence of the Gulf Stream in the southern part of the domain and by the Shelf Break Jet around  $40^\circ\text{N}$  in latitude, as shown by Figure 1.1. The shelf break Jet is an equatorward flowing jet. It is part of a coastal current system flowing from the Labrador Sea, along the east coast of North America at the edge of the shelf, until it reaches the Gulf Stream at Cape Hatteras (see Figure 1.1, [Forsyth et al., 2020]). It brings fresh and cold water over the shelf, accordingly, it is usually associated with the shelf break front. It has a maximum surface intensity observed in March and a secondary maximum between December and January (see Figure 3.15). The first one is around  $0.17$  m/s, instead, the second one had velocities only reaching  $[0.04 - 0.1]$  m/s. On the contrary, during the summer (from July to September), the free jet of the Gulf Stream had the greatest intrusion over the continental shelf, reaching  $39.8^\circ\text{N}$ , thus the mean flow is predominately eastward. During the months before and after this period, the mean coastal currents rotated to couple with the edge of the Gulf Stream.

### 3 Characterization of inter-annual chlorophyll- $\alpha$ variability

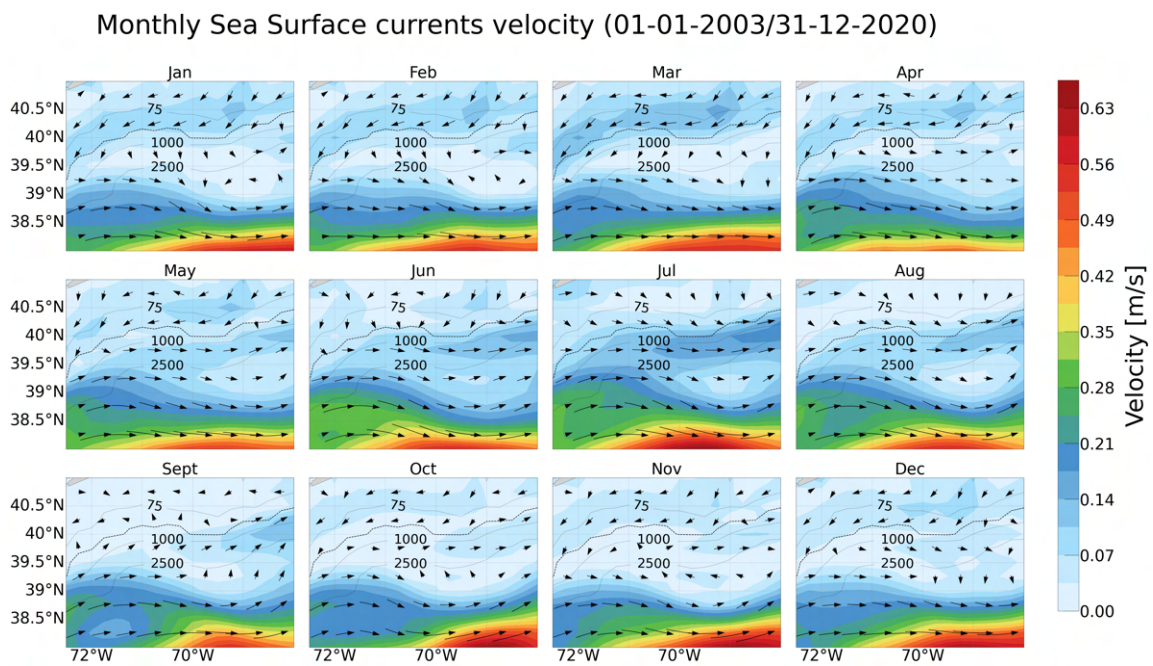


**Figure 3.15:** Monthly mean of sea surface currents distribution. Colors are the intensity calculated as the module of the horizontal velocity vector. Arrows represent surface currents' directions. The gray contour levels represent bathymetry; the bold black line represents the shelf break at 200 m isobath.

# Chapter 4

## Physical drivers for chlorophyll- $\alpha$ variability

Surface and subsurface enhancements of Chl- $\alpha$  at the MAB shelf break have been observed in synoptic *in situ* data and satellite measurements. However, the concentration levels are not always enhanced at the shelf break and they are subject to the influences of frontal instability and external forcing (e.g., wind, warm core ring, streamers) [Zhang et al., 2013]. In the following sections an attempt to explain two of the many possible driving mechanisms that may increase primary productivity has been done. In Section 4.1 the role of the Ekman transport has been studied to explain seasonal and intra-seasonal shelf break blooms. Conversely, in Section 4.2, it has been tested the hypothesis if nutrient transport induced by BBL detachment within the frontal surface can lead to a biological response.

### 4.1 Relation between wind transport and enhanced surface Chl- $\alpha$

Ekman restratification has been suggested as a possible driving mechanism [Oliver et al., 2022] for short-lived Chl- $\alpha$  enhancements in the MAB shelf break front region. This is triggered by wind forcing that opposes the surface current associated with the front, increasing the surface stratification resulting from the advection of less dense shelf water over denser slope water. Accordingly, the main role in this process is associated with westerly winds. However, these enhancements are a transient feature characterizing the Chl- $\alpha$  concentration at the MAB, in fact, they are not observed in inter-annual averaged trends (see Section 3.1.2). It has been observed that over the 18 years studied, the mean direction of the winds over the region is mainly eastward (see Chapter 3.2.1), consequently upwelling mechanisms due to the

## 4 Physical drivers for chlorophyll- $\alpha$ variability

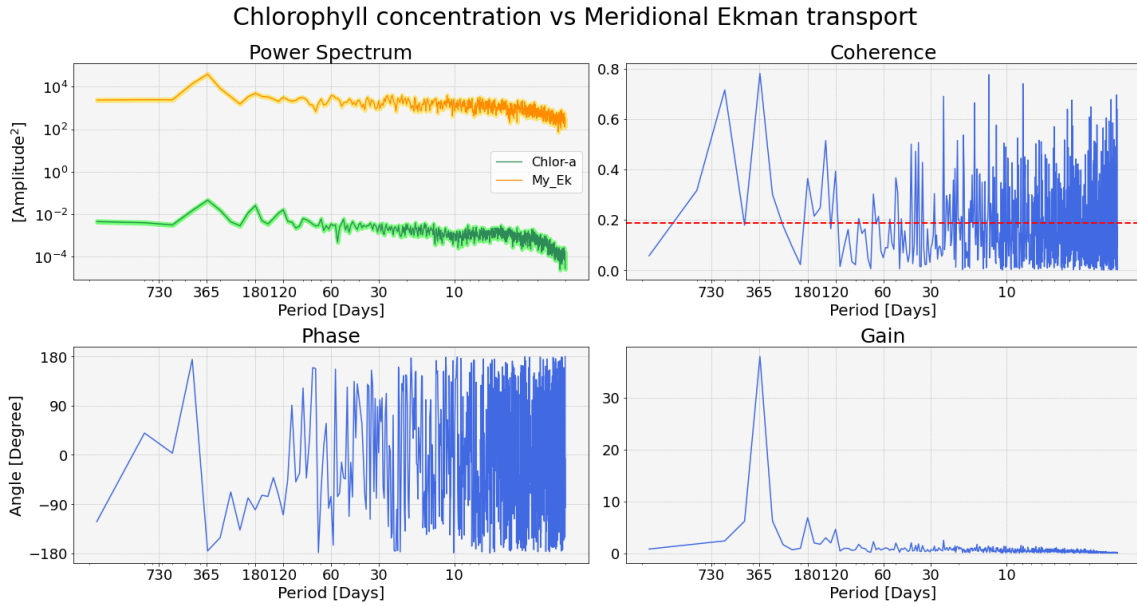


**Figure 4.1:** Coherence analysis between averaged surface Chl- $\alpha$  concentration and meridional Ekman transport calculated for the MAB region, within the period 2003-2020. Note the log scale on the y-axis. The light-green and yellow shadows in Welch’s PSD represent the confidence intervals. The red line associated with the coherence is the lower boundary for statistical significance.

displacement of the water far from the coast should be supported. To determine if there is any significant correlation between the mean surface Chl- $\alpha$  concentration and the meridional Ekman transport (it is the component of the transport associated with the westerlies), a *coherence analysis* between the two signals, limited to the area of the shelf break (between 75 m to 1000 m bathymetry) has been performed. The meridional Ekman transport and the associated upwelling index have been calculated as reported in Chapter 2.3.

The main oscillation frequencies associated with the Chl- $\alpha$  variability have a period of 120, 180, and 365 days, which confirm, respectively, the intra-seasonal, semi-seasonal, and seasonal cycles individuated from the long-term variability analysis (Figure 4.1). It is worth noting that, the same peaks correspond to local maxima of the Welch’s PSD of the meridional Ekman transport, even if they are not so self-evident, except for the one associated with the season cycle. Accordingly, in the 18-year period studied, the intensification of westerly winds leads to a significant response in the surface Chl- $\alpha$ , in fact, both gain and coherence’s local maxima were found associated with the same periods of PSD’s maxima, above the significance threshold. It is interesting to note that a significant phase shift, ranging between  $-90^\circ$  and  $-180^\circ$ , is observed between the Chl- $\alpha$  concentration and the meridional Ekman transport for either intra-seasonal, semi-seasonal, and seasonal frequencies. Specifically, in the case of the intra-seasonal and semi-seasonal cycles, a phase opposition is evident, with a

lag of approximately 6 hours<sup>1</sup>. Furthermore, for the seasonal variability, this phase opposition is prolonged to approximately 12 hours. Possibly, the driving mechanism for the former cycles could be the Ekman restratification as suggested by [Oliver et al. \[2022\]](#). If the winds are strong enough to locally increase the density gradient close to the front surface outcrop, but not so strong to deepen the mixed layer depth, then nutrients can accumulate and increase primary production. This mechanism on an inter-annual scale could be more likely during the spring and summer seasons when at the surface there is a positive heat flux that increases the surface stratification. On the contrary, in fall and winter, there is cooling and negative buoyancy forcing in contrast to spring and summer. The cooling would increase the mixed layer depth in these seasons, supplying the surface layer with nutrients from greater depths. Moreover, westerlies intensified from autumn toward the winter season, increasing the surface mixing, which can also replete the nutrients at the surface. Thus, the processes are different depending on the season but they are captured by the same signal variability.

Eventually, no significant periodic signal was found for a period within 100 and 60 days (see [Figure 4.2](#)). Nevertheless, relevant correlations can be distinguished for around monthly and from 10- to 7-day periods, even if these are weaker when compared to long-term variability. It is interesting to note that, the phase lag is coherent with the one found for semi-seasonal and seasonal frequencies. To conclude, the Ekman dynamic can explain up to the intra-seasonal variations of the surface Chl- $\alpha$ , but in general, is not a strong hypothesis to explain short-lived enhancement events.

To further investigate this latter aspect, the surface wind forcing can be quantified using an *Upwelling Index*  $UI = \tau_x / \rho_o f$ , (i.e., the off-shore component of the surface Ekman transport, [[Li et al., 2020](#)]). Positive (negative) UI represents upwelling (downwelling) favorable wind conditions, respectively. For each of the enhanced days for Chl- $\alpha$  concentration found within the analysis reported in [Chapter 3.1.2](#), it has been calculated the mean UI at the shelf break. Of all 66 enhanced days, only the 72% had a positive value for the UI, the remnants were negative. Thus, no significant correlation has been found between Ekman's upwelling estimation and the identified enhanced days. This result confirms that the magnitude of the enhancement is not sufficient to rise above the variability, which is large in this region [[Zhang et al., 2013](#)]. Furthermore, it has been verified that the Ekman upwelling dynamics is not on average correlated with the enhanced surface chlorophyll, in particular for short-term

---

<sup>1</sup>If referred to the rotation of the Earth, it takes approximately 360 degrees to complete a full rotation in 24 hours. Then to calculate the time it takes to rotate 90 degrees, it is straightforward:  $90 * \frac{24}{360}$

## 4 Physical drivers for chlorophyll- $\alpha$ variability

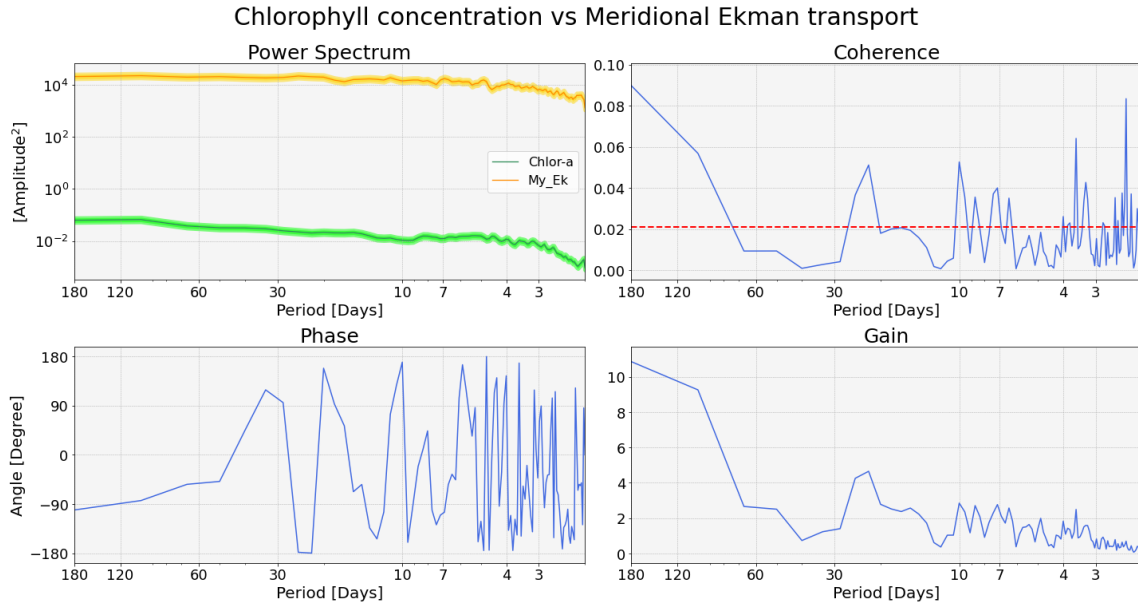


**Figure 4.2:** Coherence analysis between averaged surface Chl- $\alpha$  concentration and meridional Ekman transport calculated for the MAB region, within the period 2003-2020, highlighting the semi-seasonal variability (periods less than 180 days). Note the log scale on the y-axis. The light-green and yellow shadows in Welch’s PSD represent the confidence intervals. The red line associated with the coherence is the lower boundary for statistical significance.

events, suggesting that: there are more complex processes regulating the variability, the magnitude of the Ekman upwelling is not significant enough or the sample data is not adequately representative. It must be pointed out that the results are strongly affected by the high cloudiness of the images (see Chapter 2.2), thus more enhanced days could be identified within the same period and a more robust statistic could be built. Nevertheless, even if no significant chlorophyll enhancement at the shelf break was found in the inter-annual variability, this is not incompatible with prior studies that document elevated chlorophyll in synoptic observations ([Marra et al., 1990], [Oliver et al., 2022], [Hirzel et al., 2023]).

### 4.2 Nutrient transport induced by bottom boundary layer detachment

For synoptic observation, the hypothesis of nutrient transport induced by BBL detachment has been investigated using the two methods described in Chapter 2.1: accumulated properties change and along isopycnals changes in nitrate, chlorophyll, and PON concentrations. The analysis has been performed using the hydrographic and nutrient sections collected during the three SPIROPA oceanographic cruises. All the sections presented are North-South transects (cross-shelf) along the 70.8°W, in the northern section of the MAB: from south Cape Cod to Nantucket Shoals,

Massachusetts.

### 4.2.1 CTD and Niskin bottles sections

The hydrographic variables (temperature (T), salinity (S), potential density ( $\sigma_\theta$ )), Chl- $\alpha$ , collected from shipboard CTD, have been interpolated over a regular two-dimensional grid: 7 km in  $y$  (cross-shelf direction) and 1 m in  $z$  (vertical direction). Instead, for nutrients (nitrate, PON, phosphate, silicate) profiles collected using Niskin bottles rosette was used a 2D regular grid with a resolution of 7 km in  $y$  and 10 m in  $z$ . The horizontal resolution corresponds to the station spacing; the vertical resolution depends on the instrument. In this way, completed transects have been produced, shown in Figures 4.3, 4.4 and 4.5

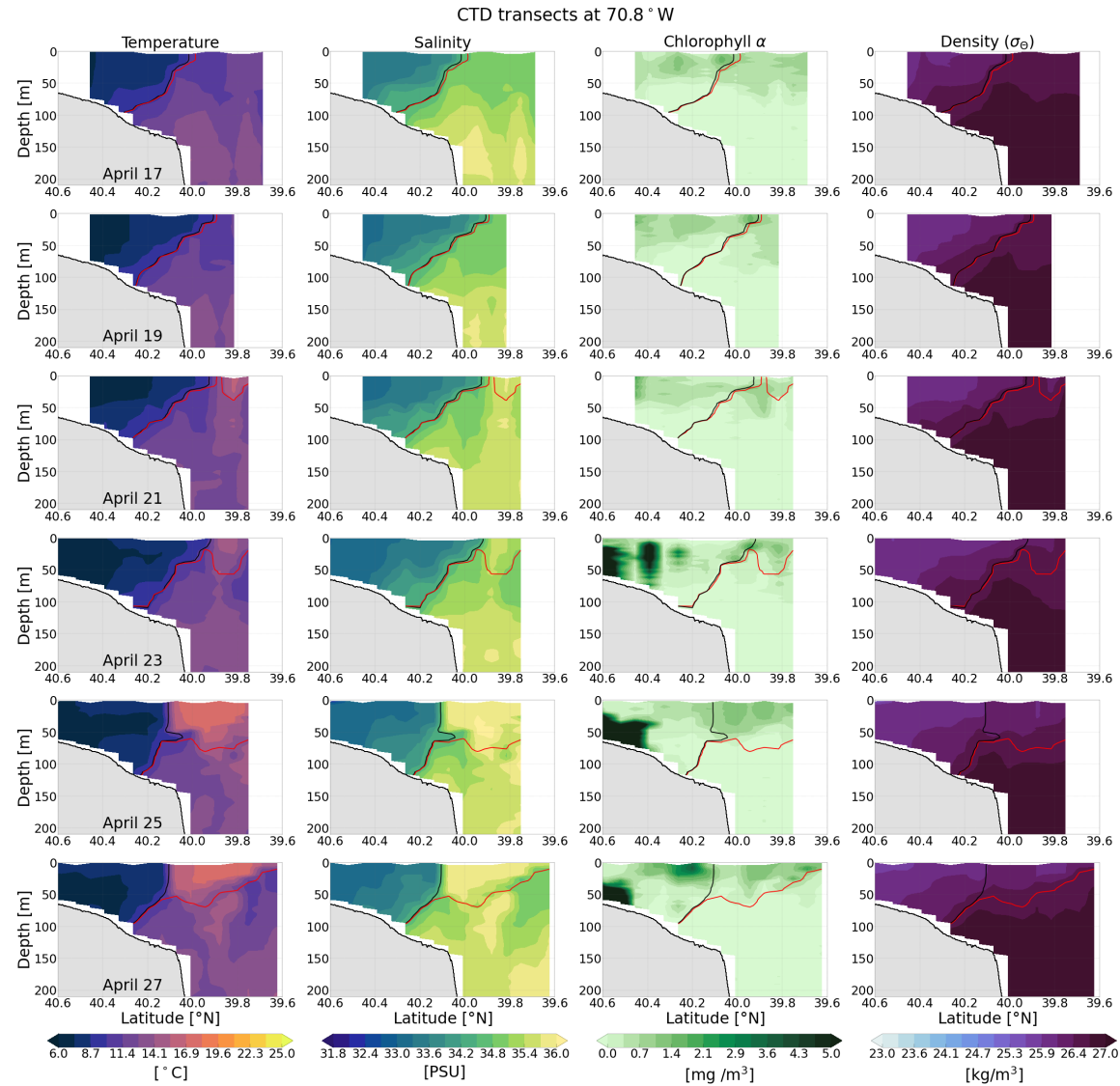
#### Frontal variability

The characteristic feature of the MAB shelf break region is the shelf break front which appears as a sharp transition from cooler, fresher shelf waters to warmer, saltier slope waters, with the isopycnals ( $\sigma$ ) sloping upward and off-shore. The slope of the isopycnals is in the opposite direction of the slope of the bathymetry [Gawarkiewicz et al., 2018]. From the literature, it can be found that the current identification for the mean location of the front corresponds with the position of the 34.5 isohaline [Houghton et al., 1988]. As explained in Chapter 1.1, the presence of both the topographic shelf break and the horizontal density gradient makes the front “trapped” at the shelf break even if its structure can be strongly affected by the seasonal stratification and off-shore forcing interactions.

April 2018 had the weakest stratification of the three cruises making the front steep with both isohalines and isopycnals outcropping at the surface and each other parallel. In contrast, July 2019 showed the greatest vertical stratification due to the formation of the thermocline; the front was shallower and the isopycnals were no longer outcropping the surface but bending below the shallower mixed layer. As much as the isopycnals flatten, as much the exchange of water between the two sides of the front is favored, thus explaining the intrusion of intermediate salty water into deeper and saltier ones.

May 2019 had increased vertical stratification compared to April 2018.

Different vertical stratification conditions were also reflected in the detection of the isopycnal at the center of the front (the one intersecting the foot of the front in the BBL, as defined by  $S = 34.5$  PSU): lighter from spring to summer. In particular, it has been found that for April was 26.6  $\sigma$ , for May 26.45  $\sigma$ , and 26.3  $\sigma$  for July. These results agree with the climatology proposed by Gawarkiewicz et al. [2018], except for April which was outside the range of variability [25.8 - 26.45] kg/m<sup>3</sup>. In general, the



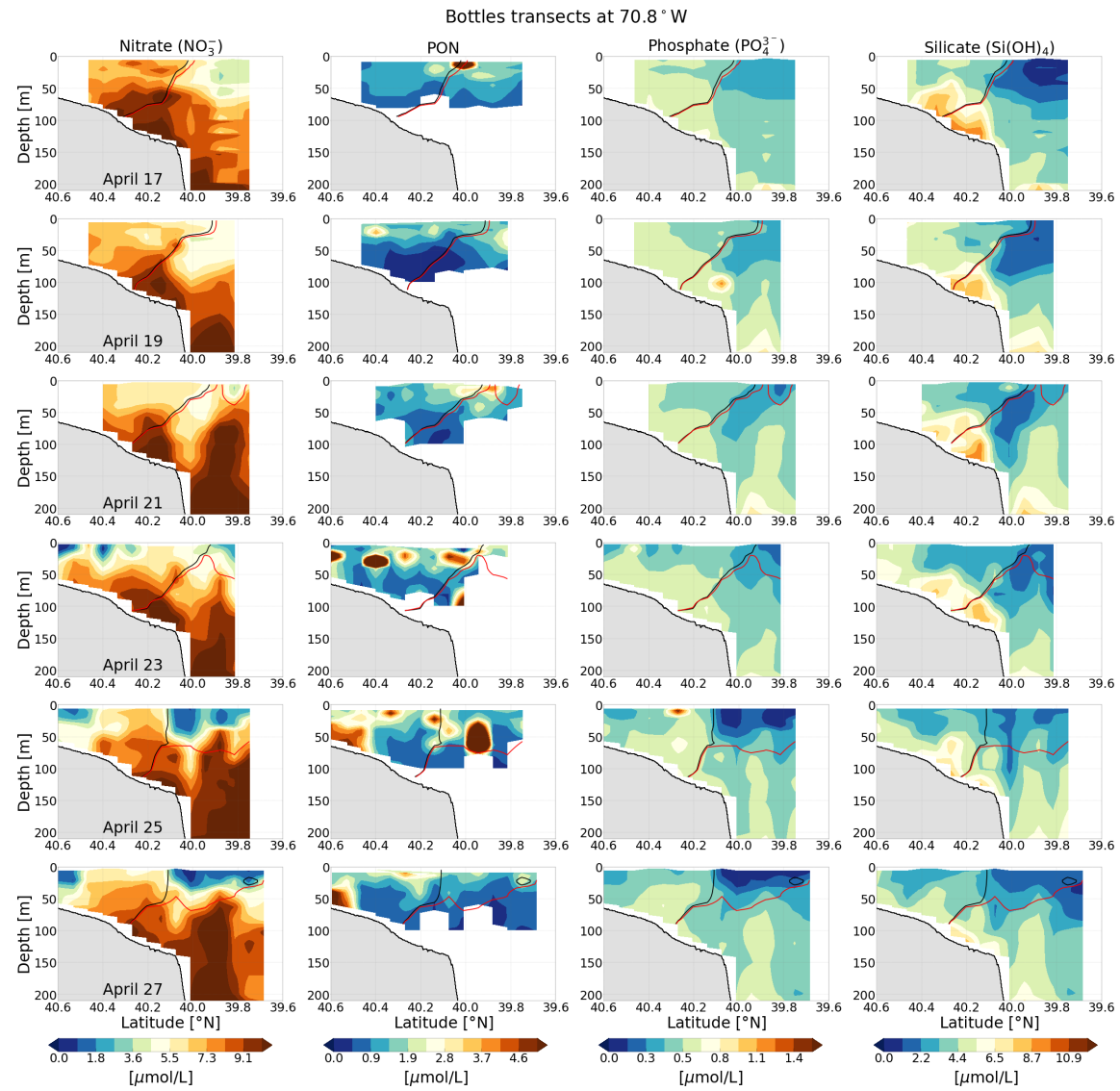
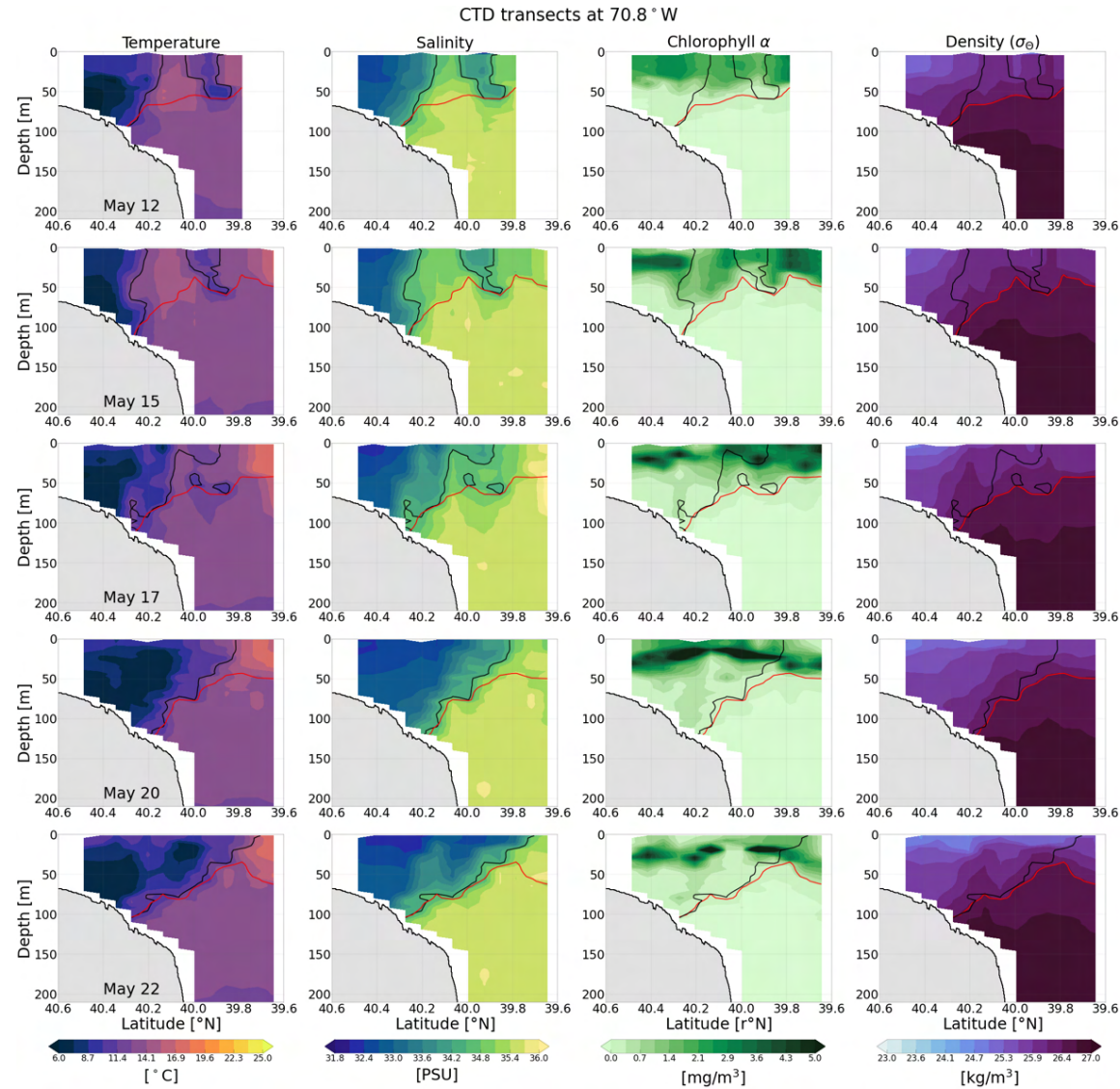


Figure 4.3: Continued from the previous page.



**Figure 4.4:** All useful transects for May 2019. The black line represents the mean location of the MAB shelf break front (34.5 isohaline). The red line represents the isopycnal intersecting the foot of the front in the bottom boundary layer (26.45  $\sigma$ ). Even page panel: CTD sections, Odd page panel: bottles sampled data sections.

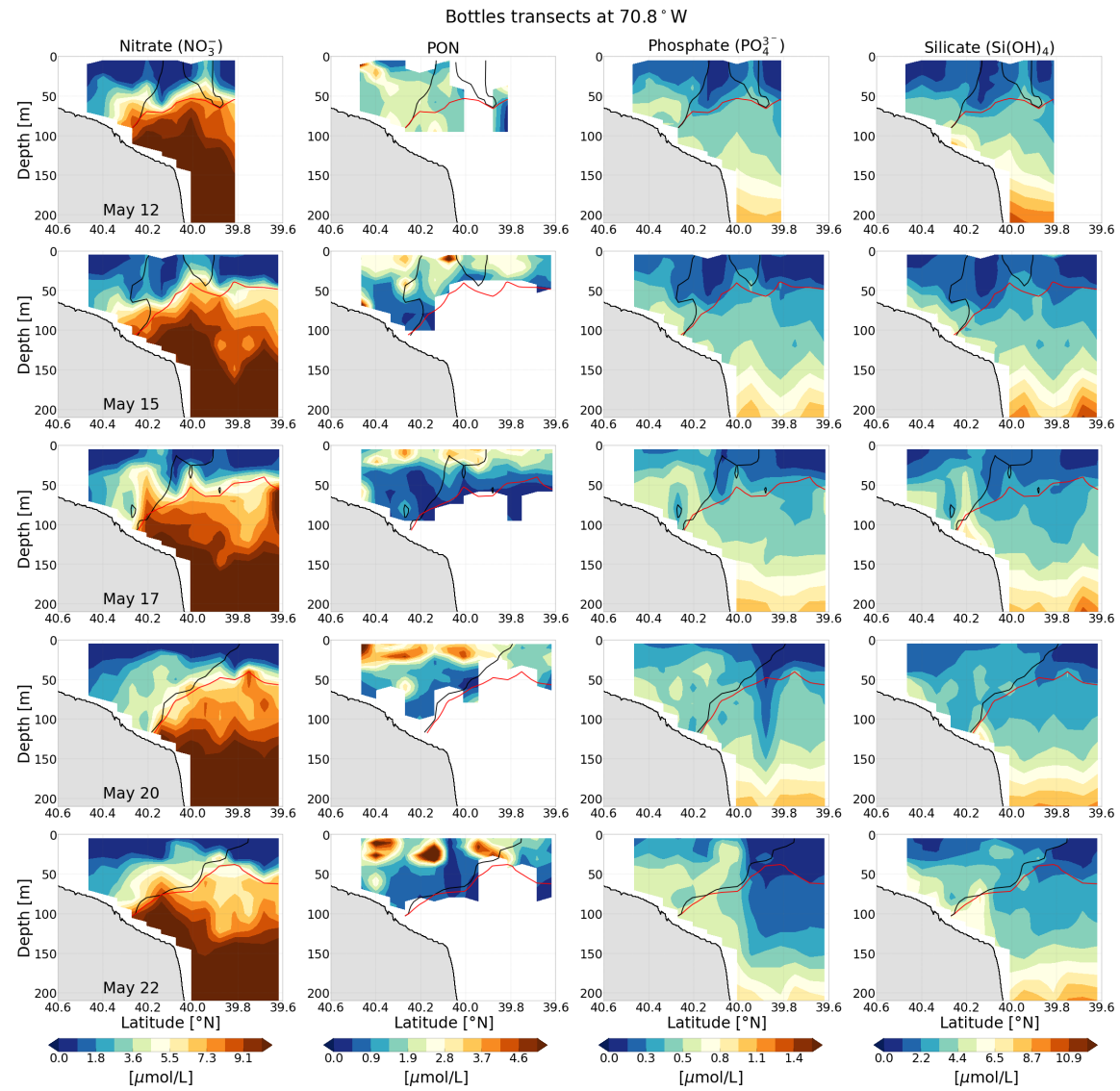
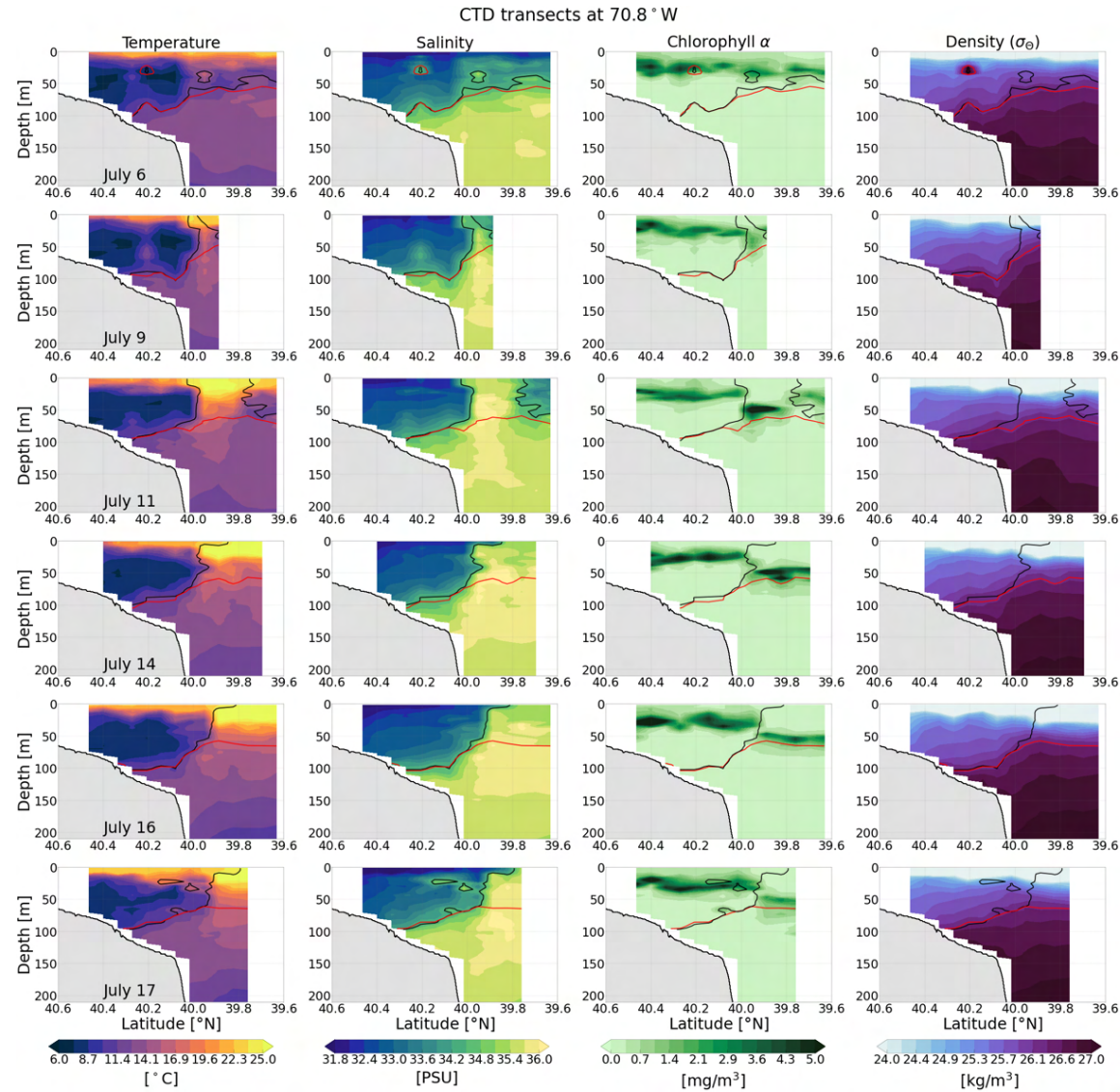


Figure 4.4: Continued from the previous page.



**Figure 4.5:** All useful transects for July 2019. The black line represents the mean location of the MAB shelf break front (34.5 isohaline). The red line represents the isopycnal intersecting the foot of the front in the bottom boundary layer (26.3  $\sigma$ ). Even page panel: CTD sections, Odd page panel: bottles sampled data sections.

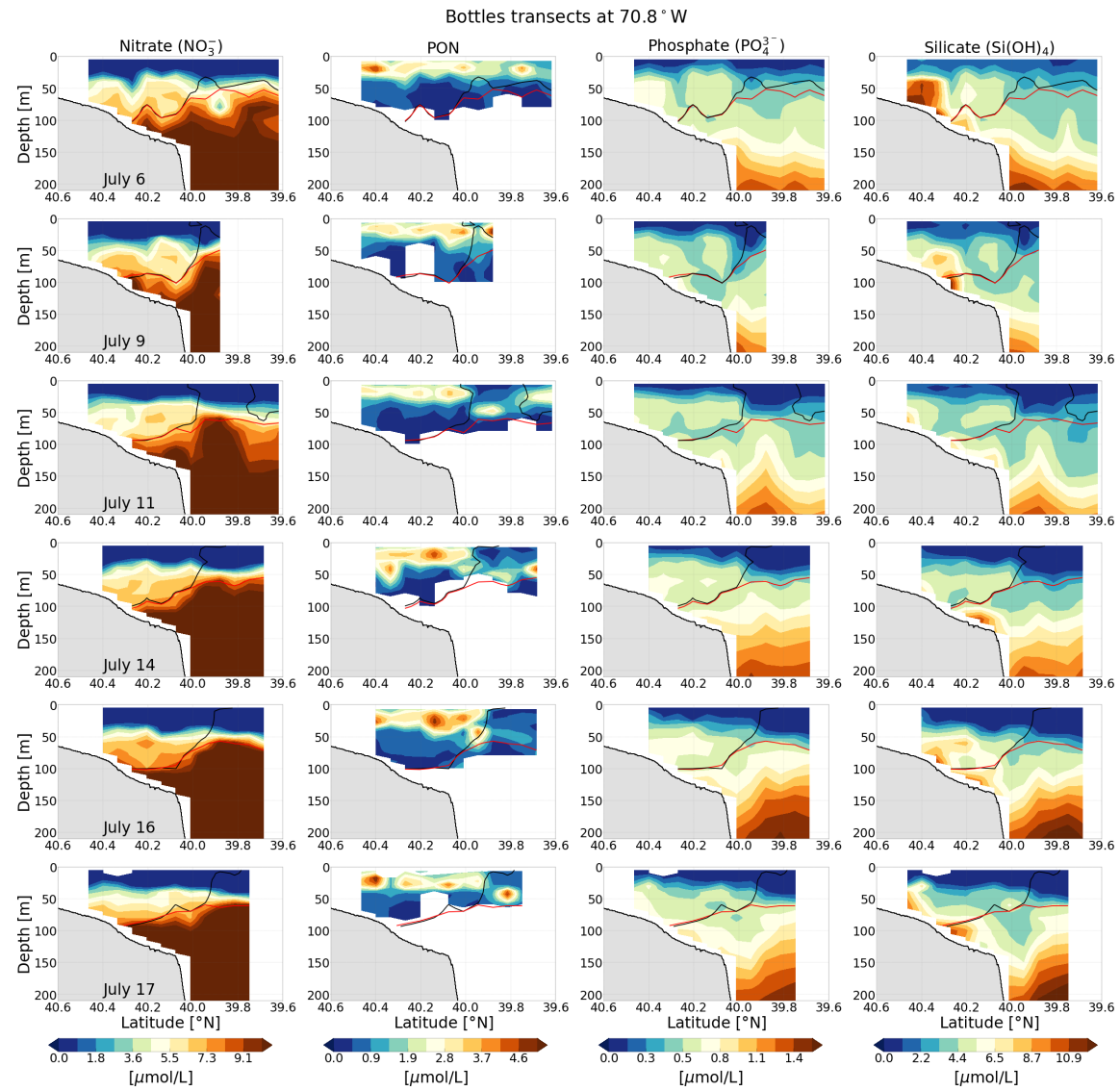


Figure 4.5: Continued from the previous page.

#### 4 Physical drivers for chlorophyll- $\alpha$ variability

---

front is denser and steeper during spring; less dense and wider through summer.

During all the cruises there were some significant influences due to off-shore structures impinging on the continental shelf. In particular, in the last days of April 2018 the peak values of both salinity and temperature in the surface layer, corresponding to the cross-shelf motion of the front head, resulted from the influence of a Gulf Stream warm-core ring [Hirzel et al., 2023]. In May there was the interaction, during all the days analyzed, with frontal eddies that pushed the head of the front significantly on-shore. Thus, making the surface almost vertical and inhibits exchange between shelf and slope water. That condition was relieved during the last day of the cruise when the frontal surface became flatter. The details of this exchange between shelf water and frontal eddies waters can be found in Hirzel et al. [2023].

July 2019 had the highest salinity variability and the greatest change of the frontal surface among the three cruises. In particular, from the third day, a peak in the temperature and salinity fields was visible at the off-shore edge of the front in the upper 50 m which was not present in the first two days. The reduced vertical stratification was related to the crossing on the continental shelf of a streamer associated with a Gulf Stream warm-core ring [Zhang et al., 2023]. The streamer was causing the off-shore advection of the shelf water, thus maintaining the same physical properties in the upper 50 m for all the transect. After the streamer passed, the shelf break front was restored.

#### Chlorophyll and nutrient variability

The distributions of nutrients and chlorophyll reflected the seasonal and submesoscale variability that affected the region. Specifically, in April 2018 nitrate, phosphate, and silicate were all relatively abundant throughout the water column, in particular nitrate and silicate were abundant around the foot of the front. Nutrients were well in excess of the limiting surface concentration of all cruises due to the deep mixed layer depth. They were not surface depleted (concentration  $< 0.1 \mu\text{mol/L}$ ) except in the inshore region around  $40.3^\circ\text{N}$  above the local maxima of chlorophyll ( $> 20 \text{ mg/m}^3$ ). This patch originated from a regional bloom of *P. pouchetii*, with a bulk of this bloom advecting into our transect from its origin on Nantucket Shoals [Hirzel et al., 2023]. The *P. pouchetii* bloom signal was also present in the patchiness of particulate organic nitrate (PON). PON includes both nitrogen contained in living material and nitrogen detritus. Unfortunately, there is no way to distinguish between the two components from these data, thus PON will be used as an order of magnitude estimation for biological particles only. Is worth noting that, the local maximum of PON on April 17th is associated with Ekman restratification, which has been indicated as a driving mechanism for surface chlorophyll enhancements [Oliver et al.,

## 4.2 Nutrient transport induced by bottom boundary layer detachment

---

2022]. In this situation, Ekman restratification has been triggered by strong eastward winds driving the movement of the front off-shore and increasing the vertical density stratification close to the surface. As isopycnals flattened, they created a shallow well-lit mixed layer that was able to support rapid phytoplankton accumulation in nutrient-repleted conditions. As demonstrated by Oliver et al. [2022], the surface chlorophyll was enhanced by the former mechanisms ( $\sim 1.5 \text{ mg/m}^3$ ), which was persistent until the April 23rd after which the concentration was influenced by the intrusion of slope-water onto the shelf, as observed by the flattening of the isopycnals with increased surface stratification.

In May 2019 the growing vertical stratification increased the surface nutrient depletion to around 25 m depth. However, due to mixing associated with strong frontal eddy interactions, all the nutrients showed great patchiness and surface chlorophyll was enhanced up to  $\sim 3.0 \text{ mg/m}^3$ .

In July 2019, nutrients were all depleted at the surface, in particular, nitrate was fully depleted above 30 m depth. Therefore, the chlorophyll maxima were located below the warm surface mixed layer. As soon as the streamer passed and the frontal structure was fully restored, in the off-shore end of the front, both the warmer surface layer and the euphotic zone extended deeper, resulting in a deeper chlorophyll maximum and a deeper nutrient depletion. Eventually, the highest PON concentrations were found matching the chlorophyll maxima patches.

### Water mass characterization

To fully characterize and understand the seasonal variability of the region, temperature (T) vs salinity (S) plots have been analyzed with particular interest to the relation with nitrate concentration. These are shown in Figures 4.6, 4.7 and 4.8.

Nitrate is considered the main limiting factor, in terms of nutrients, to phytoplankton growth in this region. The other important limitation is light but mainly during autumn, winter, and spring seasons, thus those data can not be considered as one strongly contributing to the observed variation in the chlorophyll distributions, except for April 2018.

From historical analysis of the MAB T-S variability [Wright and Parker, 1976], it has been conventional to refer as *shelf waters* to those with salinity less than 34 PSU; *frontal water* when salinity is between 34 and 35 PSU and *slope water* if salinity is greater than 35 PSU. Nowadays the former threshold has been shifted toward 35.8 PSU due to more presence over the upper continental slope of waters originating in the Gulf Stream, which contributes to continental shelf warming [Gawarkiewicz et al., 2018]. The density values associated with shelf and slope water masses were,

## 4 Physical drivers for chlorophyll- $\alpha$ variability

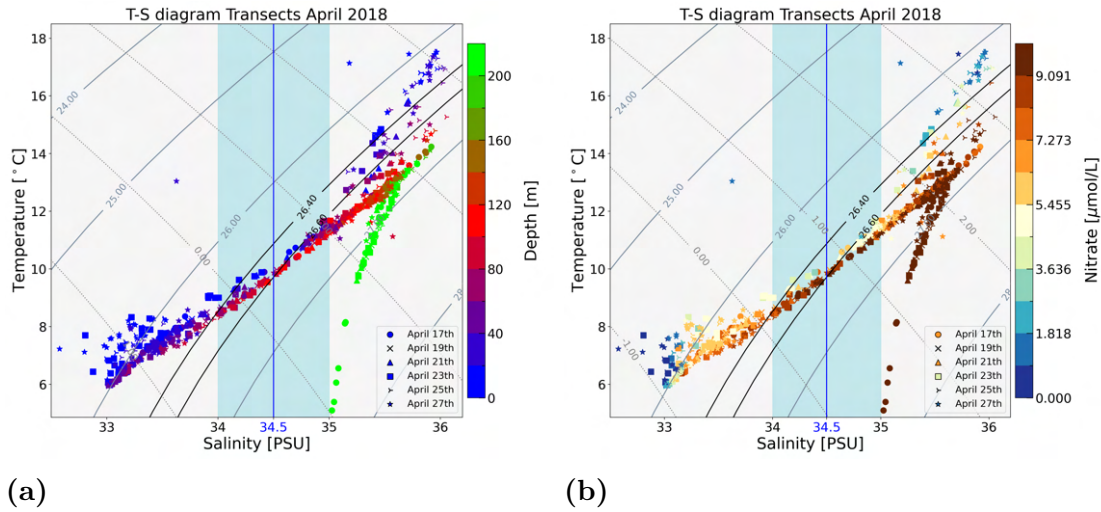


**Figure 4.6:** Temperature vs salinity diagram for all the transects from the April 2018 cruise. Panel (a): colormap represents depth; panel (b): colormap represents nitrate concentration. The light-blue area represents the isohalines corresponding to the frontal water mass. Salinity  $< 34$  PSU represent *shelf waters*,  $S > 35$  PSU correspond to *slope water*. The blue vertical line emphasizes the mean frontal position. The grey solid lines represent density contours [ $\text{kg}/\text{m}^3$ ]; grey dotted lines represent spiciness [ $\text{kg}/\text{m}^3$ ]

respectively,  $25.5 \sigma$  and around  $26.6 \sigma$  and the juncture between those two water masses was occurring for depths between 100 and 120 m. This was called by [Linder and Gawarkiewicz \[1998\]](#) the *upper water thermostad*: a homogeneous layer of waters in terms of temperature. It corresponds to a relative minimum of the vertical temperature gradient. However, these thresholds need to be reviewed considering the ongoing warming of the continental shelf due to climate change. The upper water thermostad can be identified where the vibrant red data points encounter the greenish one, close to the vibrant green data points (Figure 4.7 (a)). From all three cruises, the salinity corresponding to that juncture was increased up to 35.8 PSU, thus confirming the fact that the upper shelf is becoming warmer and saltier due to the supply of water originating in the Gulf Stream that more often reaches the shelf. Possibly also the identification of the mean location of the front should be reviewed, but more climatological investigation needs to be done and three cruises data are not sufficient for this purpose. Therefore in this analysis, the mean position of the front is still identified with the 34.5 isohaline.

The temperatures associated with the upper water thermostad were between  $12^\circ\text{C}$  and  $14^\circ\text{C}$ , up to  $2^\circ\text{C}$  more than the values found by [Wright and Parker \[1976\]](#). By a consequence, it is expected that also the isopycnals related to the bottom boundary layer detachment will be influenced by recent changes.

The distribution of the data on T-S diagrams reflects the vertical stratification conditions: the more the data are scattered, the greater is the vertical stratification.

## 4.2 Nutrient transport induced by bottom boundary layer detachment

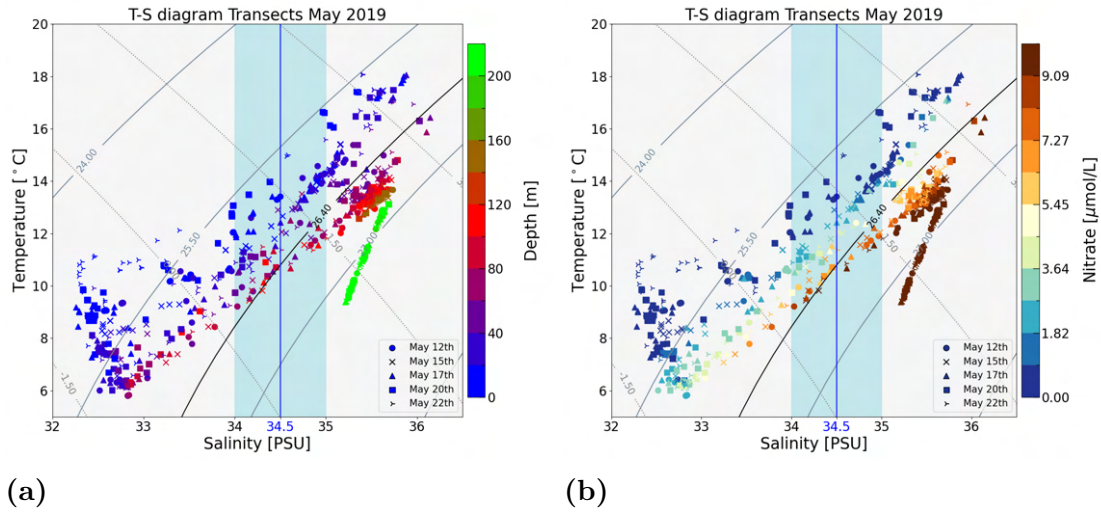


**Figure 4.7:** Temperature vs salinity diagram for all the transects from the May 2019 cruise. Panel (a): colormap represents depth; panel (b): colormap represents nitrate concentration. The light-blue area represents the isohalines corresponding to the frontal water mass. Salinity  $< 34$  PSU represents *shelf waters*,  $S > 35$  PSU corresponds to *slope water*. The blue vertical line emphasizes the mean frontal position. The grey solid lines represent density contours [ $\text{kg}/\text{m}^3$ ]; grey dotted lines represent spiciness [ $\text{kg}/\text{m}^3$ ].

The scattering of the data increases from April to July, as expected.

Another important feature for the region is the *cold pool* (CP): a body of cold bottom-trapped water remnant of winter water maintained by northerly fresh currents, that is always found on the mid to outer continental shelf. It is commonly identified with bottom-water (depth between 40-60 m) having salinity in between 32 and 33 PSU. The CP is an important element in the population dynamics of lower and upper trophic level organisms living on the MAB [Brown et al., 2023]. In Figure 4.6, the CP is present but not capped off by surface stratification as in the other seasons due to the presence of strong mixing, but as soon as the surface stratification increased and temperature-induced stratification created the CP with minimum temperatures ( $\sim 6$  °C) dependent on the severity of the previous winter’s local cooling [Brown et al., 2023]. For the time period studied, the CP was forming during April, on the innermost part of the shelf. In May, it was affected by the same frontal variability due to the strong interaction with frontal eddies. Eventually, in July, the pool was warmed up ( $\sim 7.5$ °C) by turbulent processes acting on its surface.

Another important variable to look at is the spiciness ( $\tau$ ), it represents the spatial variation in temperature and salinity whose effects on density cancel each other. Thus warmer but saltier water (“spicy”) can have the same density as colder but fresher water (“minty”). Spiciness is useful to characterize water mass properties changes. The highest values for spiciness were, as expected, for the water mass associated with the off-shore source water (the warmest and saltiest) corresponding

## 4 Physical drivers for chlorophyll- $\alpha$ variability

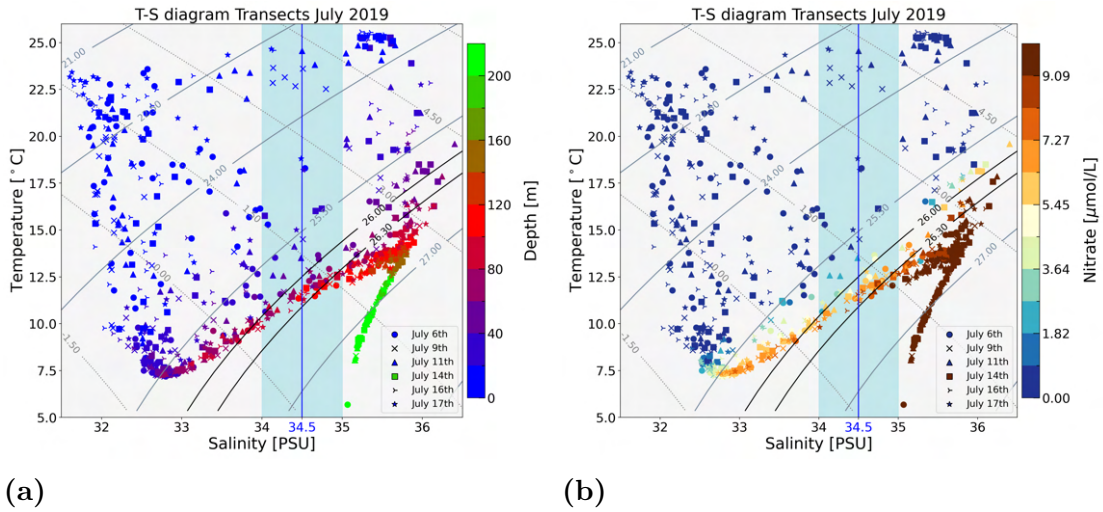


**Figure 4.8:** Temperature vs salinity diagram for all the transects from the July 2019 cruise. Panel (a) colormap represents depth; panel (b) colormap represents nitrate concentration. The light-blue area represents the isohalines corresponding to the frontal water mass. Salinity  $< 34$  PSU represents *shelf waters*,  $S > 35$  PSU corresponds to *slope water*. The blue vertical line emphasizes the mean frontal position. The grey solid lines represent density contours [ $\text{kg}/\text{m}^3$ ]; the grey dotted lines represent spiciness [ $\text{kg}/\text{m}^3$ ].

to  $\tau > 3 \text{ kg}/\text{m}^3$  and salinity greater than 35.8 PSU. However, small changes can be associated with different seasonal conditions. Frontal waters are less spicy,  $\tau = [0.5 - 1.50] \text{ kg}/\text{m}^3$ , where the lowest values were in April and increased toward July.

Relative to nitrate, as already described in Section 4.2.1, the surface depletion was almost not present during April, except for the last two days of the cruise when a warmer and saltier water mass intruded above the slope. Afterward, it increased during May and July as soon as mixing decreased and stratification increased. This is even clearer looking at the number of data points around 0 in Figure 4.9: minimum in April and maximum in July. The range of nitrate concentrations along the transect was wide:  $[0 - 25] \mu\text{mol}/\text{L}$ . In general, nitrate was low ( $< 1 \mu\text{mol}/\text{L}$ ) for high salinity and high temperature values in the surface layer, and high ( $> 10 \mu\text{mol}/\text{L}$ ) to the deepest mid-temperature and salty slope water. The highest concentration of nitrate was found for depths greater than 120 m and density over  $26.6 \text{ kg}/\text{m}^3$ , except for April where the density was  $26.8 \text{ kg}/\text{m}^3$  over the slope. Within the frontal region nitrate concentration was within  $[0 - 10] \mu\text{mol}/\text{L}$ , except for April where the minimum value was  $\sim 4 \mu\text{mol}/\text{L}$ . It is interesting to note that the region where the concentration of nitrate was  $\geq 10 \mu\text{mol}/\text{L}$  was always centered with the off-shore side of the front location ( $S \geq 34.5$ ), suggesting a Gulf Stream nutrient source [Palter and Lozier, 2008].

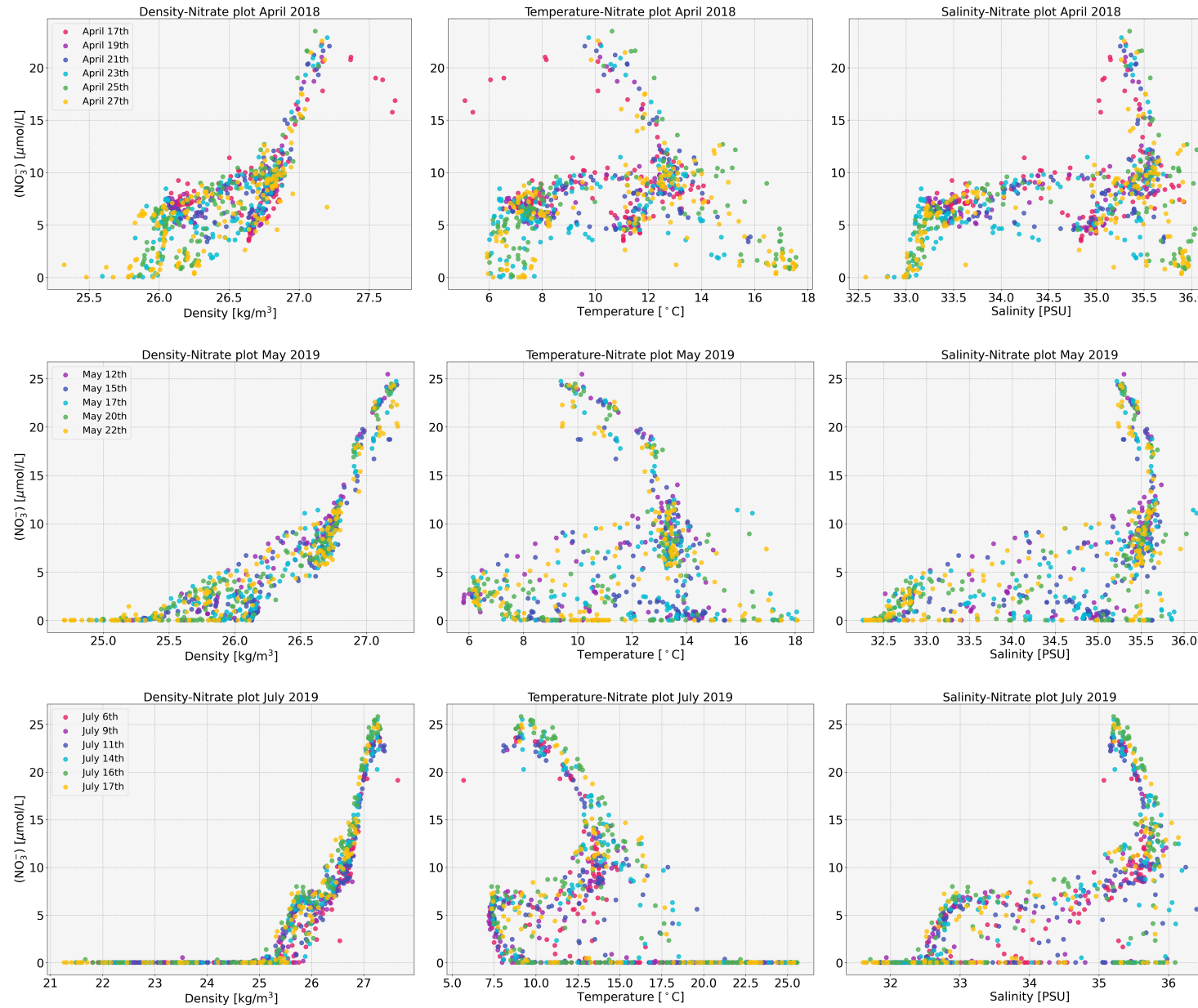


**Figure 4.9:** Density, temperature, and salinity vs nitrate concentration. First row: distributions for all the individual transects for the April 2018 cruise. Second row: distributions for all the individual transects for the May 2019 cruise. Third row: distributions for all the individual transects for the July 2019 cruise.

On the other hand, over the continental shelf ( $S < 34$ ), the concentration was up to  $\sim 7\text{-}8 \mu\text{mol/L}$ , also within the *cold pool*, which was significantly high compared to climatological values [Zhang et al., 2013]. Nitrate  $< 10 \mu\text{mol/L}$  were spread for the majority of the temperatures range; in April there was a lack of low nitrate for  $T = [8 - 13] \text{ }^\circ\text{C}$ : a further indication that strong mixing was occurring; in May and July concentration of about  $2\text{-}3 \mu\text{mol/L}$  between  $T = [16 - 18] \text{ }^\circ\text{C}$  was an indication of subsurface mixing.

### 4.2.2 Accumulated properties change

The first approach to the study of BBL detachment has been the analysis of the accumulated properties change (APC). In particular, along-isopycnal changes in the off-shore direction of temperature (ATC), salinity (ASC), and nitrate (ANC) have been computed. The APCs have been calculated for all the available transects collected in the three oceanographic cruises, using the algorithm proposed by Pickart [2000] and described in Chapter 2.1.1. In the following sections, only some relevant sections have been reported but the complete plots are shown in Appendix A.

#### Bottom boundary layer detachment identification

It has already been shown by Pickart [2000] and Linder et al. [2004] that, at least for the MAB frontal system, the ATC technique accurately detects the presence (or absence) of the detached BBL. Evidence of detachment, minima at the bottom and extending toward the surface in a tongue shape, were searched for in the fields of temperature and salinity. We look simultaneously at both ATC and ASC minima because temperature changes could result from other processes besides detachment (i.e. heating/cooling), whereas salinity is a more passive variable, whose changes have a longer timescale compared to temperature.

If the detachment layer is transporting water both off-shore and upward along the density surfaces, then the isopycnals should be characterized by relatively small lateral changes not only in temperature and salinity but also in nitrate below the euphotic zone. Thus, for those days where a significant signal of BBL detachment was found in both temperature and salinity tracers, the same calculation has been done for the high-resolution nitrate sections. Afterward, some relevant case study sections are presented for the different cruises in order to show the most significant variability affecting the structure of the BBL detachment.

**April 2018** In general, during April the detached layer extended from the bottom up to the surface, confirming the correspondence with the early spring conditions described by Linder et al. [2004]. A good example of well-defined ATC, ASC, and ANC minima is the transect from 19th April 2018, shown in Figure 4.10 (a, c and e).

## 4.2 Nutrient transport induced by bottom boundary layer detachment

The isopycnals centering the ATC and ASC minima in the bottom boundary layer were along  $[26.4 - 26.6]$   $\text{kg/m}^3$  and the maximum extension of the tongue (defined by the  $\text{ATC} = 1.0$   $^\circ\text{C}$  contour [Linder et al., 2004]) stretched within  $\sim 30$  m of the surface. Almost the same structure has been found for the ANC even though this minimum was centered on slightly lighter isopycnals compared to the one of the ATC:  $[26.3 - 26.5]$   $\text{kg/m}^3$ . Similarly, the vertical scale of the nitrate tongue was defined as the  $\text{ANC} = 2$   $\mu\text{mol/L}$  contour; thus also the ANC minima extended from the bottom to within 30 m of the surface.

On the other hand, off-shore water masses interfered at the surface (see the increased vertical stratification closer to the surface in the last two rows in Figure 4.3) flattening the isopycnals and also affected the BBL structure. One example of that is the section from the 27th of April. In fact, looking at Figure 4.10 (b, d, and f) cannot be identified a clear signal of the detachment of the BBL using the defined criteria: the ATC minima was extended along all the shelf and shelf break without any indication of upward deflection. It is interesting to note that the ANC showed a structure resembling a detachment, but without any indication in the ATC and ASC fields, no other assessment can be inferred because the variability of nitrate concentration can be related to other causes.

Variability of the position of the detachment of the BBL throughout the days it has been studied extracting which isopycnals were found within the minimum of ATC/ASC and ANC. The results are summarized in Table 4.1.

Day of April	ATC central isopycnal [ $\text{kg/m}^3$ ]	ANC central isopycnal [ $\text{kg/m}^3$ ]
17	26.6	26.3
19	$[26.4 - 26.6]$	$[26.3 - 26.5]$
21	$[26.4 - 26.6]$	26.6
23	$[26.5 - 26.6]$	$[26.3 - 26.5]$
25	$[26.5 - 26.6]$	$[26.5 - 26.6]$
27	no significant signal	26.3

**Table 4.1:** Central isopycnals found within the detached BBL in the accumulated temperature, (hence also salinity) and nitrate change sections.

For those days where the signal of detachment was found, the central isopycnals were always in between  $[26.4 - 26.6]$   $\text{kg/m}^3$  for ATC (and also ASC). Furthermore, the position of ANC ranged between  $[26.3 - 26.6]$   $\text{kg/m}^3$  matching those of ATCs.

**May 2019** The cruise of May 2019 was the one most affected by the presence of frontal eddies impinging on the continental shelf and distorting the front. In fact, none of the sections show a clear indication of detachment (see from Figure A.7 to

#### 4 Physical drivers for chlorophyll- $\alpha$ variability

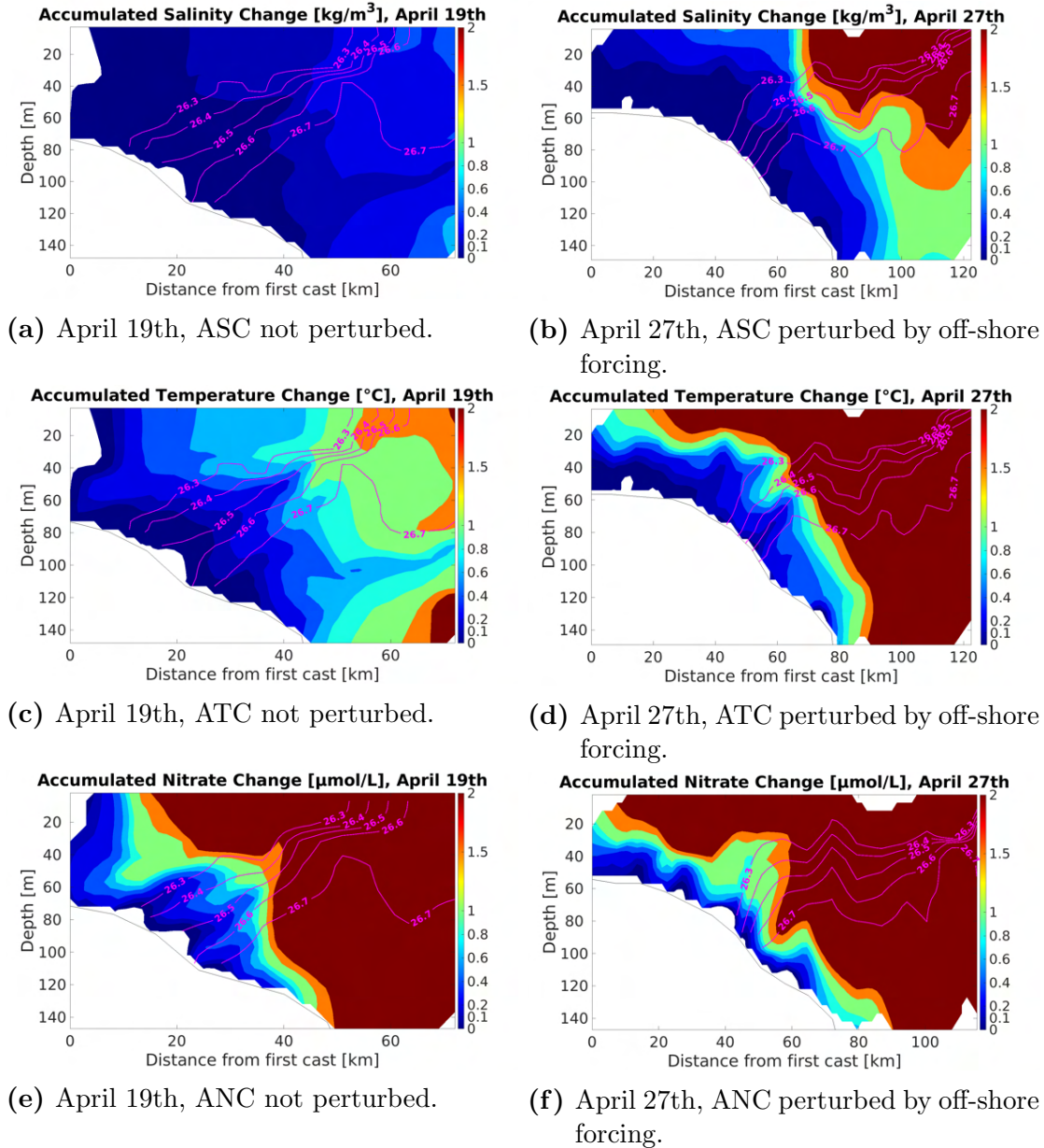


**Figure 4.10:** Accumulated properties change for some relevant sections in April 2018. The 19th of April represents a typical not perturbed frontal structure; in contrast, on the 27th the bottom boundary layer was affected by off-shore forcing. The magenta contours represent isopycnals  $[\text{kg}/\text{m}^3]$ .

## 4.2 Nutrient transport induced by bottom boundary layer detachment

---

A.11 in Appendix A); as a consequence, no ANC was calculated. For almost all the sections the BBL structure arising from ATC was quite flat close to the bottom. The ASC contours were almost horizontal over the slope but became steeper close to the surface following the isopycnal distributions.

**July 2019** During July there were two main factors affecting the BBL structure: the seasonal pycnocline becoming fully developed and a streamer originating from a Gulf Stream warm-core ring passing through some sections. Both of them inhibited the vertical penetration of the ATC minima in the water column.

A good example of the streamer perturbed conditions was found for the transect of the 6th July shown in Figure 4.11 (a, c and e). There was no clear indication of detachment in the ATC and ASC: both contours fluctuated without any explicit tendency. Therefore, the ANC minimum found along the 26.3 isopycnal can not be strictly related to BBL detachment. However, this supports the idea that off-shore water masses can disturb the frontal structure, also affecting the convergence and the upwelling process acting in the BBL.

In contrast, an expected case of unperturbed summer conditions was found for the transect on 9th July shown in Figure 4.11 (b, d and f). There was a distinct minimum, for both ATC and ASC, centered around 26.15  $\sigma$  and extending from the bottom up to  $\sim 60$  m from the surface. An analogous minima, centered on the same isopycnal, was found for the ANC. That was a clear indication that the BBL detachment is a consistent feature of the MAB shelf break front when it is not perturbed by external forcing and it is able to be fully restored after such interactions. Furthermore, the signal of the detachment was particularly strong during this day and very well delineated compared to the other not perturbed section (see Appendix A Figures from A.14 to A.17). Possibly because this was during a transition phase from the streamer perturbed conditions. The surface stratification was not completely restored (see Figure 4.5) but also the off-shore forcing was no longer intense enough to alter the BBL. The foot of the front was particularly flat close to the bottom, becoming steeper in the following days, suggesting that the downslope flow was increased, enhancing the detachment of the BBL. On the following day, the front stabilized with the intrusion of denser and saltier water mass over the slope, increasing the upslope flow and reducing the detachment.

In general, considering the relative position of the ATCs vs ANCs minima, it can be concluded that the nutrient transport occurs on the on-shore side of the front.

During summer the ATC minima dropped to around 60 m below the surface; almost twice as deep compared with April. The range of isopycnals associated with ATC and ANC minima is wider and they are centered along lighter density contours compared

#### 4 Physical drivers for chlorophyll- $\alpha$ variability

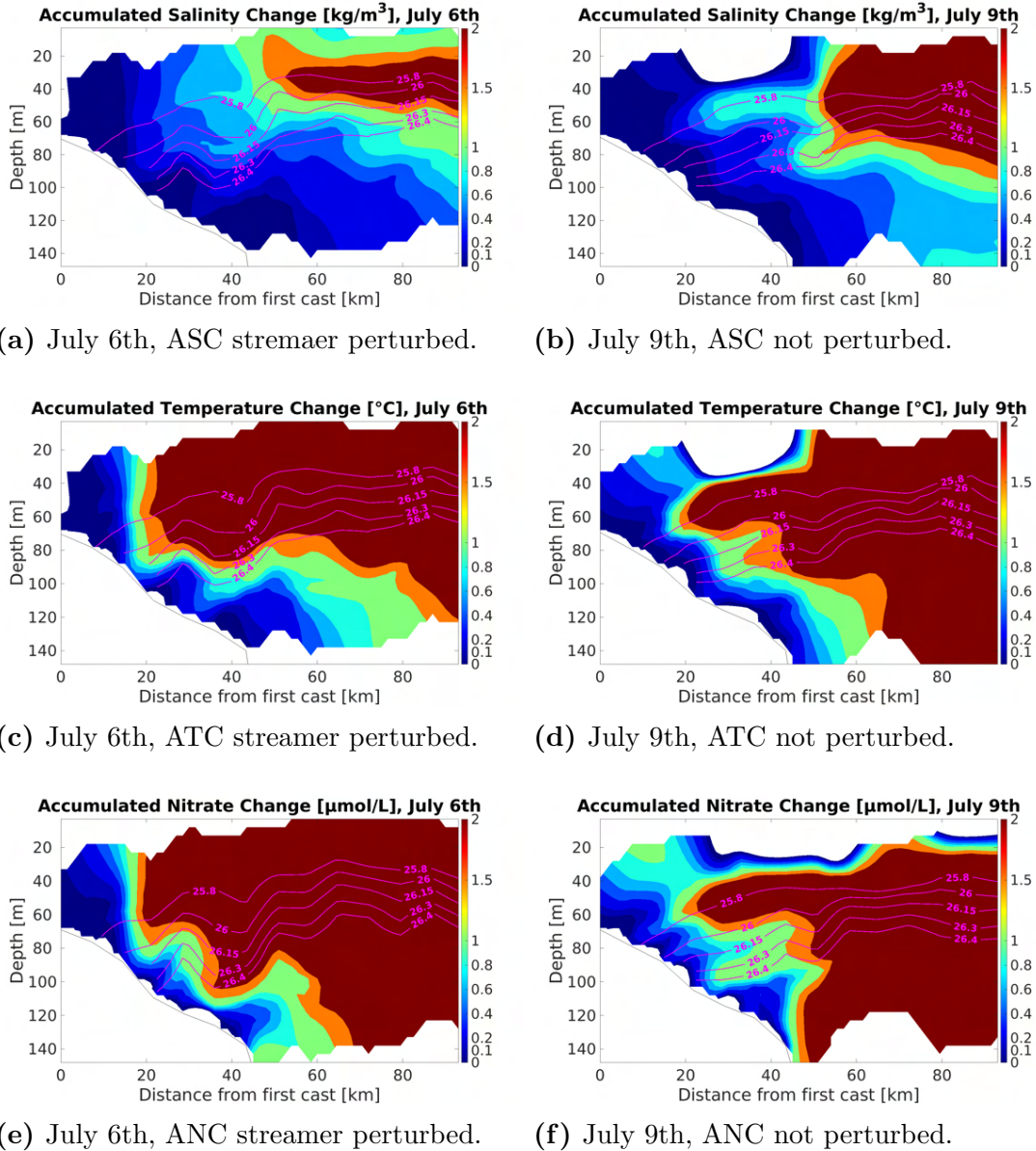


**Figure 4.11:** Accumulated properties change for some relevant sections in July 2019. The 9th July represents a typical not perturbed frontal structure; in contrast, on the 6th the bottom boundary layer was affected by off-shore forcing. The magenta contours represent isopycnals [kg/m<sup>3</sup>].

## 4.2 Nutrient transport induced by bottom boundary layer detachment

to April (table 4.2). This is consistent with the tendency found by the climatological analysis of Linder et al. [2004].

Day of July	ATC central isopycnal [kg/m <sup>3</sup> ]	ANC central isopycnal [kg/m <sup>3</sup> ]
6	no significant signal	26.3
9	[26.0 - 26.2]	26.1
11	26.0	[26.0 - 26.1]
14	[26.3 - 26.4]	[26.0 - 26.1]
16	26.3	26.4
17	26.0	26.0

**Table 4.2:** Central isopycnals found within the detached BBL in the accumulated temperature, (hence also salinity) and nitrate change sections.

In addition, it can be concluded that not only does the off-shore forcing modify and reduce the vertical penetration of the detached BBL within the water column, but also the increased strength of the thermocline at the surface, as already found by Linder et al. [2004]. Both reduce the vertical extension of the ATC minima within the water column, which is the significant layer hypothesized to carry the nutrients from the rich environment close to the bottom, up to the depleted surface, within the euphotic zone. To assess if this process can affect the surface and subsurface primary production, along with isopycnal changes in properties are investigated in the following section.

### 4.2.3 Along isopycnal change in properties

The main hypothesis of this work is that nutrients are carried upward from the layer detaching in BBL in association with the front, enriching nutrients in the euphotic zone and increasing primary production. According to the theory of how the detached layer in the BBL is created, as explained in Chapter 1.1, some target isopycnals were chosen along with estimating the differences between the concentration of nitrate, PON, and Chl- $\alpha$  at the bottom end and closer to the surface, below the euphotic zone. In particular, in all the available sections have been chosen as target isopycnals:

1. the isopycnal intersecting the foot of the front (corresponding to the bottom end of the 34.5 isohaline) in the BBL;
2. the isopycnal found in the center of the ANC minima.

Thus, the ANC sections have been used as an indication of where the BBL detachment was occurring and when it was warranted to calculate the delta along isopycnals. If no significant ANC minimum<sup>2</sup> indication was detected, only the isopycnal

<sup>2</sup>The ANC minimum signal is significant when associated with an ATC minimum centered on the same isopycnal.

#### 4 Physical drivers for chlorophyll- $\alpha$ variability

---

identified by the first criteria has been used for the calculation. Once the suitable transects were selected, to settle on how far extend along the isopycnals for the estimation of the delta, the criteria of the isopycnal outcrop in the euphotic zone or crossing the 34.75 PSU, has been applied. The sections not satisfying this methodology were excluded. For all the suitable sections the hypothesis of along-isopycnals variation  $-\Delta(NO_3^-) \approx \Delta(\text{PON})$  and  $-\Delta(NO_3^-) \sim \Delta(\text{Chl-}\alpha)$  has been tested.

##### **Verification of the applicability of the criteria**

The APC sections have been used to select the suitable sections and the isopycnals at the center of the ANC minima (see Table 4.1 and 4.2). When the ANC minimum was found within an interval, the mean value was considered. In addition, from the CTD PAR variable has been calculated the 1% light level depth as explained in Chapter 2.1.2. The results are summarized in Figure 4.12.

No signal of BBL detachment was found during the cruise of May 2019, due to strong frontal eddy interactions with the front, thereby those sections had to be rejected. In addition, neither of the criteria for the isopycnals crossing the 34.75 isohaline or the 1% light level was suitable. The frontal surface was steep and shifted significantly closer to shore because of the presence of the eddy around 39.9°N. As soon as the eddy passed, during the last two available days, the front became shallower and it had a greater extension over the slope; however, the density surfaces were still perturbed (see Figure 4.4) and the 26.45 isopycnal was crossing many times the 34.75 isohaline. Consequently, in the latter analysis, only the April and July transects will be considered.

For April, the 26.6  $\sigma$  was the isopycnal hitting the foot of the mean location of the front in the BBL, nevertheless also the average position of the ATC minima was found along this isopycnal, or 0.1-0.2 kg/m<sup>3</sup> lighter. In addition, the ANC minima were always within this range of density surfaces. As a consequence of that, it can be concluded that the detachment of the BBL is occurring on the on-shore side of the front, over the shelf.

In Table 4.3 are reported day by day the references of the latitudes used to extract the linearly interpolated value along each target isopycnal and which criteria have been applied to identify the more off-shore point (light or isohaline) along the isopycnals. Therefore, all the transects were suitable for the calculation, even if for the 27th of April only the criteria of the isopycnals hitting the foot of the mean location of the front was satisfied because no significant signal of BBL was detected.

On the other hand, the same analysis has been done for the July sections and an analogous table has been filled (see Table 4.4). The first target isopycnal was 26.3  $\sigma$

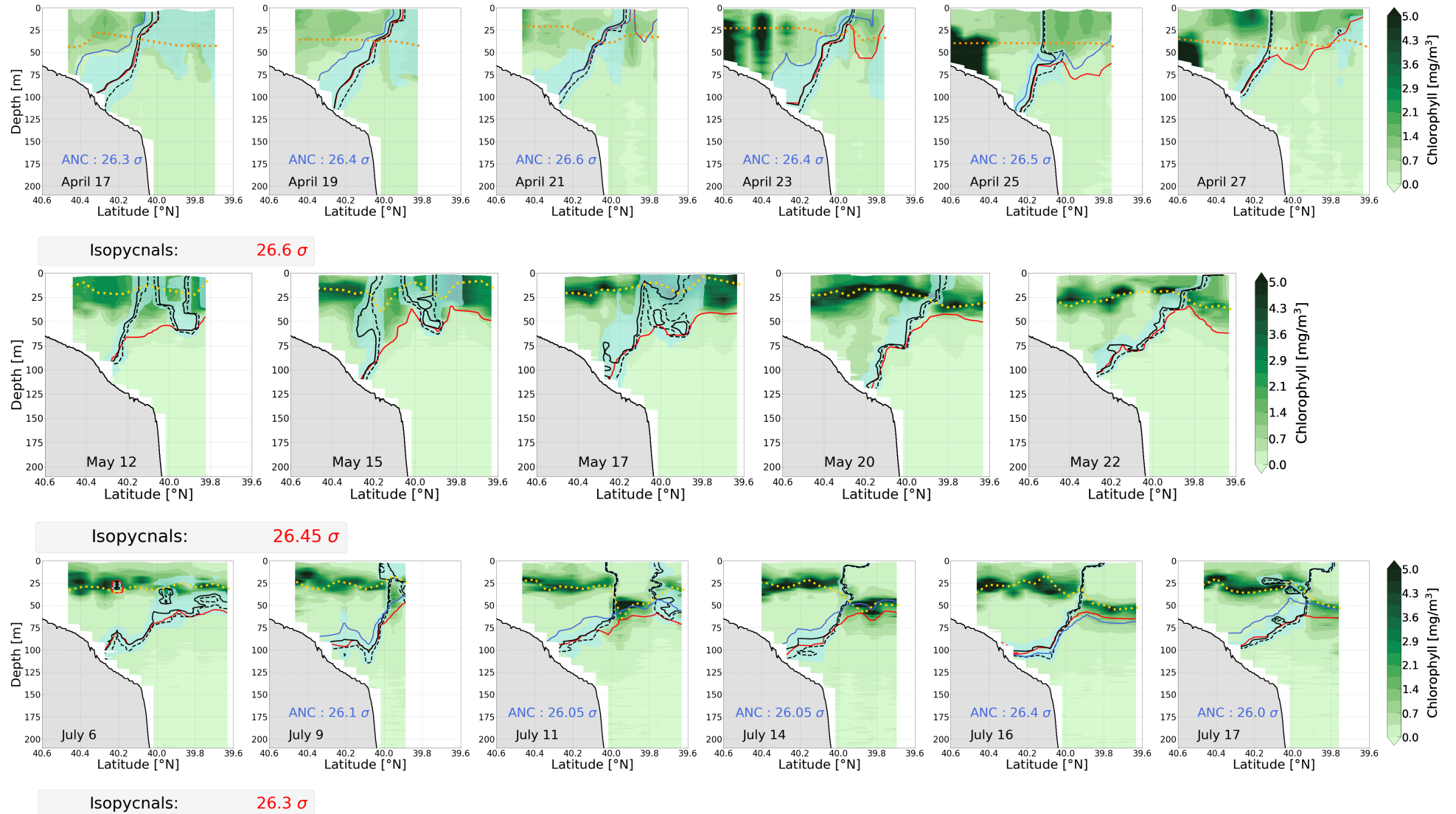


**Figure 4.12:** All the available transects from the three cruises; from top to bottom: April 2018, May 2019, and July 2019. The colormap represents the calibrated chlorophyll- $\alpha$  from the CTD. The light-blue area represents the front surface (from 34.0 to 35.0 PSU) and the black dashed line is the mean position of the front (34.5 PSU). The red line represents different isopycnals whose values are reported in each legend, instead the blue line is the isopycnal in the center of the ANC minima, different for each day. The yellow (orange for April) dotted line represents the estimated 1% light level from daily CTD casts.

#### 4 Physical drivers for chlorophyll- $\alpha$ variability

Day of April	Target isopycnal [kg/m <sup>3</sup> ]	Initial lat. [°N]	Final lat. [°N]	Criteria
17	26.3	40.39	40.13	light
	26.6	40.33	40.07	light
19	26.4	40.33	40.01	light
	26.6	40.27	40.01	light
21	26.6 <sup>3</sup>	40.26	40.07	light
23	26.4	40.33	40.07	light
	26.6	40.27	40.01	PSU
25	26.5	40.20	40.01	PSU
	26.6	40.20	40.01	PSU
27	26.6	40.27	40.08	PSU

**Table 4.3:** Target isopycnals for the calculation of the  $\Delta$ s. The initial latitude represents where the isopycnal intersects the bottom; the final latitude represents the endpoint for the calculation chosen as indicated by the criteria in the last column.

for all the transects, instead, the one corresponding with the center of the ANC minima was different for each day, varying in a wider range compared to April. As for the 27th of April, the former criteria could not be applied to the 6th of July. However, it can be confirmed, also for this month, that the detachment of the BBL is on the on-shore side of the front. In the following section, the results from the calculation of the  $\Delta$ s are investigated.

#### Testing the hypothesis of nutrient transport

The  $\Delta$ s have been calculated along each isopycnal separately because each of these has been considered independent from each other. This has been justified by noting from the APC sections (see Appendix A) that, when occurring, the detachment is narrow on a few density contours, and a shift of only 0.1 kg/m<sup>3</sup> could identify a completely different configuration of the isopycnals. In addition, it has been checked from the raw distribution of the Niskin bottles samples effectively each contour was sampled by a different bottle. The mean extension of the tongue of the detached BBL was around 30 m of the surface during April and up to 60 m for July; thus at the edge of the estimated 1% light level depth for both seasons. Thereby, the differences represent the variation, linearly interpolated along each isopycnal, of the concentration of nitrate (NO<sub>3</sub><sup>-</sup>), PON, and Chl- $\alpha$  below the euphotic zone. The 1% light level depth is a rough estimation of the region in the water column where the contribution of the incoming light is greater to primary production, hence calculating along isopycnals variations of the nutrients below this zone, allowing to exclude this kind of variability. It is important to point out that, the depth of the endpoint along

<sup>3</sup>The two target isopycnals were coincident.

## 4.2 Nutrient transport induced by bottom boundary layer detachment

Day of July	Target isopycnal [kg/m <sup>3</sup> ]	Initial lat. [°N]	Final lat. [°N]	Criteria
6	26.3	40.27	39.88	PSU
9	26.15	40.33	39.94	PSU
11	26.3	40.27	40.01	PSU
	26.05	40.27	39.94	PSU
14	26.3	40.27	40.08	PSU
	26.05	40.33	39.94	PSU
16	26.3	40.27	40.01	PSU
	26.4	40.33	40.01	PSU
17	26.3	40.33	40.01	PSU
	26.0	40.33	39.87	PSU
	26.3	40.27	39.94	PSU

**Table 4.4:** Target isopycnals for the calculation of the  $\Delta$ s. The initial latitude represents where the isopycnal intersects the bottom, the final latitude represents the endpoint for the calculation chosen as indicated by the criteria in the last column.

the isopycnals was always within the tongue of the calculated BBL detachment. When this criterion could not be applied because the isopycnals were bending below the increased surface stratification and not outcropping in the euphotic zone; then the point where the isopycnal was crossing the off-shore side of the front (34.75 PSU) was considered. To evaluate the strength of the hypothesis proposed, the *Pearson correlation coefficient* and the *p-value* have been calculated and reported on each plot shown in Figures 4.13 and 4.14.

The hypothesis that  $-\Delta(NO_3^-) \approx \Delta(\text{PON})$  and  $-\Delta(NO_3^-) \sim \Delta(\text{Chl-}\alpha)$  is confirmed by the negative values of  $R^2$ . On the contrary, the *p-values* are overall greater than 0.1 which is the usual upper threshold. However, it must be considered that this methodology looks at the process as a two-dimensional one, neglecting the variability related to the along-shelf dimension (all the transects are cross-shelf). Furthermore, this process may also be influenced by various other factors that impact front stability, including off-shore forcing. Its lagged effects may have been detected through the positive change in nitrate (indicating an increase in concentration with decreasing depth)  $\Delta(NO_3^-)$  calculated along the 26.05  $\sigma$  for the 11th July and along the 26.3  $\sigma$  for the 14th July. They are highlighted in orange, respectively, in Figure 4.14 (a) and (b), and they were excluded from the linear regression estimation due to their representation of different phenomena. Notably, these processes, possibly associated with internal wave propagation within the water column after the streamer was passed or nitrogen fixation/regeneration, deviated significantly from the hypothesis of this work. However, in Figures 4.13 and 4.14, the statistical indices have been calculated

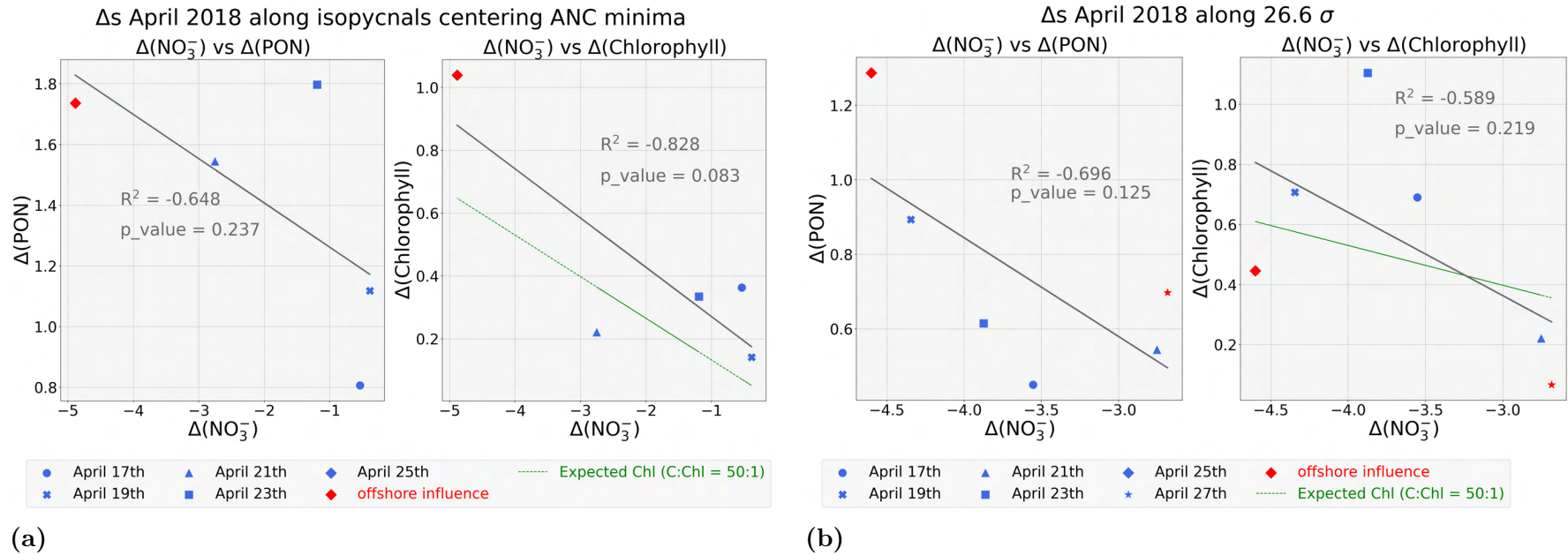
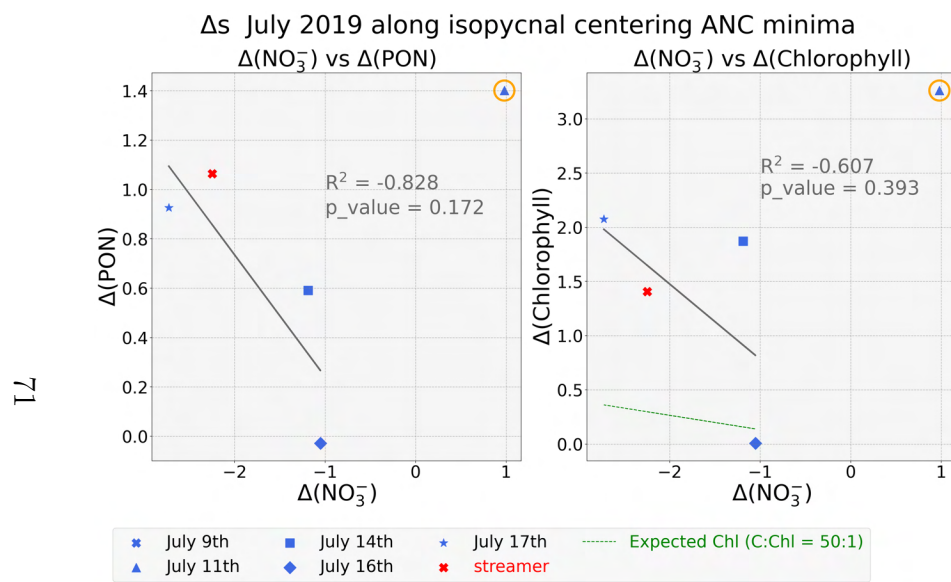
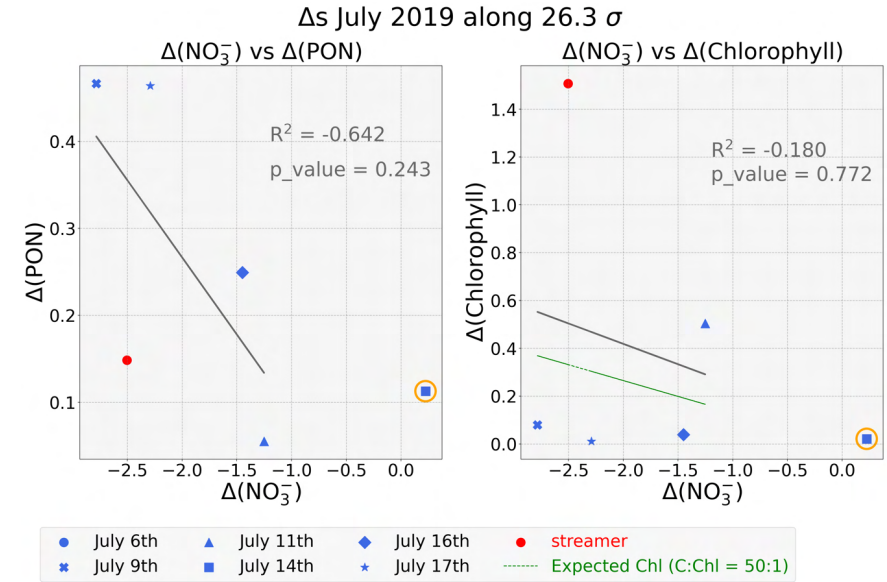


**Figure 4.13:** Left panel:  $\Delta$ s calculated along the isopycnals, different for each day, found at the center of the ANC minima. Right panel:  $\Delta$ s calculated along the isopycnal hitting the foot of the front (34.5 PSU) in the BBL. Each day of April has a different marker, as indicated in the legend. In red are emphasized the days when the off-shore forcing was significant. The gray line represents the regression line and the green line is the theoretical C:Chl regression line.



17

(a)



(b)

**Figure 4.14:** Left panel: Δs calculated along the isopycnals, different for each day, found at the center of the ANC minima. Right panel: Δs calculated along the isopycnal hitting the foot of the front (34.5 PSU) in the BBL. Each day of July has a different marker, as indicated in the legend. In red are emphasized the days when the off-shore forcing was significant. The gray line represents the regression line and the green line is the theoretical C:Chl regression line. The orange round contours highlight the data points excluded in the linear regression estimation.

#### 4 Physical drivers for chlorophyll- $\alpha$ variability

---

while incorporating the data points associated with perturbed conditions. It is worth noting that, despite the presence of off-shore streamer data, there remains a discernible and meaningful signal within the computed deltas.

Furthermore, the PON is not only contained in biological living particles but also in non-living sediments, thus the observed values are also affected by bottom sediments and, close to the surface, by the dust transported by winds. Regrettably, there was no practical way to separate them during the measurements.

Lastly, the photoadaptation of phytoplankton must be considered to interpret the observed Chl- $\alpha$ . The chlorophyll concentrations are estimated from the calibrated CTD fluorescence (see Chapter 2.1), but phytoplankton has the ability to concentrate the available light to maximize the production of chlorophyll. This is particularly true when the bloom appears below the surface (see Figure 4.12, third row) where the amount of light decreases. Thus, high fluorescence values do not always correspond to high biomass. This is evident in the differences calculated for the July sections, along the 26.3  $\sigma$  (Figure 4.14 (b)), which was the deepest isopycnal among those chosen. Except for the highest value associated with the clearer streamer waters, all the others were less than 0.5  $\mu\text{mol}/\text{m}^3$ .

For all the reasons above, the considerable scattering affecting the data can be explained and it could be reduced by having more suitable transects to apply this methodology. Possibly, increasing the data sample would improve the *p-value* statistic. In conclusion, in a first-order approximation where the third dimension is neglected, the nutrients upwelled by the BBL detachment lead to a biological response.

# Chapter 5

## Conclusions and outlooks

The shelf break front at the Mid-Atlantic Bight shelf-break hosts a large and productive marine ecosystem supported by high phytoplankton concentrations. This significant productivity is driven by several upwelling mechanisms associated with the presence of the front and with the Gulf Stream submesoscale structures that interact with the continental shelf. The main objective of this work was to investigate the link between one of these upwelling mechanisms and the observed enhanced surface and subsurface Chl- $\alpha$  concentration at the shelf break front.

Despite the various upwelling mechanisms, it is noteworthy that the concentrations of Chl- $\alpha$  in the shelf break region do not consistently exhibit enhancement throughout the year. The present study has examined the inter-annual variability of surface Chl- $\alpha$  from 2003 to 2020 linked to environmental factors, including surface winds, surface temperature, salinity, and horizontal velocities. In particular, the seasonal trend for wind speeds presents higher magnitude during winter and lower speeds in summer, with values ranging from 2.4 m/s to  $\sim 5$  m/s. In general, wind direction was perpendicular to the coast throughout the seasons: predominantly eastward in Spring, northeast in Summer, and southwest during Autumn and Winter, hence enabling upwelling due to the displacement of water far away from the coast.

As expected, the surface Chl- $\alpha$  concentration displays a periodic variability, characterized by seasonal and intra-seasonal peaks, which align with the Spring and Autumn blooms. This periodic signal exhibits a noteworthy degree of coherence with surface wind variability. However, it is important to highlight that no significant peak with a period within 100 and 60 days was found, but there was a weaker but meaningful coherence for periods around a month and within the range from 10 to 7 days. These findings suggest that wind-driven dynamics drive the seasonal and intra-seasonal variability of surface Chl- $\alpha$  concentration, but in general, this

## 5 Conclusions and outlooks

---

is not true for short-period enhancements, which are driven by other mechanisms. Furthermore, while enhancements in Chl- $\alpha$  concentrations are observable within the shelf break region of the MAB, such enhancements were not consistently detected in climatological and inter-annual analyses. This observation leads us to conclude that they represent a transient feature of the shelf. Interestingly, despite occasional short-lived Chl- $\alpha$  concentration enhancements, lasting only a few days, that may be attributed to wind-induced processes (see [Oliver et al. \[2022\]](#)); there is no discernible correlation between short-term Chl- $\alpha$  concentration variability and surface winds. Consequently, we infer that the variability of the observed enhancements in this area is not primarily driven by wind dynamics, but is the combination of many upwelling mechanisms.

Moreover, examining sea surface temperature, salinity, and currents, the frontal structure at the shelf break was evident in the horizontal gradients, showing distinct seasonal variations. Surface water homogenized in summer, reaching approximately 23 °C, while it decreased to around 13 °C in autumn and winter. Salinity exhibited a strong horizontal gradient in summer, with lower values close to the coast, persisting throughout the year but less intense in colder seasons. Sea surface currents were primarily influenced by the Gulf Stream in the southern part of the region, and the Shelf Break Jet around 40°N, with varying intensities observed throughout the year. Overall, these findings provide a comprehensive understanding of the dynamic oceanographic conditions in the study area.

Furthermore, the hypothesis that nutrient transport induced by the bottom boundary layer detachment can lead to a biological response has been tested. Based on prior research, it has been established that the pronounced ocean pressure gradient is responsible for sustaining the front at the shelf break [[Linder et al., 2004](#)]. The associated geostrophic adjustment of surface currents drives a convergence in BBL that leads to the uplift and off-shore transport of water masses. While this phenomenon had been primarily examined through seasonal analyses of temperature and salinity field variability of the front, our present study employs the Accumulated Property Change algorithm (APC), as developed by [Linder \[2005\]](#), to identify and characterize the detachment of the BBL in synoptic cross-shelf sections. The APC algorithm is applied to *in situ* data obtained during three distinct oceanographic cruises conducted as part of the SPIROPA project. The method, allows us to provide a comprehensive description of the variability of the BBL detachment. In particular, it has been found that the BBL detachment occurs on the on-shore side of the frontal surface and it can be strongly affected by the off-shore transport associated with Gulf Stream features, such as warm-core ring streamers and frontal eddies. The signal of the BBL detachment can be completely disrupted during these periods

---

of perturbed conditions and the modifications can last a few days after the passage of the perturbation. When no external factor was present, the BBL detachment was always detected with the APC method, confirming that it is a valuable procedure to detect this phenomenon for the MAB frontal system. The seasonal dynamic of the frontal system is also a key factor in the BBL detachment. In the case of summer high surface stratification, there is a pronounced downward compression of the detached tongue originating from the BBL. In contrast, under conditions of winter low surface stratification, the tongue can extend much closer to the water's surface. The extent to which the BBL tongue penetrates the water column can influence factors such as nutrient distribution, and consequently, the vertical distribution of phytoplankton abundance. To assess the importance of BBL detachment for nutrient upwelling, we have developed a method that evaluates changes in properties along isopycnals. Based on predefined criteria, we have selected specific target isopycnals and calculated the differences between a point closer to the surface and the concentration near the detachment of the BBL at the bottom. The BBL detachment at the bottom is taken as an indicator of nutrients upwelled in the water column and moving along isopycnals. Results show that the relationships between the decline of nitrate along isopycnals and the concurrent increase in phytoplankton biomass did not exhibit a simple pattern. While a general negative correlation between these variables was expected, the strength of this correlation was not consistent and robust for the data available. In some instances, the anticipated negative association between nitrate decline and phytoplankton biomass increase was observed, aligning with our initial expectations, but it was not always the case. This variability underscores the complexity of the relationship between nutrient availability (nitrate), phytoplankton biomass, and frontal dynamics. Moreover, it must be noticed that our interpretation of the phenomena is a two-dimensional simplification that completely neglects any variability associated with the lateral transport, which could have a significant influence on this process. However, on a first-order approximation, it can be concluded that there is a biological response led by the nutrients transported by the detaching BBL.

To further investigate these complex processes and enhance our understanding of the specific contributions of the various upwelling mechanisms in the region, would be interesting to develop a computational model capable of replicating the system and testing some of the dynamical hypothesis. In particular, it would be valuable to expand the modeling framework done by [Pickart \[2000\]](#), which simulated the detachment of the BBL at the shelf break front and the resulting secondary circulation, with a biogeochemical model, hence including nutrient cycling and the dynamics of phytoplankton growth and grazing. Such an attempt could provide valuable insights

## 5 Conclusions and outlooks

---

into the interconnected nature of physical and biogeochemical processes in the studied region, ultimately contributing to a more comprehensive understanding of the ecosystem's behavior and response to various environmental factors. This would be a significant step forward in the comprehension of the ecosystem dynamics of this region, in particular nowadays in the challenging contest of climate change which is significantly altering all the Earth's systems. Precisely, an inter-annual investigation of how the front at the MAB shelf break has changed in recent years, could be afforded using the time series provided by the *in situ* measurements collected with the NSF (*National Science Foundation*) Ocean Observatory Initiative's (OOI) Pioneer Array. This array has been operational in the region from April 2014 to November 2022. Moreover, this time series substantially aligns with the area sampled, since 2018 to the present, by the *Northeast U.S. Shelf Long Term Ecological Research* (NES-LTER) project. A joint effort in combine all these observations, will enhance our understanding of the dynamic changing occurring within the frontal system, particularly in response to the extensive influence of climate change.



**Figure 5.1:** Left: me collecting water samples from Niskin Bottles on board of the *R/V Endeavor*, during the summer oceanographic cruise EN706, in August 2023. Right: Scientific crew of the summer oceanographic cruise EN706 of the *Northeast U.S. Shelf Long Term Ecological Research* (NES-LTER) project.

# Appendix A

## Accumulated properties change figures

All the APC plots calculated are shown organized by cruise.  
April 2018

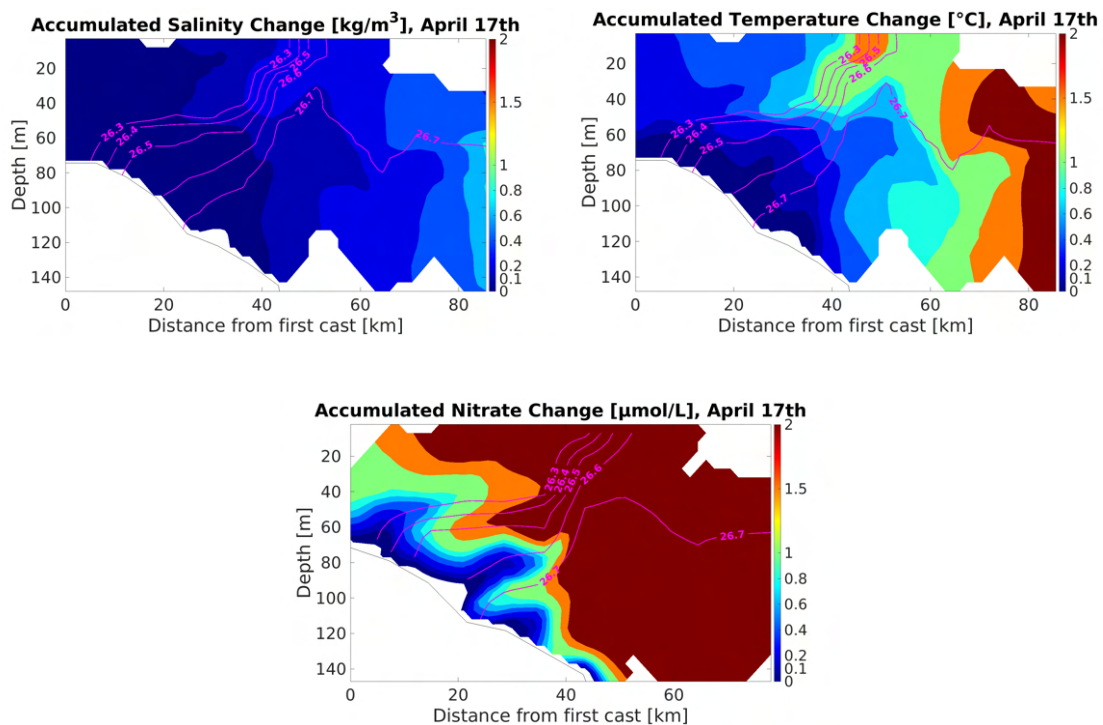


**Figure A.1:** From left to right: accumulated salinity (color), temperature (color), and nitrate (color) change at the 17th April. The magenta contours represent isopycnals [kg/m<sup>3</sup>].

## A Accumulated properties change figures

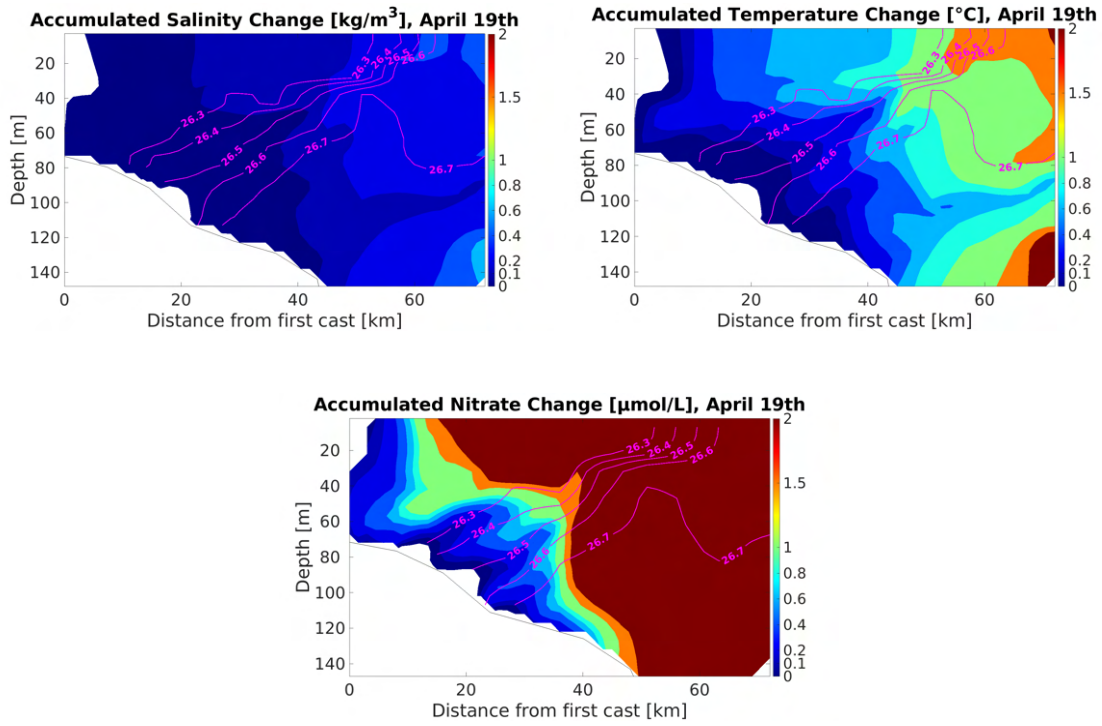


**Figure A.2:** From left to right: accumulated salinity (color), temperature (color), and nitrate (color) change at the 19th April. The magenta contours represent isopycnals [kg/m<sup>3</sup>].

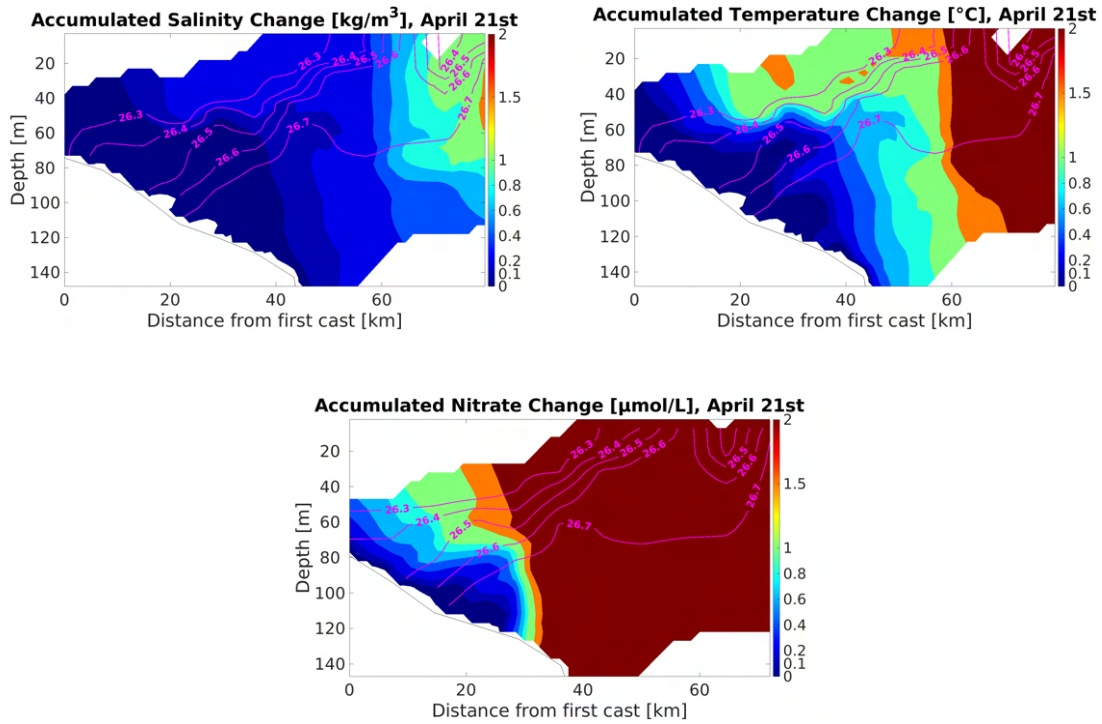


**Figure A.3:** From left to right: accumulated salinity (color), temperature (color), and nitrate (color) change at the 21th April. The magenta contours represent isopycnals [kg/m<sup>3</sup>].

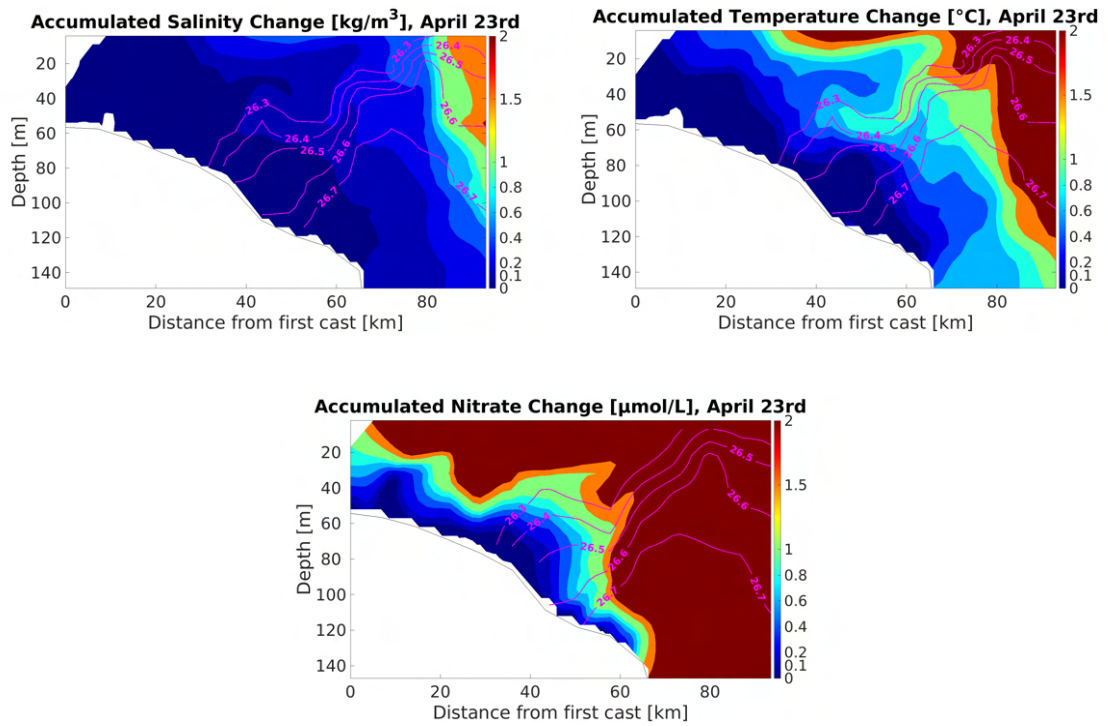


**Figure A.4:** From left to right: accumulated salinity (color), temperature (color), and nitrate (color) change at the 23th April. The magenta contours represent isopycnals [ $\text{kg}/\text{m}^3$ ].

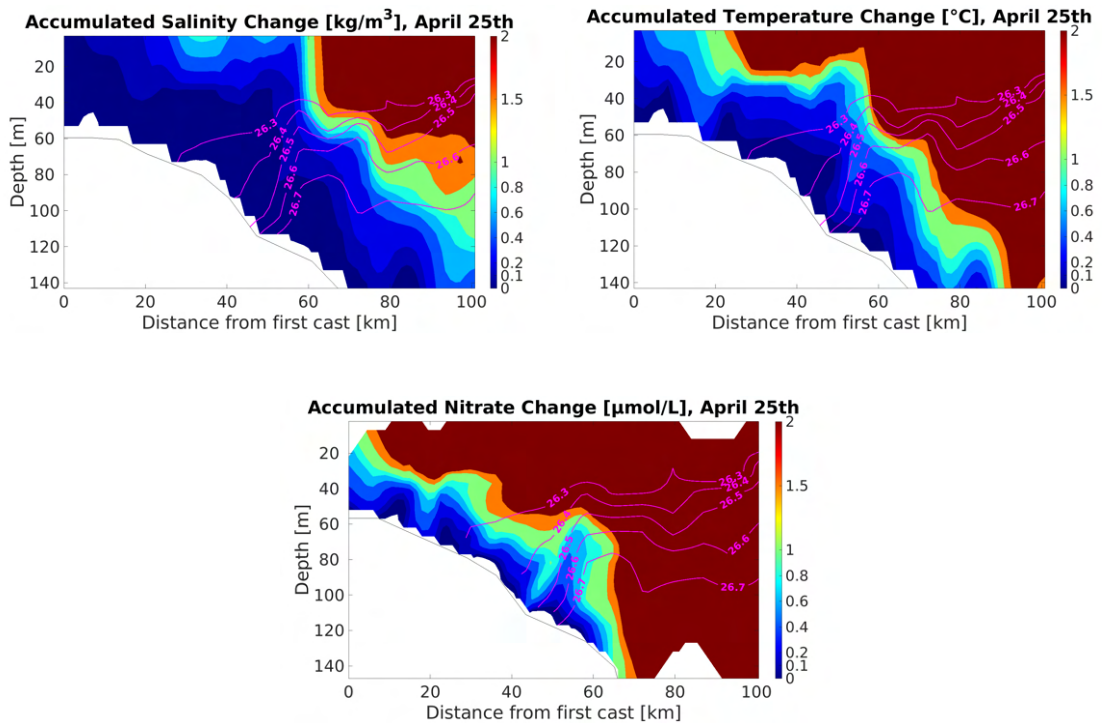


**Figure A.5:** From left to right: accumulated salinity (color), temperature (color), and nitrate (color) change at the 25th April. The magenta contours represent isopycnals [ $\text{kg}/\text{m}^3$ ].

## A Accumulated properties change figures

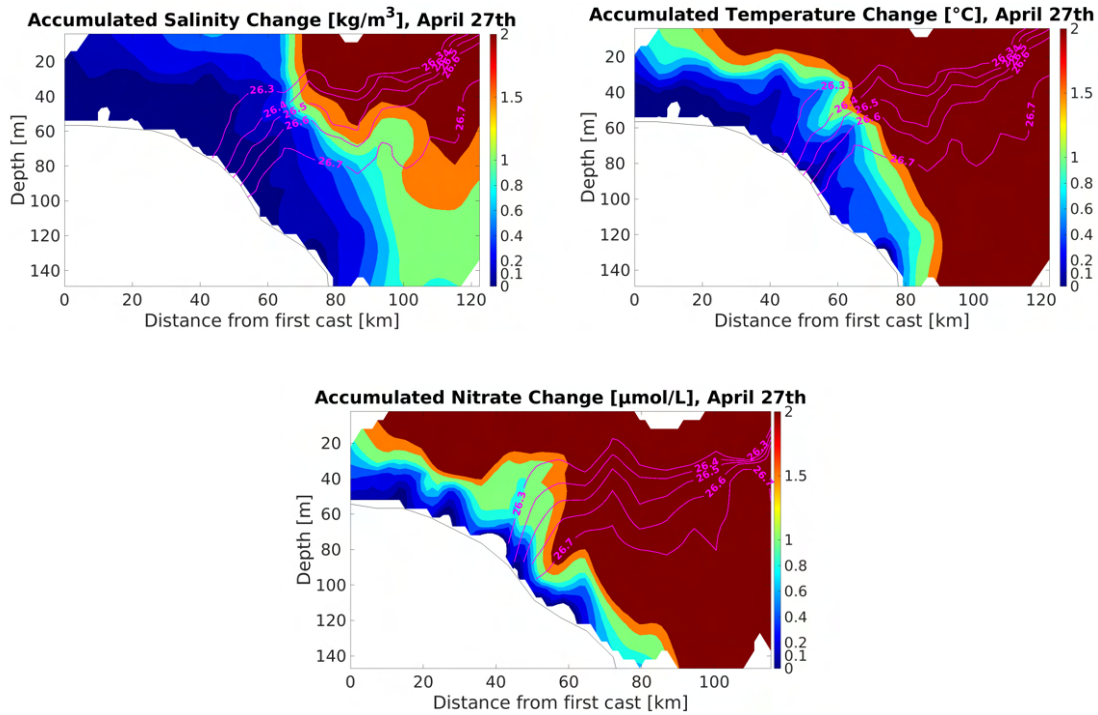


**Figure A.6:** From left to right: accumulated salinity (color), temperature (color), and nitrate (color) change at the 27th April. The magenta contours represent isopycnals [kg/m<sup>3</sup>].

May 2019

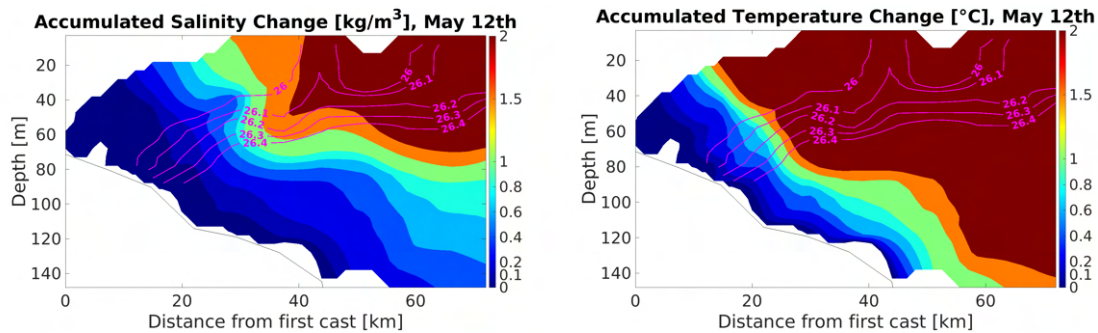


**Figure A.7:** From left to right: accumulated salinity (color) and temperature (color) change at the 12th May. The magenta contours represent isopycnals [kg/m<sup>3</sup>].

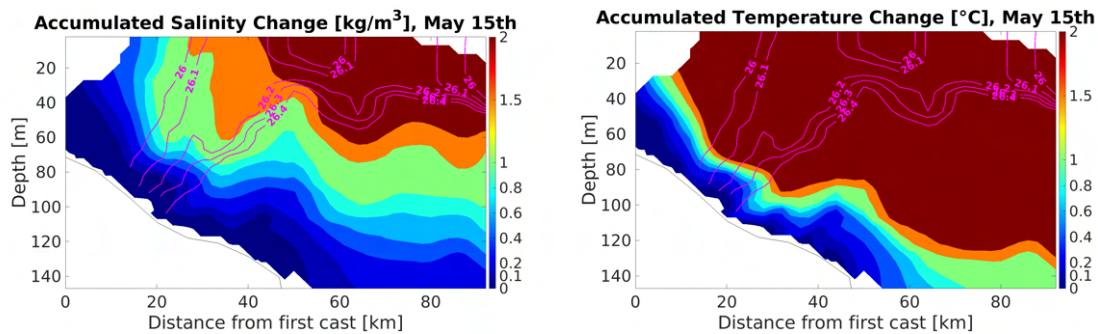


**Figure A.8:** From left to right: accumulated salinity (color) and temperature (color) change at the 15th May. The magenta contours represent isopycnals [kg/m<sup>3</sup>].

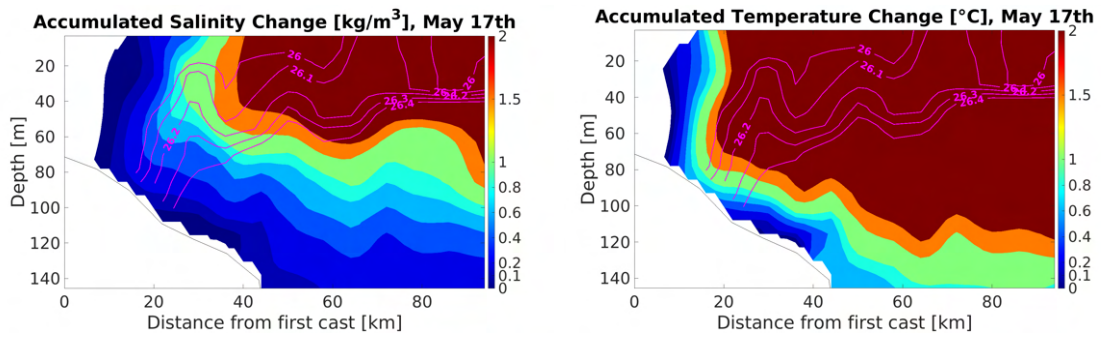


**Figure A.9:** From left to right: accumulated salinity (color) and temperature (color) change at the 17th May. The magenta contours represent isopycnals [ $\text{kg}/\text{m}^3$ ].

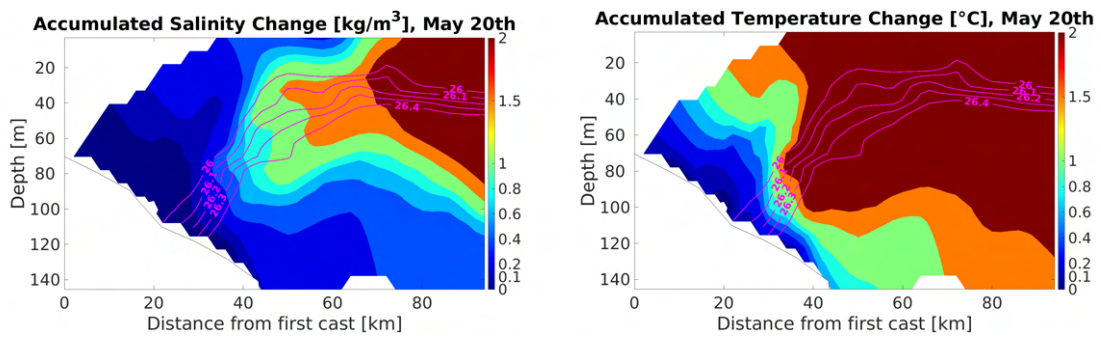


**Figure A.10:** From left to right: accumulated salinity (color) and temperature (color) change at the 20th May. The magenta contours represent isopycnals [ $\text{kg}/\text{m}^3$ ].

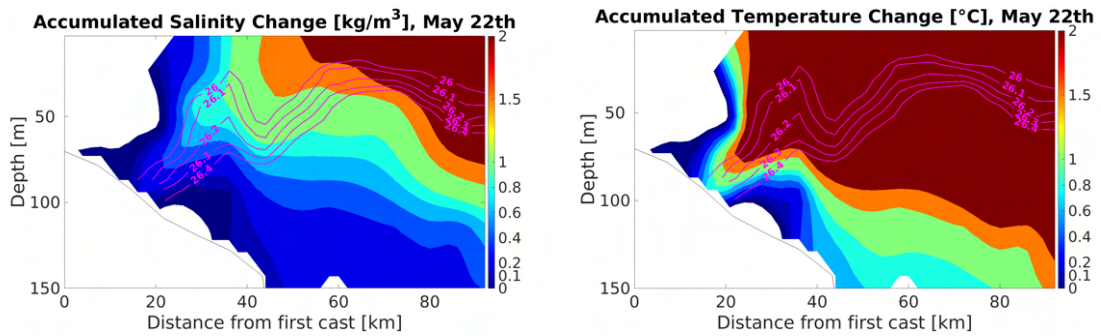


**Figure A.11:** From left to right: accumulated salinity (color) and temperature (color) change at the 22th May. The magenta contours represent isopycnals [ $\text{kg}/\text{m}^3$ ].

## A Accumulated properties change figures

July 2019

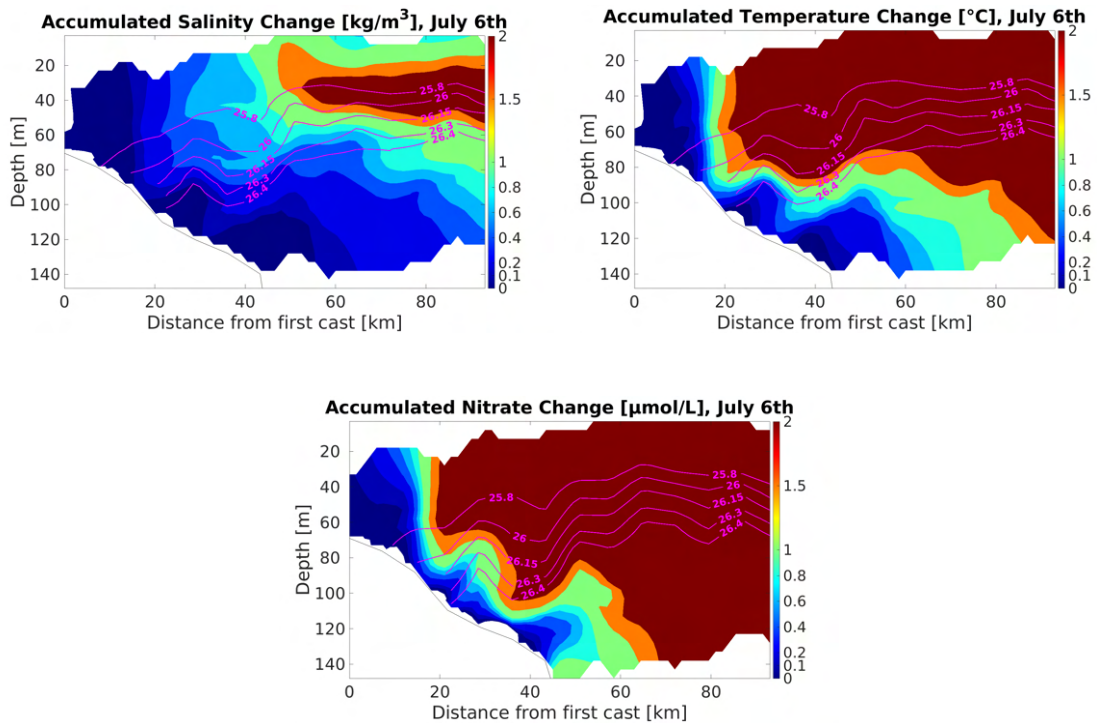


**Figure A.12:** From left to right: accumulated salinity (color), temperature (color), and nitrate (color) change at the 6th July. The magenta contours represent isopycnals [kg/m<sup>3</sup>].

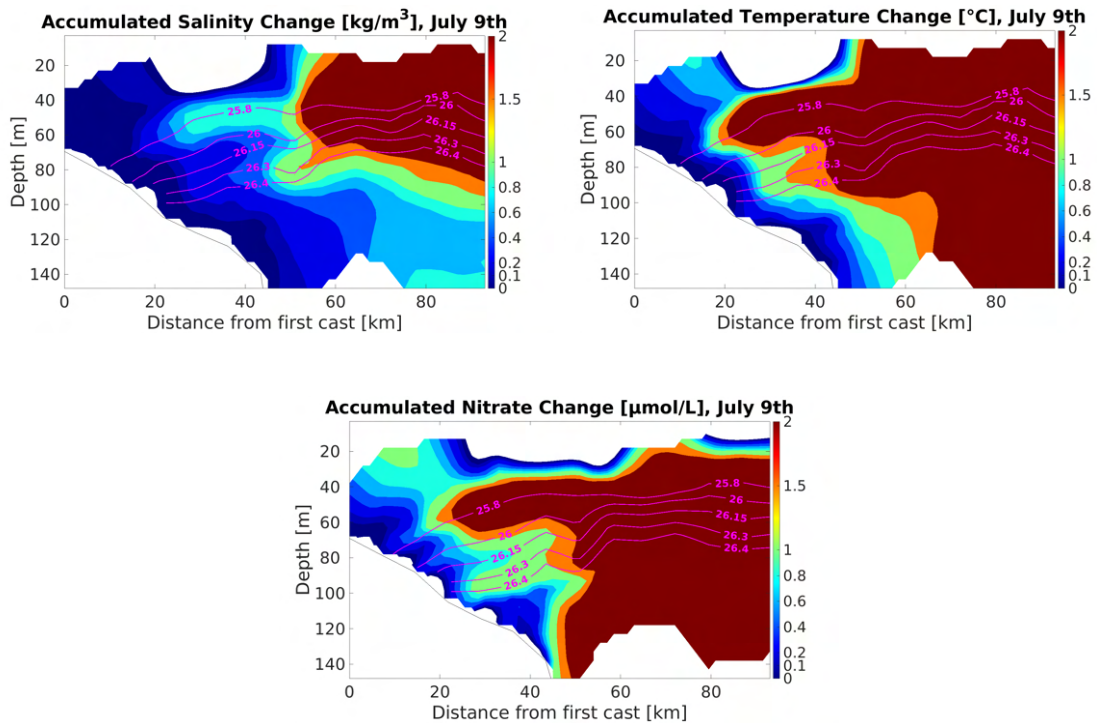


**Figure A.13:** From left to right: accumulated salinity (color), temperature (color), and nitrate (color) change at the 9th July. The magenta contours represent isopycnals [kg/m<sup>3</sup>].

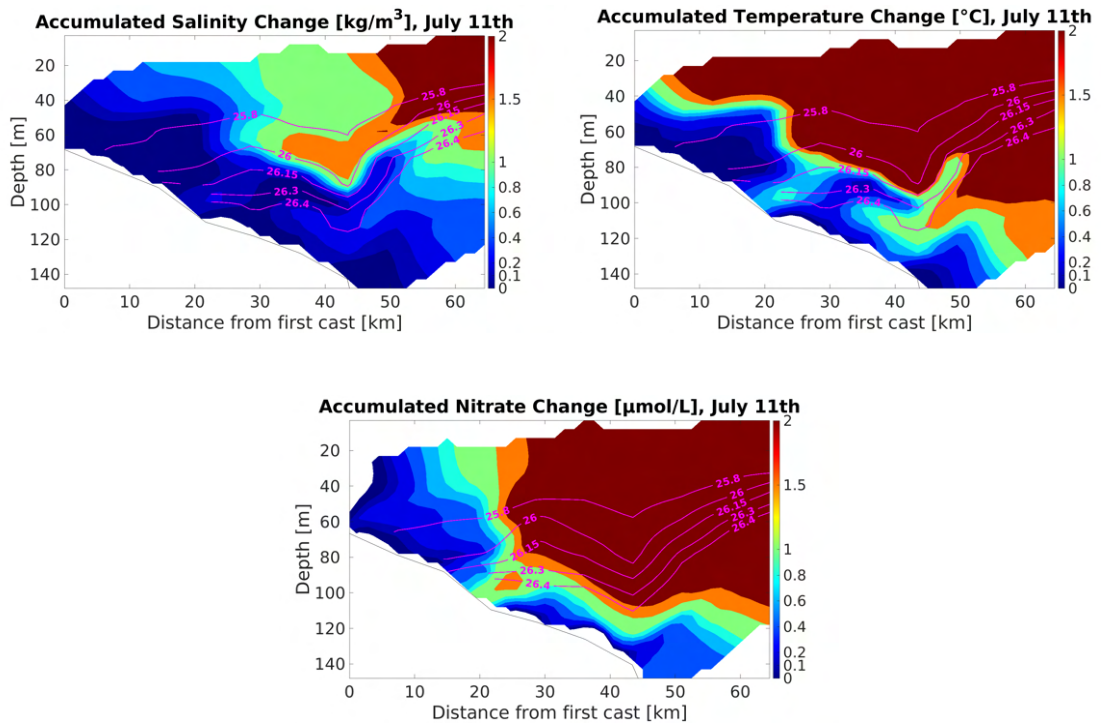


**Figure A.14:** From left to right: accumulated salinity (color), temperature (color), and nitrate (color) change at the 11th July. The magenta contours represent isopycnals [ $\text{kg}/\text{m}^3$ ].

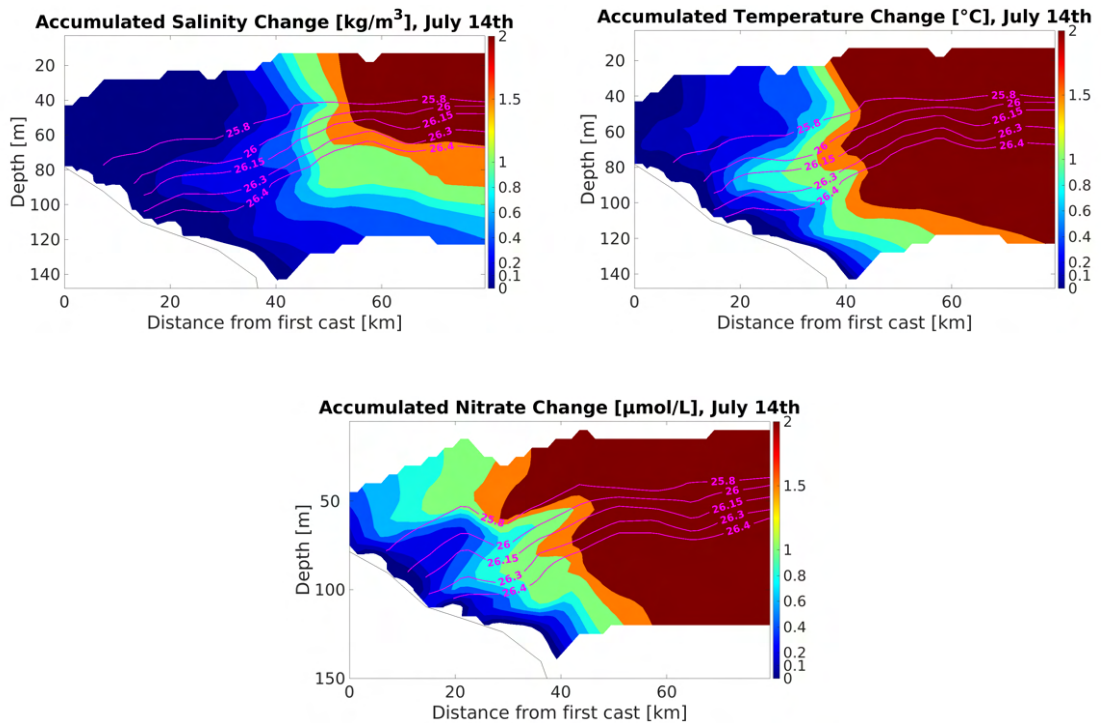


**Figure A.15:** From left to right: accumulated salinity (color), temperature (color), and nitrate (color) change at the 14th July. The magenta contours represent isopycnals [ $\text{kg}/\text{m}^3$ ].

## A Accumulated properties change figures

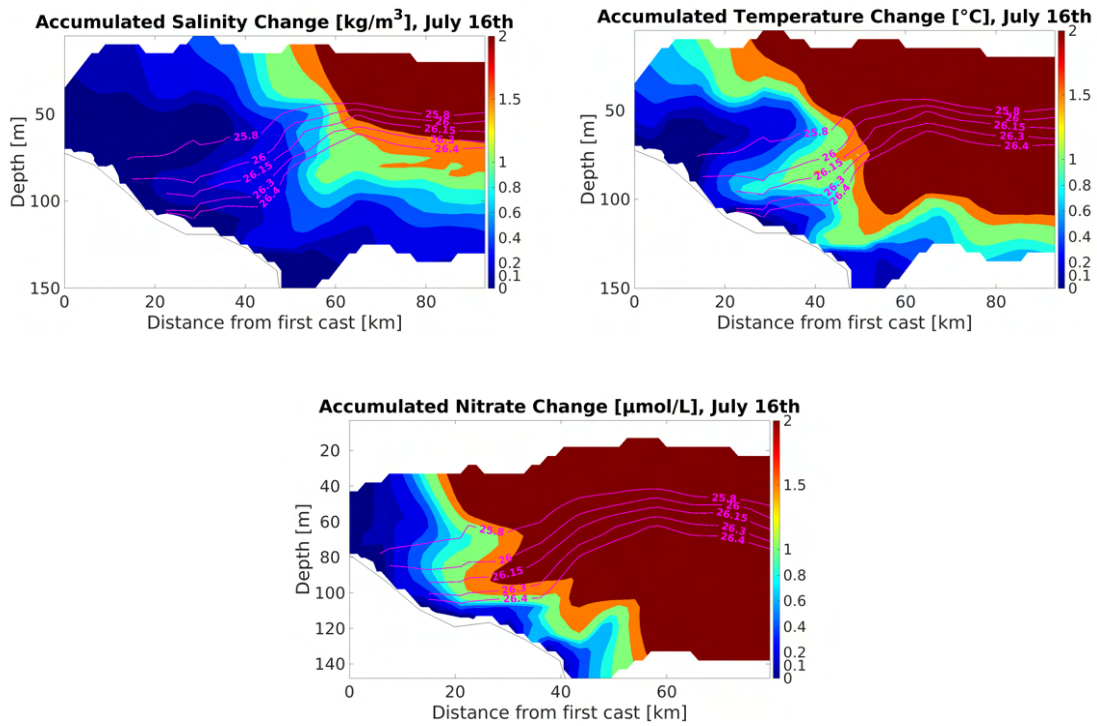


**Figure A.16:** From left to right: accumulated salinity (color), temperature (color), and nitrate (color) change at the 16th July. The magenta contours represent isopycnals [kg/m<sup>3</sup>].

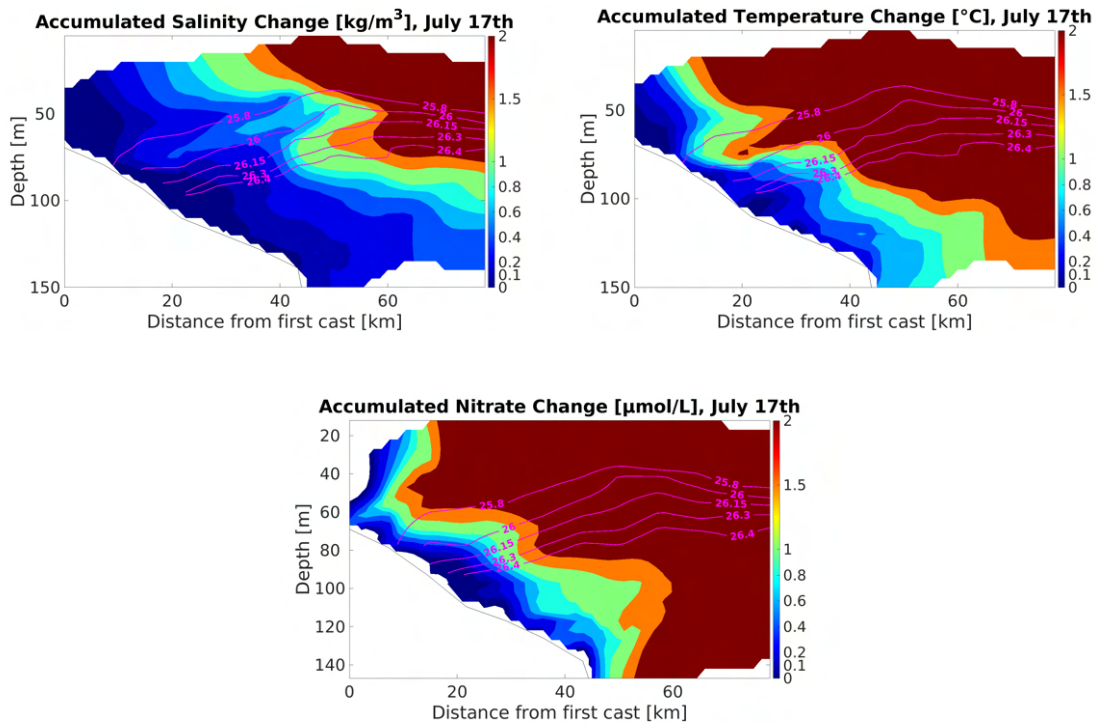


**Figure A.17:** From left to right: accumulated salinity (color), temperature (color), and nitrate (color) change at the 17th July. The magenta contours represent isopycnals [kg/m<sup>3</sup>].

---

## Acknowledgments

This thesis has been an incredible journey for me; I hope the first of many. For this reason, I want to thank all the people that have guided me throughout that.

I want to thank Prof. Nadia Pinardi for being one of my mentors; her passion and dedication to oceanography are a constant source of inspiration. I would like to extend my gratitude to Prof. Paolo Oddo for dedicating his time to teaching me, patiently listening to my doubts, and guiding me through challenges.

This work would not be possible without the invaluable collaboration with the *Woods Hole Oceanographic Institution* (WHOI), where I studied during this summer. Thus, I want to express my gratefulness to my advisors from there Dr. Dennis McGillicuddy and Dr. Glen Gawarkiewicz. Thank you for all the guidance and support throughout my work. I am thankful for the time and effort you have invested, patiently guiding me through this fascinating subject, and sharing your broad knowledge of oceanography. Moreover, I want to thank all the people that I have met from the Physical Oceanography department and from the SPIROPA project for providing constructive feedback that has significantly contributed to my scientific and personal growth.

This summer I had the opportunity to participate in an oceanographic cruise carried out in the NES-LTER project, hence I want to thank Heidi Sosik for giving me this terrific opportunity that I will never forget. A special thanks go also to Emily Peacock and Taylor Crockford for their patience and clear teaching of biological sampling.

Infine, ringrazio di cuore i miei genitori Nadia e Fabio per supportarmi in modo costruttivo nelle mie scelte e per l'attenzione che impiegate nel farlo. Un grazie particolare va anche alla mia nonna Vanna, che è la mia fan numero uno.



# Bibliography

- J. A. Barth, D. Bogucki, S. D. Pierce, and P. M. Kosro. Secondary circulation associated with a shelfbreak front. *Geophysical Research Letters*, 25(15):2761–2764, 1998. doi: <https://doi.org/10.1029/98GL02104>. URL <https://agupubs.onlinelibrary.wiley.com/doi/abs/10.1029/98GL02104>.
- W. Brown, O. Schofield, S. Glenn, J. Kohut, and W. Boicourt. Mid-atlantic bight cold pool based on ocean glider observations. *Continental Shelf Research*, 264: 105040, 2023. doi: <https://doi.org/10.1016/j.csr.2023.105040>. URL <https://www.sciencedirect.com/science/article/pii/S0278434323001176>.
- D. C. Chapman and S. J. Lentz. Trapping of a coastal density front by the bottom boundary layer. *Journal of Physical Oceanography*, 24:1464–1479, 1994. URL <https://api.semanticscholar.org/CorpusID:129703997>.
- E. C. M. S. CMEMS. Global Ocean Ensemble Physics reanalysis, 2023. data retrieved from Copernicus Marine Service, [https://data.marine.copernicus.eu/product/GLOBAL\\_REANALYSIS\\_PHY\\_001\\_031/description](https://data.marine.copernicus.eu/product/GLOBAL_REANALYSIS_PHY_001_031/description), accessed on 04/28/2023.
- J. J. Cullen. Subsurface chlorophyll maximum layers: Enduring enigma or mystery solved? *Annual Review of Marine Science*, 7(1):207–239, 2015. doi: 10.1146/annurev-marine-010213-135111. URL <https://doi.org/10.1146/annurev-marine-010213-135111>. PMID: 25251268.
- D. . N. C. f. A. R. S. E. Dee. The climate data guide: Era-interim, 11 2022. URL <https://climatedataguide.ucar.edu/climate-data/era-interim>. Retrieved on 2023-11-19.
- C. S. ECMWF, Copernicus Climate. ERA5 hourly data on single levels from 1940 to present, 2023. data retrieved from Climate Data Store, <https://cds.climate.copernicus.eu/cdsapp#!/dataset/reanalysis-era5-single-levels?tab=overview>, accessed on 04/11/2023.

- J. Forsyth, M. Andres, and G. Gawarkiewicz. Shelfbreak jet structure and variability off new jersey using ship of opportunity data from the cmv oleander. *Journal of Geophysical Research: Oceans*, 125(9):e2020JC016455, 2020. doi: <https://doi.org/10.1029/2020JC016455>. URL <https://agupubs.onlinelibrary.wiley.com/doi/abs/10.1029/2020JC016455>.
- G. Gawarkiewicz and D. C. Chapman. The role of stratification in the formation and maintenance of shelf-break fronts. *Journal of Physical Oceanography*, 22(7): 753 – 772, 1992. doi: [https://doi.org/10.1175/1520-0485\(1992\)022<0753:TROSIT>2.0.CO;2](https://doi.org/10.1175/1520-0485(1992)022<0753:TROSIT>2.0.CO;2). URL [https://journals.ametsoc.org/view/journals/phoc/22/7/1520-0485\\_1992\\_022\\_0753\\_trosit\\_2\\_0\\_co\\_2.xml](https://journals.ametsoc.org/view/journals/phoc/22/7/1520-0485_1992_022_0753_trosit_2_0_co_2.xml).
- G. Gawarkiewicz, K. H. Brink, F. Bahr, R. C. Beardsley, M. Caruso, J. F. Lynch, and C.-S. Chiu. A large-amplitude meander of the shelfbreak front during summer south of New England: Observations from the Shelfbreak PRIMER experiment. *Journal of Geophysical Research (Oceans)*, 109(C3):C03006, Mar. 2004. doi: 10.1029/2002JC001468.
- G. Gawarkiewicz, R. Pickart, W. G. Zhang, J. Partida, A. Mahmud-Ul-Hasan, P. Fratantoni, and A. M. Merce. The changing nature of shelf-break exchange revealed the ooi pioneer array. *Oceanography*, March 2018. URL <https://doi.org/10.5670/oceanog.2018.110>.
- C. G. GEBCO. Gebco 2022 grid, 2022. data retrieved from GEBCO Bathymetry Data, [https://www.gebco.net/data\\_and\\_products/gridded\\_bathymetry\\_data/](https://www.gebco.net/data_and_products/gridded_bathymetry_data/), accessed on 03/17/2023.
- M. Gurvan, R. Bourdallé-Badie, P.-A. Bouttier, C. Bricaud, D. Bruciaferri, D. Calvert, J. Chanut, E. Clementi, A. Coward, D. Delrosso, C. Ethé, S. Flavoni, T. Graham, J. Harle, D. Iovino, D. Lea, C. Lévy, T. Lovato, N. Martin, S. Masson, S. Mocavero, J. Paul, C. Rousset, D. Storkey, A. Storto, and M. Vancoppenolle. Nemo ocean engine, June 2019. URL <https://doi.org/10.5281/zenodo.3248739>.
- R. He, K. Chen, K. Fennel, G. Gawarkiewicz, and D. McGillicuddy. Seasonal and interannual variability of physical and biological dynamics at the shelfbreak front of the middle atlantic bight: Nutrient supply mechanisms. *Biogeosciences Discussions*, 8, 10 2011. doi: 10.5194/bg-8-2935-2011.
- A. J. Hirzel, P. Alatalo, H. Oliver, C. M. Petitpas, J. T. Turner, W. G. Zhang, and D. J. McGillicuddy. High resolution analysis of plankton distributions at

- the middle atlantic bight shelf-break front. *Continental Shelf Research*, 267: 105113, 2023. doi: <https://doi.org/10.1016/j.csr.2023.105113>. URL <https://www.sciencedirect.com/science/article/pii/S0278434323001905>.
- R. Houghton, F. Aikman, and H. Ou. Shelf-slope frontal structure and cross-shelf exchange at the new england shelf-break. *Continental Shelf Research*, 8(5):687–710, 1988. doi: [https://doi.org/10.1016/0278-4343\(88\)90072-6](https://doi.org/10.1016/0278-4343(88)90072-6). URL <https://www.sciencedirect.com/science/article/pii/0278434388900726>.
- R. W. Houghton and M. Visbeck. Upwelling and convergence in the middle atlantic bight shelfbreak front. *Geophysical Research Letters*, 25(15):2765–2768, 1998. doi: <https://doi.org/10.1029/98GL02105>. URL <https://agupubs.onlinelibrary.wiley.com/doi/abs/10.1029/98GL02105>.
- J. L. K.H. Mann. *Dynamics of Marine Ecosystem*. Blackwell Publishing, 2006.
- T. A.-M. Levy Marina, Klein Patrice. Impact of sub-mesoscale physics on production and subduction of phytoplankton in an oligotrophic regime, 2001. URL <https://archimer.ifremer.fr/doc/00000/800/>.
- Y. Li, R. P. Stumpf, D. McGillicuddy, and R. He. Dynamics of an intense alexandrium catenella red tide in the gulf of maine: satellite observations and numerical modeling. *Harmful Algae*, 99:101927, 2020. doi: <https://doi.org/10.1016/j.hal.2020.101927>. URL <https://www.sciencedirect.com/science/article/pii/S1568988320302067>.
- C. Linder. Software - bottom boundary layer analysis, 10 2005. URL [https://www.whoi.edu/science/P0/people/clinder/software\\_bbl.html](https://www.whoi.edu/science/P0/people/clinder/software_bbl.html). Accessed on 06/29/2023.
- C. A. Linder and G. Gawarkiewicz. A climatology of the shelfbreak front in the middle atlantic bight. *Journal of Geophysical Research: Oceans*, 103(C9):18405–18423, 1998. doi: <https://doi.org/10.1029/98JC01438>. URL <https://agupubs.onlinelibrary.wiley.com/doi/abs/10.1029/98JC01438>.
- C. A. Linder, GlenGawarkiewicz, and R. S. Pickart. Seasonal characteristics of bottom boundary layer detachment at the shelfbreak front in the middle atlantic bight. *Journal of Geophysical Research*, 109, 2004.
- J. Marra, R. Houghton, and C. Garside. Phytoplankton growth at the shelf-break front in the middle atlantic bight. *Journal of Marine Research*, 48:851–868, 11 1990. doi: 10.1357/002224090784988665.

- D. J. McGillicuddy Jr., W. G. Zhang, H. M. Sosik, W. Smith, R. Stanley, J. Turner, and C. Petitpas. *Collaborative Research Proposal: Shelfbreak frontal dynamics: mechanisms of upwelling, net community production, and ecological implications*. 2016.
- O. B. P. G. NASA Goddard Space Flight Center, Ocean Ecology Laboratory. Moderate-resolution imaging spectroradiometer (MODIS) Aqua Chlorophyll Data, 2022. data retrieved from NASA Ocean Color, <https://oceancolor.gsfc.nasa.gov/13/>, accessed on 03/17/2023.
- H. Oliver, W. G. Zhang, W. O. Smith Jr., P. Alatalo, P. D. Chappell, A. J. Hirzel, C. R. Selden, H. M. Sosik, R. H. R. Stanley, Y. Zhu, and D. J. McGillicuddy Jr. Diatom hotspots driven by western boundary current instability. *Geophysical Research Letters*, 48(11):e2020GL091943, 2021. doi: <https://doi.org/10.1029/2020GL091943>. URL <https://agupubs.onlinelibrary.wiley.com/doi/abs/10.1029/2020GL091943>.
- H. Oliver, W. G. Zhang, K. M. Archibald, A. J. Hirzel, W. O. Smith Jr, H. M. Sosik, R. H. R. Stanley, and D. J. McGillicuddy Jr. Ephemeral surface chlorophyll enhancement at the new england shelf break driven by ekman restratification. *Journal of Geophysical Research: Oceans*, 127(1):e2021JC017715, 2022. doi: <https://doi.org/10.1029/2021JC017715>. URL <https://agupubs.onlinelibrary.wiley.com/doi/abs/10.1029/2021JC017715>. e2021JC017715 2021JC017715.
- J. B. Palter and M. S. Lozier. On the source of gulf stream nutrients. *Journal of Geophysical Research: Oceans*, 113(C6), 2008. doi: <https://doi.org/10.1029/2007JC004611>. URL <https://agupubs.onlinelibrary.wiley.com/doi/abs/10.1029/2007JC004611>.
- R. Pickart. Bottom boundary layer structure and detachment in the shelfbreak jet of the middle atlantic bight. *Journal of Physical Oceanography*, 30(11):2668 – 2686, 2000. doi: [https://doi.org/10.1175/1520-0485\(2001\)031<2668:BBLSAD>2.0.CO;2](https://doi.org/10.1175/1520-0485(2001)031<2668:BBLSAD>2.0.CO;2). URL [https://journals.ametsoc.org/view/journals/phoc/30/11/1520-0485\\_2001\\_031\\_2668\\_bblsad\\_2.0.co\\_2.xml](https://journals.ametsoc.org/view/journals/phoc/30/11/1520-0485_2001_031_2668_bblsad_2.0.co_2.xml).
- A. Redfield. *On the Proportions of Organic Derivatives in Sea Water and Their Relation to the Composition of Plankton*. University Press of Liverpool, 1934. URL <https://books.google.it/books?id=szAezQEACAAJ>.
- J. L. Sarmiento. *Ocean Biogeochemical Dynamics*. Princeton University Press, 2006.
- I. Valiela. *Marine Ecological Processes*. Springer, 2015.

- P. Virtanen, R. Gommers, T. E. Oliphant, M. Haberland, T. Reddy, D. Cournapeau, E. Burovski, P. Peterson, W. Weckesser, J. Bright, S. J. van der Walt, M. Brett, J. Wilson, K. J. Millman, N. Mayorov, A. R. J. Nelson, E. Jones, R. Kern, E. Larson, C. J. Carey, Í. Polat, Y. Feng, E. W. Moore, J. VanderPlas, D. Laxalde, J. Perktold, R. Cimrman, I. Henriksen, E. A. Quintero, C. R. Harris, A. M. Archibald, A. H. Ribeiro, F. Pedregosa, P. van Mulbregt, and SciPy 1.0 Contributors. SciPy 1.0: Fundamental Algorithms for Scientific Computing in Python. *Nature Methods*, 17:261–272, 2020. doi: 10.1038/s41592-019-0686-2.
- P. Welch. The use of fast fourier transform for the estimation of power spectra: A method based on time averaging over short, modified periodograms. *IEEE Transactions on Audio and Electroacoustics*, 15(2):70–73, 1967. doi: 10.1109/TAU.1967.1161901.
- W. R. Wright and C. E. Parker. A volumetric temperature/salinity census for the middle atlantic bight1. *Limnology and Oceanography*, 21(4):563–571, 1976. doi: <https://doi.org/10.4319/lo.1976.21.4.0563>. URL <https://aslopubs.onlinelibrary.wiley.com/doi/abs/10.4319/lo.1976.21.4.0563>.
- W. Zhang, G. Gawarkiewicz, D. McGillicuddy, and J. Wilkin. Climatological mean circulation at the new england shelf break. *Journal of Physical Oceanography*, 41: 1874, 10 2011. doi: 10.1175/2011JPO4604.1.
- W. G. Zhang and G. G. Gawarkiewicz. Length scale of the finite-amplitude meanders of shelfbreak fronts. *Journal of Physical Oceanography*, 45(10):2598 – 2620, 2015. doi: <https://doi.org/10.1175/JPO-D-14-0249.1>. URL <https://journals.ametsoc.org/view/journals/phoc/45/10/jpo-d-14-0249.1.xml>.
- W. G. Zhang, D. J. McGillicuddy Jr., and G. Gawarkiewicz. Is biological productivity enhanced at the new england shelfbreak front? *Journal of Geophysical Research: Oceans*, 118(1):517–535, 2013. doi: <https://doi.org/10.1002/jgrc.20068>. URL <https://agupubs.onlinelibrary.wiley.com/doi/abs/10.1002/jgrc.20068>.
- W. G. Zhang, P. Alatalo, T. Crockford, A. J. Hirzel, M. G. Meyer, H. Oliver, E. Peacock, C. M. Petitpas, Z. Sandwith, W. O. Smith, H. M. Sosik, R. H. Stanley, B. L. Stevens, J. T. Turner, and D. J. McGillicuddy. Cross-shelf exchange associated with a shelf-water streamer at the mid-atlantic bight shelf edge. *Progress in Oceanography*, 210:102931, 2023. doi: <https://doi.org/10.1016/j.pocean.2022.102931>. URL <https://www.sciencedirect.com/science/article/pii/S0079661122001902>.